POLITECNICO
MILANO 1863

SCUOLA DI INGEGNERIA INDUSTRIALE
E DELL'INFORMAZIONE

Study of Heliocentric Escape Dynamics from Earth-Moon L2 Near Rectilinear Halo Orbits

Tesi di Laurea Magistrale in
Space Engineering - Ingegneria Spaziale

Author: **Francesca Giulia Cicchi**

Student ID: 247718
Advisor: Prof. Camilla Colombo
Co-advisors: Mathilda Bolis
Academic Year: 2024-25

This content is original, written by the Author, Francesca Giulia Cicchi. All the non-original information, taken from previous works, are specified and recorded in the Bibliography.

When referring to this work, full bibliographic details must be given, i.e.
Francesca Giulia Cicchi, "Study of heliocentric escape dynamics from Earth-Moon L2 Near Rectilinear Halo Orbits". 2026, Politecnico di Milano, Faculty of Industrial Engineering, Department of Aerospace Science and Technologies, Master in Space Engineering, Supervisor: Camilla Colombo, Co-supervisor: Mathilda Bolis.

Declaration of generative AI and AI-assisted technologies in the manuscript preparation process.

During the preparation of this thesis the author used ChatGPT (OpenAI) only to support language correction and text clarity in selected parts of the manuscript. After using this tool, the author reviewed and edited the content as needed and takes full responsibility for the content of the manuscript.

Printed in Italy

Abstract

The increasing use of Near-Rectilinear Halo Orbits (NRHOs) in the Earth-Moon system requires the definition of reliable End-of-Life (EoL) strategies to prevent long-term accumulation of inactive spacecraft in the cislunar environment. Among the proposed solutions, heliocentric disposal represents a promising option, as it enables the spacecraft to permanently leave the Earth-Moon region. However, despite the recognised influence of the relative Sun-Earth-Moon configuration on escape trajectories, the mechanisms governing heliocentric disposal from NRHOs remain only partially understood.

This thesis investigates heliocentric escape from Earth-Moon L2 NRHOs within the coupled Circular Restricted Three-Body Problem (CR3BP) framework. The analysis exploits invariant manifold dynamics to generate disposal trajectories and includes a systematic parametric study in which the orbital phase angle and the relative Sun-Earth-Moon configuration are varied. The results are synthesised in escape maps constructed for four representative NRHOs, characterised by different dynamic properties. These maps reveal the coexistence of regular escape regions and highly fragmented areas associated with increased dynamical sensitivity. Overall, the escape behaviour is shown to depend on both the orbital phase and the relative Sun-Earth-Moon configuration, confirming the central role of geometry in shaping the heliocentric disposal dynamics.

To support the interpretation of the observed structures, additional dynamical indicators including the Jacobi Constant (JC) and the Finite-Time Lyapunov Exponent (FTLE), are considered to further characterise the escape dynamics.

Overall, this work provides a structured dynamical framework for understanding heliocentric disposal from NRHOs and supports the development of more systematic EoL strategies in the cislunar environment.

Keywords: Near-Rectilinear Halo Orbits, heliocentric disposal, coupled CR3BP, invariant manifolds, cislunar environment, escape dynamics

Abstract in lingua italiana

L'impiego crescente delle Orbite Halo Quasi Rettilinee (NRHOs) nel sistema Terra-Luna richiede la definizione di strategie di Fine Vita (EoL) affidabili, al fine di prevenire l'accumulo a lungo termine di veicoli spaziali inattivi nell'ambiente cislunare. Tra le soluzioni proposte, il disposal eliocentrico rappresenta un'opzione promettente, poiché consente al veicolo di abbandonare permanentemente la regione Terra-Luna. Tuttavia, nonostante sia riconosciuta l'influenza della configurazione relativa Sole-Terra-Luna sulle traiettorie di fuga, i meccanismi che governano il disposal eliocentrico da NRHOs risultano ancora solo parzialmente compresi.

La presente tesi analizza la fuga eliocentrica dalle NRHOs attorno a L_2 del sistema Terra-Luna nell'ambito del Problema Circolare Ristretto dei Tre Corpi (CR3BP) accoppiato. L'analisi sfrutta la dinamica delle varietà instabili delle NRHO per generare traiettorie di smaltimento e include uno studio parametrico sistematico in cui vengono variati l'angolo di fase orbitale e la configurazione relativa Sole-Terra-Luna. I risultati sono sintetizzati in mappe di fuga costruite per quattro NRHOs rappresentative, caratterizzate da differenti proprietà dinamiche. Tali mappe rivelano la coesistenza di regioni di fuga regolari e di aree fortemente frammentate associate a una maggiore sensibilità dinamica. Nel complesso, il comportamento di fuga risulta dipendere sia dalla fase orbitale sia dalla configurazione relativa Sole-Terra-Luna, confermando il ruolo centrale della geometria nel determinare la dinamica del disposal eliocentrico. A supporto dell'interpretazione delle strutture osservate, vengono inoltre considerati ulteriori indicatori dinamici, tra cui la Costante di Jacobi (JC) e l'Esponente di Lyapunov a Tempo Finito (FTLE), al fine di caratterizzare ulteriormente la dinamica di fuga.

Nel complesso, questo lavoro fornisce un quadro strutturato per la comprensione del disposal eliocentrico da NRHOs e supporta lo sviluppo di strategie di EoL più sistematiche nell'ambiente cislunare.

Parole chiave: Orbite Halo quasi rettilinee, smaltimento eliocentrico, CR3BP accoppiato, varietà instabili, ambiente cislunare, dinamica di fuga

Contents

1 | Introduction

This first Chapter presents the context in which the Thesis is developed, together with the research gaps that have motivated this work and the objectives. Finally, a brief outline of the overall structure is provided.

1.1. Description of the problem

The renewed interest in lunar exploration has progressively shifted the focus of astrodynamics from Earth-centered mission design to the broader and more complex cislunar environment. The region governed by the combined gravitational influence of the Earth and the Moon is no longer considered a transitional domain between different gravitational environments, but rather a strategic operational space for future long-term activities.

The cislunar environment is commonly described using the three-body problem, in which equilibrium solutions arise from the combined gravitational interaction of two primary bodies. The existence of such equilibrium points has been known since the eighteenth century, following the work of Euler [1] and Lagrange [2]. However, their practical relevance for space missions emerged only in the second half of the twentieth century, when advances in spaceflight made it possible to consider trajectories beyond the classical two-body framework. Early studies identified the potential of libration point regions for communication and observation purposes, and soon after, three-dimensional periodic solutions around the collinear points, later termed halo orbits, were systematically investigated. These studies gradually led to the operational use of Libration Point Orbits (LPOs), first in the Sun-Earth system and later in other gravitational configurations [3].

With the increasing attention devoted to space sustainability, the mitigation principles already adopted for the congested near Earth environment [4] are progressively being considered also for operations in the cislunar region. As this cislunar region becomes progressively more populated, dedicated End-of-Life (EoL) strategies are required to prevent long-term accumulation of inactive spacecraft and to preserve operational safety for future missions. To address these concerns, recent literature has begun to propose guidelines for

EoL disposal in cislunar space, aiming to ensure its long-term sustainability [5, 6]. However, the dynamical environment near libration points is complex, characterised by strong nonlinear behaviour. In such a highly sensitive and chaotic framework, the long-term evolution of spacecraft trajectories may be difficult to predict, significantly complicating the design and assessment of reliable disposal solutions. In particular, the European Space Agency (ESA) has emphasised the importance of protecting lunar orbital regions as exploration activities intensify [5]. Ensuring their sustainable use requires dedicated EoL strategies based on long-term dynamical analysis.

Among the family of halo orbits around Earth-Moon L_2, Near-Rectilinear Halo Orbits (NRHOs) have recently gained particular relevance. NRHOs are highly elongated three-dimensional periodic trajectories characterised by close lunar approaches and pronounced out-of-plane motion. Compared to other halo solutions, they combine favorable communication geometry with relatively moderate station-keeping requirements, making them suitable for long-duration missions. For these reasons, NRHOs have been selected as the reference orbit for the Lunar Gateway[1], the first planned permanent space station beyond Low Earth Orbit (LEO), within the Artemis program[2]. As a consequence, NRHOs are expected to host a growing number of spacecraft in the coming years, making the design of reliable disposal strategies in this dynamical regime a matter of strategic importance.

1.2. Motivation

The increasing operational relevance of NRHOs in future cislunar missions makes the development of robust disposal strategies a critical aspect of mission sustainability. Among the available EoL options, heliocentric disposal is particularly attractive, as it allows the spacecraft to permanently leave the Earth-Moon environment.

Previous investigations have analysed disposal trajectories from Earth-Moon LPOs, highlighting the decisive role of the Sun in enabling or preventing successful escape. These studies show that the outcome of heliocentric disposal is strongly influenced by the relative Sun-Earth-Moon configuration. However, the geometric dependence of escape has not been systematically characterised within a structured parametric framework, nor has it been explicitly interpreted in terms of the dynamical mechanisms governing transport between the cislunar and heliocentric domains.

[1]National Aeronautics and Space Administration (NASA), *Gateway*, `https://www.nasa.gov/mission/gateway/`, last accessed 22 September 2025.

[2]National Aeronautics and Space Administration (NASA), *Artemis Mission*, `https://www.nasa.gov/humans-in-space/artemis/`, last accessed 22 September 2025.

The research questions addressed in this Thesis are therefore:

- How does the relative Sun-Earth-Moon configuration influence the success of heliocentric escape from Earth-Moon L_2 NRHOs?
- Can the observed escape behaviour be interpreted and characterised in terms of the underlying dynamical structures governing transport in the Sun-Earth-Moon system?

1.3. Objectives

In order to address the research questions formulated above, this Thesis develops a structured dynamical framework to investigate heliocentric escape from Earth-Moon L_2 NRHOs. The analysis is conducted within a coupled Circular Restricted Three-Body Problem (CR3BP) formulation, allowing a consistent description of the transition between the Earth-Moon and Sun-Earth dynamical environments.

Heliocentric disposal trajectories are generated by exploiting invariant manifold dynamics associated with representative NRHOs. A systematic parametric study is then performed, varying both the orbital phase along the NRHO and the relative Sun-Earth-Moon configuration, in order to evaluate their influence on escape outcomes. The results are synthesised through the construction of escape maps, enabling the identification of successful disposal regions and dynamically sensitive regimes.

Finally, the observed escape behaviour is interpreted from a dynamical perspective, relating the escape geometry to energetic conditions and local sensitivity within the coupled system.

1.4. Thesis outline

The Thesis is structured into six Chapters, organised as follows:

- **Chapter 1** introduces the context of cislunar exploration and motivates the need for reliable EoL strategies for spacecraft operating in NRHOs. The research questions and objectives of the Thesis are defined.
- **Chapter 2** reviews the current state of the art on NRHOs relevance, cislunar debris mitigation and disposal strategies, with particular emphasis on heliocentric escape solutions from LPOs and on the dynamical mechanisms exploited in previous studies.

- **Chapter 3** presents the dynamical framework adopted in this work. The CR3BP is introduced, together with its main properties, and the coupled Earth-Moon and Sun-Earth formulation is described.
- **Chapter 4** details the methodology of the study. The computation of the NRHO family, the construction of invariant manifolds, and the implementation of the parametric escape analysis within the coupled CR3BP framework are presented.
- **Chapter 5** discusses the results of the parametric escape analysis. Escape maps are constructed for representative NRHOs and interpreted in terms of geometrical configuration, energetic constraints, and dynamical sensitivity.
- **Chapter 6** summarises the main findings of the Thesis and outlines possible extensions of the present work, both in terms of dynamical modelling and operational applications.

2 | Literature review

This Chapter reviews the state of the art on the topics most relevant to this Thesis. It first discusses debris mitigation in the cislunar environment and the main EoL strategies for spacecraft operating in the Earth-Moon system, with particular attention on sustainable disposal solutions. The focus then shifts to NRHOs, outlining their key dynamical and operational properties and their relevance for future cislunar missions. Finally, disposal design from Earth-Moon and Sun-Earth LPOs is introduced, together with a discussion on manifold-based transfer strategies, which form the basis of the disposal approach investigated in this work.

2.1. Debris mitigation

Debris mitigation strategies in Earth orbit are well established and have progressively evolved over the years. In LEO, disposal often relies on a combination of manoeuvres and the natural decay induced by atmospheric drag, while at higher-altitude graveyard orbits are commonly used. These approaches are reported in current mitigation guidelines [6]. Disposal strategies for cislunar missions build on these established approaches. However, the dynamical environment beyond Earth orbit differs significantly. In particular, the absence of atmospheric drag and the high non-linear dynamics prevent relying on passive orbital decay mechanisms. As a result, disposal strategies in cislunar space cannot be transferred directly from the terrestrial context and require a dedicated analysis of its dynamical structure.

The progressive expansion of missions operating in the Earth-Moon system requires the definition of reliable debris mitigation and EoL strategies to preserve the long-term sustainability of cislunar operations. Spacecraft operating in cislunar space evolve within a multi-body gravitational environment dominated by the Earth, Moon, and Sun. In this regime, motion is governed by non-linear dynamics and can exhibit strong sensitivity to initial conditions [7, 8]. As a result, uncontrolled spacecraft may remain for long periods in operational regions or migrate across protected zones if disposal is not properly designed [9].

In response to the evolving use of cislunar space, international agencies have recently introduced specific mitigation guidelines addressing disposal for missions operating beyond Earth orbit. The ESA Space Debris Mitigation Requirements [5] explicitly extend debris mitigation principles to cislunar space and define disposal strategies aimed at preventing the long-term accumulation of inactive spacecraft within the Earth-Moon system. Four main EoL strategies can be identified for spacecraft operating in the cislunar region:

- **Heliocentric disposal:** injection into a heliocentric orbit enables the permanent removal of the spacecraft from the Earth-Moon system. When successfully achieved, this option eliminates long-term collision risks within cislunar operational regions and prevents future interference with protected orbital zones. For this reason, heliocentric disposal is generally considered the most robust long-term mitigation strategy and is prioritised in current ESA requirements whenever mission constraints allow it [5].
- **Lunar impact:** a controlled impact on the lunar surface provides an effective and historically adopted removal mechanism. However, its extensive use raises concerns regarding the preservation of scientifically relevant sites, future operational areas and heritage locations on the lunar surface, making its large-scale adoption less desirable from a long-term sustainability perspective, as discussed for example in [10].
- **Earth atmospheric re-entry:** transfer to a trajectory leading to atmospheric re-entry ensures the complete disintegration of the spacecraft and therefore a definitive removal. Nevertheless, this option typically requires higher costs and must comply with strict safety and operational constraints [6].
- **Cislunar graveyard orbit:** relocation to dynamically stable or weakly interacting orbits around the Earth or the Moon represents an alternative when direct removal is not feasible. Although this approach reduces the probability of interference with operational trajectories, it does not guarantee permanent removal from the Earth-Moon environment and therefore represents a less robust long-term solution, as discussed in [10].

In particular, heliocentric disposal is identified as the preferred long-term solution whenever technically feasible. When heliocentric disposal cannot be achieved, the alternative strategies, may be adopted, when justified through dedicated orbit propagation and disposal analyses in accordance with [5].

2.2. Operational relevance of Near Rectilinear Halo Orbits

NRHOs have been extensively investigated in recent years within the framework of multi-body dynamics. Early studies have focused on their generation, orbital characteristics, and stability properties within the CR3BP, as well as on their suitability for long-duration missions in the Earth-Moon system. Subsequent works have analysed operational aspects, including station-keeping requirements, transfer strategies, and robustness under perturbations. More recently, attention has also been directed toward the EoL scenarios. The following overview summarises the main contributions in the literature concerning NRHOs characterisation.

NRHOs are commonly classified in terms of their linear stability properties, which can be described by a Stability Index (SI) derived from the monodromy matrix of the periodic orbit. This metric provides an indicator of the sensitivity to perturbations over one orbital period, and it is commonly used to compare different NRHO families and amplitudes. A detailed definition and interpretation of the adopted SI, together with its computation procedure within the CR3BP, are provided in Sec. 4.3 of this Thesis.

From an operational standpoint, one of the primary advantages of NRHOs lies in the relatively low cost required to maintain the orbit over extended mission durations. Although these orbits are formally unstable, their divergence from the nominal trajectory occurs over long time scales, enabling effective station-keeping with modest propellant. Detailed analyses of orbit maintenance in lunar NRHOs show that long-term operations can be sustained through different control strategies that exploit the underlying dynamical structure of the orbit, including approaches based on dynamical systems theory and reference-state targeting [11].

Particularly relevant are NRHOs that exhibit resonance with the lunar synodic period. Synodic resonant NRHOs are defined by an integer ratio between the spacecraft orbital period and the Earth-Moon synodic period. Resonant families are therefore classified through an integer ratio between the number of spacecraft revolutions N and the number of lunar synodic periods Q, typically denoted as a resonance N:Q [12]. When the orbital period is synchronised with the synodic motion, illumination conditions repeat predictably, allowing mission designers to select epochs that minimise or even eliminate Earth and lunar eclipses over extended intervals. Such eclipse-avoidance capabilities are particularly valuable for missions subject to strict thermal and power constraints, and they constitute a primary operational reason for adopting NRHOs as staging orbits in cislunar

space [13]. Among the possible resonant options, the 9:2 synodic resonance has received particular attention. Within the broader class of synodic resonances discussed above, this configuration represents a well-balanced compromise between illumination performance, dynamical stability, and transfer accessibility. For this reason, it has been adopted as the baseline orbit for the Lunar Gateway architecture due to its suitability for sustained crewed operations [12, 14].

A further quantity that has been used to characterise trajectory evolution in the NRHO region is the Momentum Integral (MI) [11]. This parameter can be used to map deviations from confined orbital motion. For periodic trajectories the MI remains limited, whereas significant variations may indicate that the spacecraft is leaving the NRHO vicinity. The behaviour of the MI is used as a practical indicator for both station-keeping and escape detection. In station-keeping applications, a sustained increase of the MI is interpreted as a warning that the spacecraft is drifting away from the nominal orbit. Conversely, in disposal and EoL analyses, the same behaviour can be used to determine when the spacecraft has permanently left the operational NRHO region and entered a disposal trajectory.

2.3. Strategies for disposal design

As anticipated in the introduction of this Chapter, this Section also addresses transfers exploiting invariant manifold dynamics, which are relevant to the disposal approach considered in this work.

2.3.1. Libration Points Orbits transfer exploiting manifold dynamics

Within the CR3BP framework described in Sec. 3.7, periodic orbits are associated with stable and unstable invariant manifolds. These structures define natural pathways that can map the spacecraft motion within multi-body dynamical environments and are therefore widely exploited for trajectory design.

The systematic use of invariant manifolds for transfers between different gravitational regimes was formalised by Koon et al. [15], whose work represents a cornerstone in the use of invariant manifolds for trajectory design in multi-body systems. In that study, the Sun-Earth-Moon four-body problem is interpreted as two coupled three-body systems, and low-energy Earth-Moon transfers are obtained through the intersection of invariant manifold structures associated with the Sun-Earth and Earth-Moon CR3BP. A key outcome of

this approach is that the existence of low-energy connections between different dynamical regions depends on the relative Sun-Earth-Moon configuration, which determines whether invariant manifold trajectories associated with the two systems can effectively connect. Although the present work focuses on heliocentric escape rather than targeted capture, this perspective is directly relevant, as the relative geometry of the three primaries governs the accessibility of invariant manifold linking Earth-Moon libration regions to heliocentric trajectories.

Building on this coupled-systems viewpoint, numerous works, i.e. Lei et al. [16] proposed systematic transfer strategies between LPOs of the Sun-Earth and Earth-Moon systems. Their methodology combines invariant manifold propagation in the Sun-Earth CR3BP with a BCR4BP formulation to connect the transition toward the Earth-Moon environment. This work provides an additional example of transfer design across multiple gravitational regimes, combining different dynamical models to describe the transition between the Sun-Earth and Earth-Moon environments.

More recent investigations have explored how manifold-based trajectory design can be combined with additional optimization and control strategies. Zhang et al. [17], for example, examined transfers from unstable Earth-Moon libration point orbits to the lunar surface by coupling invariant manifold arcs with two-body transfer segments and numerical optimization. Their results illustrate how manifold-guided trajectories can be integrated within more flexible design frameworks when purely ballistic solutions are suboptimal.

Complementary studies have instead focused on the robustness of manifold-based transfers within a single dynamical system. Srivastava et al. [18] investigated halo orbit transfers in the Sun-Earth CR3BP including additional perturbations such as solar radiation pressure and oblateness of the Earth, showing that invariant manifolds remain effective design structures even in more realistic dynamical models. While such analyses do not consider coupled multi-system dynamics, they confirm the persistence of manifold-driven transport mechanisms under perturbations.

Overall, these works demonstrate that invariant manifolds provide a coherent framework to describe natural transport across and within multi-body dynamical systems. In the context of heliocentric escape from Earth-Moon libration regions, this perspective is particularly relevant, as escape trajectories can be interpreted as the continuation of manifold-guided motion from the cislunar environment into the Sun-Earth dynamical domain, with the relative configuration of the primaries playing a central role in shaping the accessible pathways.

The literature on manifold-based transfers is extensive, and the studies cited here are provided only as representative examples, since a comprehensive review of this topic is beyond the scope of the present work.

2.3.2. Sun-Earth Libration Point Orbits disposal

Several studies have investigated disposal strategies for spacecraft operating in Sun-Earth LPOs, often considering past and current missions as representative case studies, such as Gaia, SOHO, and Herschel. For these missions, different EoL options have been analysed, including heliocentric graveyard orbits, lunar impact, and controlled Earth re-entry.

Among the most comprehensive contributions, Colombo et al. [19] examine three representative missions and assess all the main disposal strategies, heliocentric graveyard, lunar impact, and Earth re-entry, within a coherent and general framework. Their work is particularly relevant as it provides a systematic overview of the problem, combining dynamical modelling and optimisation techniques while extending the analysis also to highly elliptical orbit missions. Armellin et al. [20, 21] investigate disposal strategies for libration point missions, with particular attention to SOHO and Gaia. In [20], a high-fidelity $(n+1)$-body dynamical model is combined with a structured two-step optimisation approach and an energetic formulation for heliocentric disposal. The subsequent study [21] focuses specifically on Gaia, providing a more mission-oriented analysis of EoL options.

Other authors concentrate on a single disposal option. Concerning heliocentric disposal, Olikara [22] proposes a trajectory design based on Sun-Earth CR3BP invariant structures. Beyond the specific results, a major strength of this work lies in the clear and detailed description of the manifold dynamics, which is not always presented in a systematic way in the literature. Soldini et al. [23] also investigate heliocentric graveyard solutions exploiting the natural transport mechanisms of the three-body problem, and further introduces the use of solar sails to modify the topology of the Zero Velocity Curves (ZVCs), enabling additional dynamical pathways. In contrast, Colombo et al. [24] approach the same problem from an optimisation perspective.

Lunar impact disposal is addressed in detail by Van der Weg [25], whose work is particularly relevant for the present Thesis, as it exploits the same dynamical model used herein. In addition to exploiting natural transport structures to achieve the transfer, the authors model the trajectory from the Sun-Earth Lagrange points to the Moon within a coupled CR3BP framework.

Earth re-entry disposal is treated more specifically by Alessi [26, 27], who analyses feasible re-entry conditions and associated dynamical constraints.

A common feature of all these studies is the systematic exploitation of the natural transport properties of multi-body dynamics. This is consistent with the favourable results already discussed in the previous Section, where such structures proved to be an effective alternative to purely optimisation-based approaches. Their repeated adoption across different disposal strategies confirms their versatility and practical relevance. This motivates their further investigation in the present Thesis. However, when considering heliocentric disposal from cislunar orbits, the problem becomes more complex. The spacecraft must evolve under the combined influence of the Sun, the Earth and the Moon, making simplified three-body models insufficient. As a consequence, dynamical models that explicitly include the combined gravitational influence of the Earth, Moon, and Sun, such as a coupled CR3BP or a Bicircular Restricted Four-Body Problem (BCR4BP), are required to capture the essential dynamics of the transfer.

2.3.3. Earth-Moon Near Rectilinear Halo Orbits disposal

Recent studies have specifically addressed EoL strategies for spacecraft operating on NRHOs, with particular attention to heliocentric disposal, although lunar impact options have also been investigated. Since the present work focuses on heliocentric escape, only contributions relevant to this scenario are discussed here.

Most analyses are conducted within the BCR4BP, which explicitly accounts for the effects of the Sun, the Earth and the Moon on trajectory design. Unlike the CR3BP, the BCR4BP does not admit an integral of motion like the Jacobi Constant (JC) due to the explicit time-dependence introduced by the Sun effect. As a consequence the classical concept of fixed ZVC is not valid. An energy-like quantity, often referred to as the Hamiltonian of the system, is instead used to characterise the instantaneous energetic state. However, this quantity is not constant along the trajectory, and the associated forbidden regions evolve with the relative Sun-Earth-Moon configuration.

Among the first systematic investigations, Boudad et al. [28, 29] initiated a series of studies aimed at characterising heliocentric disposal trajectories departing from NRHOs. In these works, separation manoeuvres are applied along the instantaneous velocity direction of the spacecraft. A parametric analysis is performed by varying both the ΔV magnitude and the phase angle along the orbit θ, in order to explore the sensitivity of the resulting trajectories. A distinction is introduced between departure and escape. Departure corresponds to the effective exit from the NRHO and is identified through the evaluation of the MI, introduced in Sec. 2.2, when a prescribed threshold is exceeded. Escape, instead, is defined as the instant at which the spacecraft exits the Earth's vicinity, modelled as a

sphere centred at the Earth with radius equal to the Earth-Sun L_1 distance. The resulting trajectories are classified into three categories:

- Direct Escape: the trajectory directly connects with the departing flow, leading to a prompt transition toward heliocentric motion.
- Indirect Escape: the trajectory exhibits additional apoapses with respect to the Earth-Moon barycentre B_1, but eventually connects with the departing flow.
- Capture: the trajectory shows additional apoapses with respect to B_1, but does not connect with the departing flow within the considered time, or results in impact with the Earth or the Moon.

Concerning the influence of the manoeuvre location, [28, 29] show that burns performed at perilune in the velocity direction generally lead to faster departures, whereas manoeuvres at apolune tend to produce longer and more variable escape times. The higher orbital velocity at perilune amplifies the effect of the applied ΔV, favouring a more rapid divergence from the NRHO. At apolune, instead, the lower velocity reduces the energetic leverage of the manoeuvre, and the resulting trajectories display a stronger variability.

A similar conclusion is reached in the subsequent works by Davis et al. [30, 31], which further analyse both departure times and heliocentric escape conditions. These works also analyse manoeuvre directions other than the tangential one, including normal and binormal directions. The effectiveness of the manoeuvre direction depends on the spacecraft location along the NRHO. Tangential burns generally provide the fastest escape, with the best performance near perilune, while their effectiveness decreases as the burn location moves toward apolune.

Beyond this global trend, [31] provide an additional dynamical interpretation based on the local linear structure of the NRHOs. The angle between the stable and unstable eigenvectors of the periodic orbit is evaluated along the trajectory. Near perilune, the angle between these eigenvectors is small, meaning that the invariant manifolds are locally less distinct and the dynamics is highly sensitive to perturbations. Near apolune, instead, the eigenvectors are well separated, and the associated manifolds appear more clearly structured. Although the manifolds are locally less distinguishable near perilune, the unstable direction still corresponds to the eigenvector associated with the maximum growth of perturbations and therefore remains dynamically meaningful for escape purposes.For this reason, their role is further investigated in the present Thesis, whose objective is to provide a dynamical characterisation of the escape process and the associated transport mechanisms, with the aim of identifying favourable escape conditions.

Regarding the effect of the ΔV magnitude, the studies show that, when escape occurs, increasing ΔV generally reduces the time required to depart from the NRHO. However, a larger ΔV does not necessarily increase the probability of achieving escape.

More recent investigations [32, 33] extend earlier NRHO disposal analyses to Gateway jettison operations, further analysing departure conditions for heliocentric escape within an operational framework.

Another important aspect in the analysis of escape trajectories is the tidal effect of the Sun [34]. In the rotating frame centred at the secondary body, four quadrants are defined around it and numbered counterclockwise as illustrated in Fig. 2.1. The orientation of a spacecraft trajectory is characterised by the quadrant containing its apoapsis.

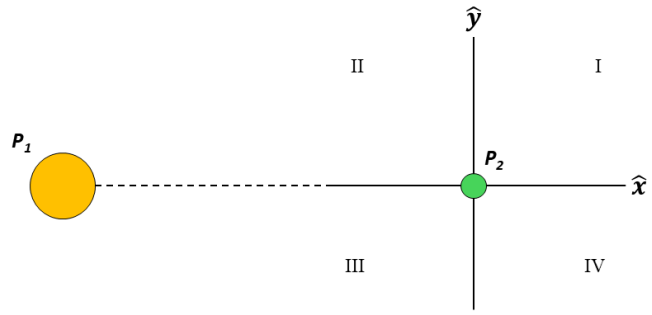

Figure 2.1: Quadrants as defined in the Sun-B1 rotating frame [34].

Within this framework, the tidal acceleration induced by the primary is predominantly directed outward from the secondary and acts most strongly near apoapsis. Its effect depends on the quadrant in which apoapsis lies. For prograde motion, apoapsis in quadrants I and III generally enhances orbital elongation and lowers periapsis radius, whereas apoapsis in quadrants II and IV tends to raise periapsis radius and promote orbital circularisation. Diagonal quadrants therefore exhibit similar dynamical behaviour. This quadrant-based interpretation explains the strong dependence of escape dynamics on the Sun-Earth-Moon geometry observed in NRHO disposal studies. In particular, such tidal effects become relevant once the spacecraft has departed from the periodic orbit and evolves freely in the Earth-Moon vicinity. The framework is therefore especially useful for interpreting indirect escape trajectories, which experience multiple apoapses before eventually transitioning toward heliocentric motion.

Based on Davis' studies [34], also the aforementioned works introduce the problem of the primaries relative geometry. Within the BCR4BP framework [30, 31, 35], the solar phase at the instant of the manoeuvre influences both the departure geometry and the subsequent evolution of the Sun-B_1 Hamiltonian.

Overall, these studies provide a structured dynamical interpretation of heliocentric disposal from NRHOs, highlighting the dependence on manoeuvre location, energy variation, and system geometry. However, most analyses remain primarily centred on specific manoeuvre configurations within the BCR4BP framework, while the geometric and dynamical structure underlying escape has not been investigated in a fully systematic manner. In particular, the role of the system configuration has not yet been examined through a systematic parametric approach.

Finally, a different perspective on NRHOs disposal is proposed by Bolis et al. [36], who address the design of EoL strategies within the coupled CR3BP framework. In contrast to BCR4BP-based approaches, heliocentric disposal is constructed by exploiting the unstable manifold of the reference NRHO in the Earth-Moon system and subsequently switching to the Sun-Earth CR3BP where the ZVC closure is enforced if the escape occurs. This manifold-driven energetic approach provides a structured way to design low-cost no-return trajectories while explicitly accounting for the geometric coupling between the two three-body systems. Among the open aspects identified in [36] is the need for a deeper investigation of the role played by the relative Sun-Earth-Moon configuration on escape success and cost. The present work builds directly on this framework, focusing precisely on a systematic and parametric analysis of the geometric dependence of heliocentric escape from Earth-Moon L2 NRHOs.

3 | Dynamical models

This Chapter presents the theoretical framework adopted in this work to model the spacecraft dynamics. The CR3BP is introduced and its main dynamical features are discussed, including Lagrange points, JC, ZVCs, periodic orbits, and invariant manifolds. The theory presented is based on standard references on the CR3BP [3, 7, 37].

3.1. Circular Restricted Three-Body Problem

The CR3BP is a fundamental model in astrodynamics used to study the motion of a small body under the gravitational influence of two massive primaries that follow circular orbits around their common center of mass. In this framework, the third body, typically the spacecraft, is assumed to have negligible mass compared to the primaries, such that its motion does not affect the dynamics of the two primary bodies.
The CR3BP is particularly useful for mission design and trajectory analysis in the Earth-Moon, Sun-Earth, and other planetary systems, where spacecraft or small satellites operate in regions dominated by the gravitational fields of two primary bodies. By using a reduced-order model, the CR3BP provides a framework to identify important dynamical elements, such as libration points, periodic orbits families, and their associated stable and unstable manifolds.
The CR3BP is based on the following already mentioned key assumptions:

- **Circular**: the primaries move in circular orbits around their centre of mass, neglecting orbital eccentricities.
- **Restricted**: the third body does not influence the motion of the primaries, allowing the problem to be treated as restricted.

Despite these assumptions, the CR3BP offers significant advantages: it reduces the full N-body problem to a manageable dynamical system, preserves the main qualitative features of a three-body interaction, and allows for the exploration of invariant structures such as stable and unstable manifolds. These structures provide natural "highways" for spacecraft to transfer between orbits with minimal energy expenditure, making the CR3BP an

invaluable tool for trajectory optimization, disposal design, and mission planning.

3.2. Reference frames

To analyse the dynamics of a body under the gravitational influence of the two primaries, two reference frames are commonly introduced: an inertial frame, denoted by the axes (X, Y, Z), and a rotating (synodic) frame, denoted by the axes (x, y, z), both centred in the centre of mass of the two larger bodies. Fig. 3.1 illustrates these frames, showing their relative orientation and axes. The two primary bodies are denoted as P_1 and P_2, representing the larger and smaller body, respectively, with masses m_1 and m_2.

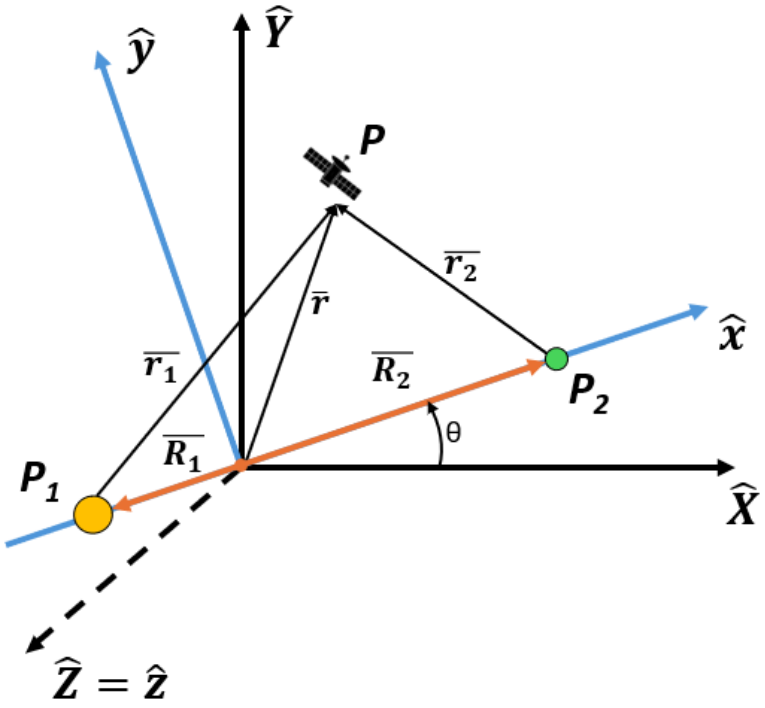

Figure 3.1: Inertial and rotating reference frame for the CR3BP [7].

The inertial frame is a non-rotating reference frame centred at the system's barycentre. The primaries move in the XY-plane, with the Z-axis perpendicular to it. The axes form a right-handed coordinate system.
The synodic frame is a non-inertial reference frame centred at the barycentre of the two primaries. Its x-axis is given by the line connecting the major to the minor primary and points toward it, the z-axis is perpendicular to the orbital plane, and the frame rotates with constant angular velocity equal to the mean motion of the primaries with respect to

the inertial frame. The y-axis completes the right-handed system.
The transformation between the inertial and rotating reference frames is defined as follows. Denoting by (X, Y, Z) and (x, y, z) the coordinates of the point P in the inertial and rotating frames, respectively, the position transformation can be written as:

$$\begin{pmatrix} X \\ Y \\ Z \end{pmatrix} = A(t) \begin{pmatrix} x \\ y \\ z \end{pmatrix} \tag{3.1}$$

where

$$A(t) = \begin{pmatrix} \cos\theta & -\sin\theta & 0 \\ \sin\theta & \cos\theta & 0 \\ 0 & 0 & 1 \end{pmatrix} \tag{3.2}$$

By differentiating Eq. (3.1) with respect to time, the transformation of the velocity components is obtained as:

$$\begin{pmatrix} \dot{X} \\ \dot{Y} \\ \dot{Z} \end{pmatrix} = A(t) \begin{pmatrix} \dot{x} - y \\ \dot{y} + x \\ \dot{z} \end{pmatrix} \tag{3.3}$$

3.3. Equation of motion in the inertial frame

The equations of motion in the inertial reference frame can be obtained starting from the general N-body gravitational model. The motion of each body is described by its position vector $\mathbf{R}_i$, measured with respect to a fixed inertial origin O. Under the assumption that all bodies can be treated as point masses, the application of Newton's second law leads to

$$\ddot{\mathbf{R}}_i = -G \sum_{\substack{j=1 \\ j \neq i}}^{N} m_j \frac{\mathbf{R}_i - \mathbf{R}_j}{\|\mathbf{R}_i - \mathbf{R}_j\|^3}, \qquad i = 1, \ldots, N \tag{3.4}$$

where G is the gravitational constant and time is chosen as the independent variable. By restricting the formulation to the case $N = 3$, Eq. (3.4) describes the dynamics of the three-body problem in an inertial reference frame. Considering the notation reported in Fig. 3.1 the expression becomes:

$$\ddot{\mathbf{r}} = -G\frac{m_1}{r_1^3}\mathbf{r}_1 - G\frac{m_2}{r_2^3}\mathbf{r}_2 \tag{3.5}$$

where the position of the primaries is:

$$\begin{aligned} \mathbf{R}_1 &= R_1\big(-\cos(\theta)\,\hat{\mathbf{X}} - \sin(\theta)\,\hat{\mathbf{Y}}\big) \\ \mathbf{R}_2 &= R_2\big(\cos(\theta)\,\hat{\mathbf{X}} + \sin(\theta)\,\hat{\mathbf{Y}}\big) \end{aligned} \tag{3.6}$$

The position vector of P and the relative position of P with respect to the primaries is:

$$\mathbf{r} = X\,\hat{\mathbf{X}} + Y\,\hat{\mathbf{Y}} + Z\,\hat{\mathbf{Z}} \tag{3.7}$$

$$\begin{aligned} \mathbf{r}_1 &= (X + R_1\cos(\theta))\,\hat{\mathbf{X}} + (Y + R_1\sin(\theta))\,\hat{\mathbf{Y}} + Z\,\hat{\mathbf{Z}} \\ \mathbf{r}_2 &= (X - R_2\cos(\theta))\,\hat{\mathbf{X}} + (Y - R_2\sin(\theta))\,\hat{\mathbf{Y}} + Z\,\hat{\mathbf{Z}} \end{aligned} \tag{3.8}$$

The equations of motion for the third body, P_3, in the inertial reference frame can be derived by substituting the expressions in Eq. (3.5) and taking into account that these are second-order differential equations. In component form, they can be written as

$$\begin{cases} \ddot{X} = -G\,m_1\dfrac{X + R_1\cos(\dot{\theta}t)}{R_1^3} - G\,m_2\dfrac{X - R_2\cos(\dot{\theta}t)}{R_2^3} \\ \ddot{Y} = -G\,m_1\dfrac{Y + R_1\sin(\dot{\theta}t)}{R_1^3} - G\,m_2\dfrac{Y - R_2\sin(\dot{\theta}t)}{R_2^3} \\ \ddot{Z} = -G\,m_1\dfrac{Z}{R_1^3} - G\,m_2\dfrac{Z}{R_2^3} \end{cases} \tag{3.9}$$

where R_1 and R_2 represent the distances between P and the two primary bodies. Since the system of equations in Eq. (3.9) is nonlinear and second-order, no closed-form analytical solution exists. Therefore, numerical integration techniques are typically employed to study the evolution of the state of P over time.

3.4. Equation of motion in the rotating frame

The CR3BP is commonly formulated in the rotating reference frame, as this choice leads to a simpler mathematical description of the dynamics. In this frame, the relative positions of the primaries remain fixed, which facilitates the identification of recurrent patterns, invariant structures, and dynamically significant trajectories. Moreover, the rotating frame naturally introduces conserved quantities, such as the Jacobi integral, and provides a convenient setting for the analysis of equilibrium points and their associated invariant manifolds.

It is now necessary to introduce the nondimensionalisation of the problem, which allows the equations of motion to be expressed by appropriately scaling lengths, masses, and

time. Through this process, the number of governing parameters is reduced and the numerical conditioning of the problem is improved. The following parameters are therefore introduced to nondimensionalise the problem:

- **Mass:** the total mass of the primaries is used, $m_1 + m_2$. The resulting nondimensional masses are $\mu = \frac{m_2}{m_1+m_2}$ for P_2 and $1-\mu = \frac{m_1}{m_1+m_2}$ for P_1.
- **Length:** the characteristic length is taken as the mean distance between P_1 and P_2. Therefore, P_2 is located at $1-\mu$ and P_1 at $-\mu$.
- **Time:** the time unit is chosen such that the orbital period of P_1 and P_2 rotating in circular motion about their common centre of mass is 2π.

With this choice of units, the gravitational constant is normalised to $G = 1$, and the mean motion of the primaries is also unity.
Rewriting the Eq. (3.5) in the nondimesional units, Eq. (3.10) is obtained:

$$\ddot{\mathbf{r}} = -\frac{1-\mu}{r_1^3}\mathbf{r}_1 - \frac{\mu}{r_2^3}\mathbf{r}_2 \tag{3.10}$$

where r_1 and r_2 are the distances of the satellite to the major and the minor primary, respectively.

$$\begin{aligned} r_1 &= \sqrt{(x+\mu)^2 + y^2 + z^2} \\ r_2 &= \sqrt{(x-1+\mu)^2 + y^2 + z^2}. \end{aligned} \tag{3.11}$$

Equation (3.10) describes the motion of the massless body in nondimensional form with respect to the inertial reference frame. To express the dynamics in the rotating frame, it is necessary to relate time derivatives taken in the inertial frame to those evaluated in the rotating frame.
Let the rotating reference frame rotate with constant angular velocity $\boldsymbol{\omega} = \hat{z}$ with respect to the inertial frame. The first time derivative of the position vector can then be written as

$$\frac{d\mathbf{r}}{dt} = \dot{\mathbf{r}} + \boldsymbol{\omega} \times \mathbf{r} \tag{3.12}$$

where the overdot denotes differentiation with respect to the nondimensional time in the rotating frame.
Taking the time derivative of Eq. (3.12) and noting that $\boldsymbol{\omega}$ is constant, the inertial acceleration becomes

$$\frac{d^2\mathbf{r}}{dt^2} = \ddot{\mathbf{r}} + 2\,\boldsymbol{\omega} \times \dot{\mathbf{r}} + \boldsymbol{\omega} \times (\boldsymbol{\omega} \times \mathbf{r}) \tag{3.13}$$

where the additional terms represent the Coriolis and centrifugal accelerations, respectively.

Substituting Eq. (3.13) into Eq. (3.10) and rearranging, the equations of motion expressed in the rotating reference frame are obtained. Projecting the resulting vector equation along the axes of the rotating frame yields the scalar equations of motion of the CR3BP. The equations of motion in the rotating reference frame can therefore be written in vector form as

$$\ddot{\mathbf{r}} = -\frac{1-\mu}{r_1^3}\mathbf{r}_1 - \frac{\mu}{r_2^3}\mathbf{r}_2 - 2\,\boldsymbol{\omega} \times \dot{\mathbf{r}} - \boldsymbol{\omega} \times (\boldsymbol{\omega} \times \mathbf{r}) \tag{3.14}$$

where $\boldsymbol{\omega} = \hat{z}$ is the constant angular velocity of the rotating frame.
By projecting Eq. (3.14) along the axes of the rotating reference frame, the scalar equations of motion of the CR3BP are obtained:

$$\begin{cases} \ddot{x} = 2\dot{y} + x - \dfrac{1-\mu}{r_1^3}(x+\mu) - \dfrac{\mu}{r_2^3}(x-1+\mu) \\ \ddot{y} = -2\dot{x} + y - \dfrac{1-\mu}{r_1^3}y - \dfrac{\mu}{r_2^3}y \\ \ddot{z} = -\dfrac{1-\mu}{r_1^3}z - \dfrac{\mu}{r_2^3}z \end{cases} \tag{3.15}$$

It is convenient to rewrite the equations of motion in the rotating reference frame by introducing a scalar effective potential function. To this end, the gravitational and centrifugal terms appearing in Eq. (3.15) can be grouped into a single scalar function $U(x, y, z)$, defined as

$$U(x, y, z) = \frac{1}{2}\left(x^2 + y^2\right) + \frac{1-\mu}{r_1} + \frac{\mu}{r_2} \tag{3.16}$$

The partial derivatives of the effective potential with respect to the rotating frame coordinates are given by

$$\begin{cases} \dfrac{\partial U}{\partial x} = x - \dfrac{1-\mu}{r_1^3}(x+\mu) - \dfrac{\mu}{r_2^3}(x-1+\mu) \\ \dfrac{\partial U}{\partial y} = y - \dfrac{1-\mu}{r_1^3}y - \dfrac{\mu}{r_2^3}y \\ \dfrac{\partial U}{\partial z} = -\dfrac{1-\mu}{r_1^3}z - \dfrac{\mu}{r_2^3}z \end{cases} \tag{3.17}$$

By substituting the expressions in Eq. (3.17) into the scalar equations of motion, the equations of the CR3BP can be written in compact form as

$$\begin{cases} \ddot{x} - 2\dot{y} = \dfrac{\partial U}{\partial x} \\ \ddot{y} + 2\dot{x} = \dfrac{\partial U}{\partial y} \\ \ddot{z} = \dfrac{\partial U}{\partial z} \end{cases} \tag{3.18}$$

3.5. Lagrange points

The Lagrange (or libration) points are equilibrium solutions of the CR3BP. Their locations are obtained by first rewriting the Equations of Motion (EoM) in first-order form, $\dot{\mathbf{x}} = \mathbf{f}(\mathbf{x})$, shown in Eqs. (3.19) and then imposing the equilibrium condition $\mathbf{f}(\mathbf{x}) = \mathbf{0}$.

$$\begin{cases} \dot{x} = v_x \\ \dot{y} = v_y \\ \dot{z} = v_z \\ \dot{v}_x = 2v_y + \dfrac{\partial U}{\partial x} \\ \dot{v}_y = -2v_x + \dfrac{\partial U}{\partial y} \\ \dot{v}_z = \dfrac{\partial U}{\partial z} \end{cases} \tag{3.19}$$

The result is that $v_x = v_y = v_z = 0$, and the partial derivatives of the potential U with respect to the spatial coordinates x, y and z are null. Eq. (3.20) shows the condition for the Lagrange points.

$$\begin{cases} 0 = x - \dfrac{1-\mu}{r_1^3}(x+\mu) - \dfrac{\mu}{r_2^3}(x-1+\mu) \\ 0 = y - \dfrac{1-\mu}{r_1^3}y - \dfrac{\mu}{r_2^3}y \\ 0 = -\dfrac{1-\mu}{r_1^3}z - \dfrac{\mu}{r_2^3}z \end{cases} \tag{3.20}$$

From the third equation in Eq. (3.20), it follows that the equilibrium solutions satisfy $z = 0$, thus all Lagrange points lie in the synodic plane. The second equation in Eq. (3.20) can be rewritten by collecting the y-coordinate as

$$y\left(1 - \frac{1-\mu}{r_1^3} - \frac{\mu}{r_2^3}\right) = 0 \tag{3.21}$$

This condition admits two distinct classes of solutions: either $y = 0$, which leads to equilibrium points aligned with the primaries along the x-axis, or $y \neq 0$, in which case the term in parentheses should be equal to zero, giving rise to the triangular equilibrium configurations.

In the first case, by imposing $y = 0$, the second equation in Eq. (3.20) is identically satisfied, while the equilibrium condition reduces to a single scalar equation along the x-direction

$$x - \frac{1-\mu}{r_1^3}(x+\mu) - \frac{\mu}{r_2^3}(x-1+\mu) = 0 \tag{3.22}$$

which admits three real solutions corresponding to the collinear Lagrange points L_1, L_2, and L_3.

When $y \neq 0$, the second equation in Eq. (3.20) yields the additional condition

$$1 - \frac{1-\mu}{r_1^3} - \frac{\mu}{r_2^3} = 0 \tag{3.23}$$

A solution is obtained by imposing $r_1 = r_2 = 1$ which, together with $z = 0$, also satisfies the first equilibrium equation by symmetry. This configuration corresponds to two points forming equilateral triangles with the primaries and identifies the triangular Lagrange points L_4 and L_5.

Fig.3.2 shows the location of the five Lagrange points in the synodic reference frame, highlighting the collinear points L_1, L_2, and L_3 along the line connecting the primaries, and the triangular points L_4 and L_5. Although the CR3BP has been treated in a general form without specifying the mass parameter μ, a specific value is required for visualization purposes. In Fig.3.2, the Earth-Moon system is considered, where the spatial coordinates are expressed in ndL (non-dimensional Length), adopted in the CR3BP formulation.

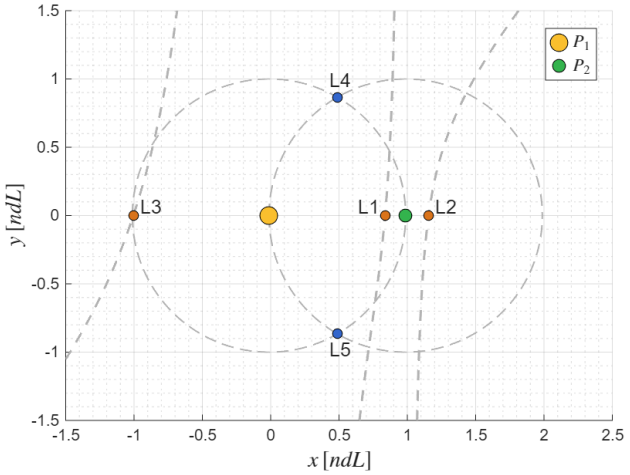

Figure 3.2: Lagrange points

3.6. Jacobi Constant and Zero Velocity Curves

The CR3BP admits an integral of motion known as the JC. This quantity can be derived by manipulating the equations of motion expressed in the rotating reference frame, given in Eq. (3.18).
By multiplying the second-order equations by $\dot{x}$, $\dot{y}$, and $\dot{z}$, respectively, and summing them, one obtains

$$\dot{x}\ddot{x} + \dot{y}\ddot{y} + \dot{z}\ddot{z} = \dot{x}\frac{\partial U}{\partial x} + \dot{y}\frac{\partial U}{\partial y} + \dot{z}\frac{\partial U}{\partial z} \tag{3.24}$$

The right-hand side of Eq. (3.24) corresponds to the total time derivative of the effective potential U, which can be obtained through the chain rule

$$\frac{dU}{dt} = \frac{\partial U}{\partial x}\dot{x} + \frac{\partial U}{\partial y}\dot{y} + \frac{\partial U}{\partial z}\dot{z} \tag{3.25}$$

Substituting Eq. (3.25) into Eq. (3.24) and integrating with respect to time yields

$$\dot{x}^2 + \dot{y}^2 + \dot{z}^2 = 2U - JC \tag{3.26}$$

where JC is the constant of integration. Introducing the squared magnitude of the velocity in the rotating reference frame as $V^2 = \dot{x}^2 + \dot{y}^2 + \dot{z}^2$, Eq. (3.26) can be written in the compact form

$$V^2 = 2U - JC \tag{3.27}$$

Moreover, Eq. (3.27) provides a clear energy interpretation of the motion in the rotating frame, for a given value of JC, the kinetic energy is uniquely determined by the effective potential U. The JC therefore represents a conserved energy quantity and constitutes a fundamental tool for analysing the admissible regions of motion in the CR3BP.
Since the squared magnitude of the velocity must be non-negative, the condition $V^2 \geq 0$ must be satisfied. This requirement defines a constraint on the admissible motion, which can be expressed as $U \geq JC/2$. As a consequence, the regions of space where $U < JC/2$ are dynamically forbidden, as they would correspond to an imaginary velocity. The boundary between allowed and forbidden regions is defined by

$$U = \frac{JC}{2} \tag{3.28}$$

which identifies the so-called Zero Velocity Surfaces (ZVSs).
Fig.3.3 reports the ZVSs for the Earth-Moon system at values of the JC equal to those associated with the Lagrange points. The green marker indicates the first primary (Earth), while the yellow marker denotes the second primary (Moon).

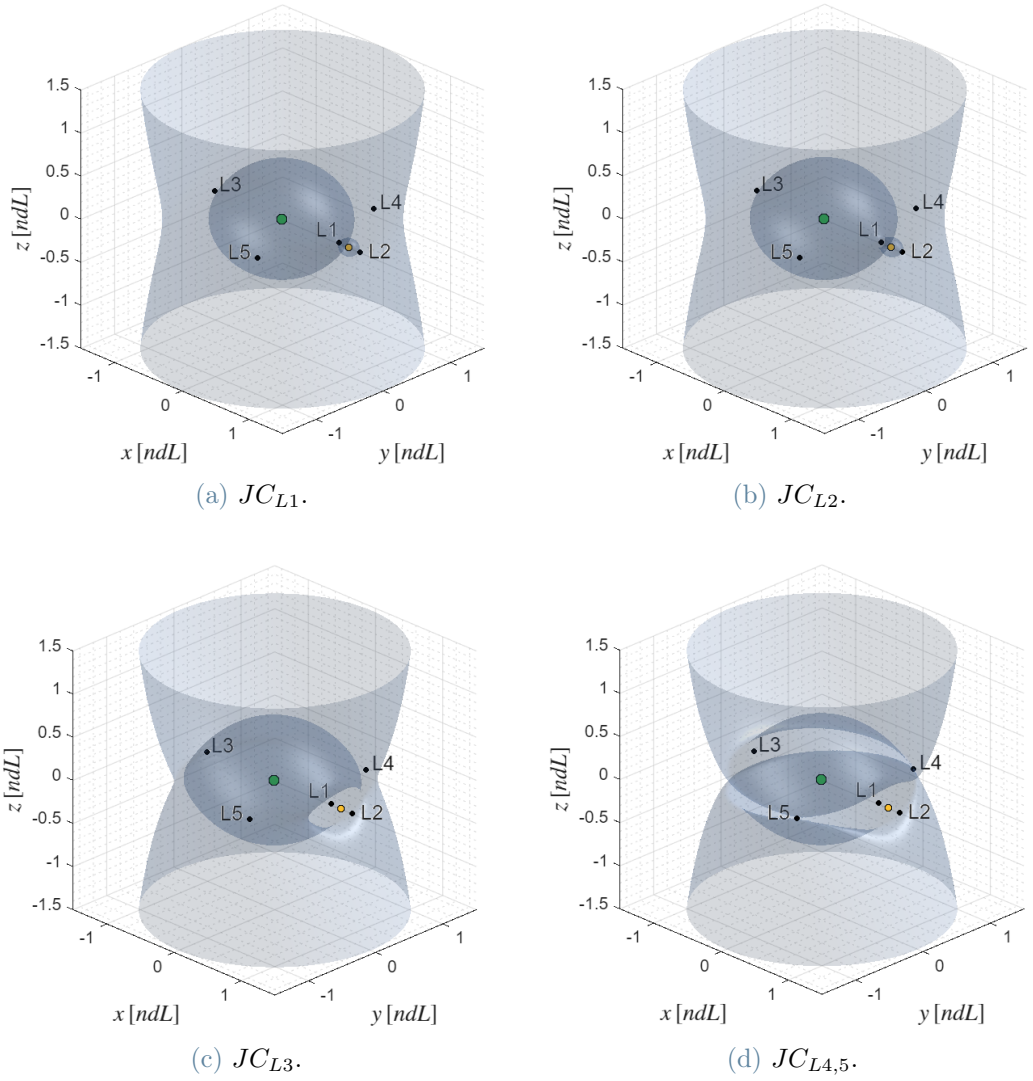

(a) JC_{L1}. (b) JC_{L2}.

(c) JC_{L3}. (d) $JC_{L4,5}$.

Figure 3.3: ZVS at the JC corresponding to the Lagrange points.

By restricting the analysis to planar motion, the ZVS reduce to ZVCs, which provide a convenient two-dimensional representation of the admissible regions of motion. As already observed for the ZVSs, the topology of the corresponding curves depends on the value of the JC and undergoes significant changes as JC varies, governing the opening and closure of the neck regions around the collinear Lagrange points. In the following, the evolution of the ZVCs as a function of JC is analysed to characterise the corresponding regimes of motion, as shown in Fig. 3.4 for the Earth-Moon and Sun-Earth systems. In the Earth-Moon case, the green and yellow markers denote the Earth and the Moon, respectively, while in the Sun-Earth case the green marker indicates the Earth-Moon barycenter.

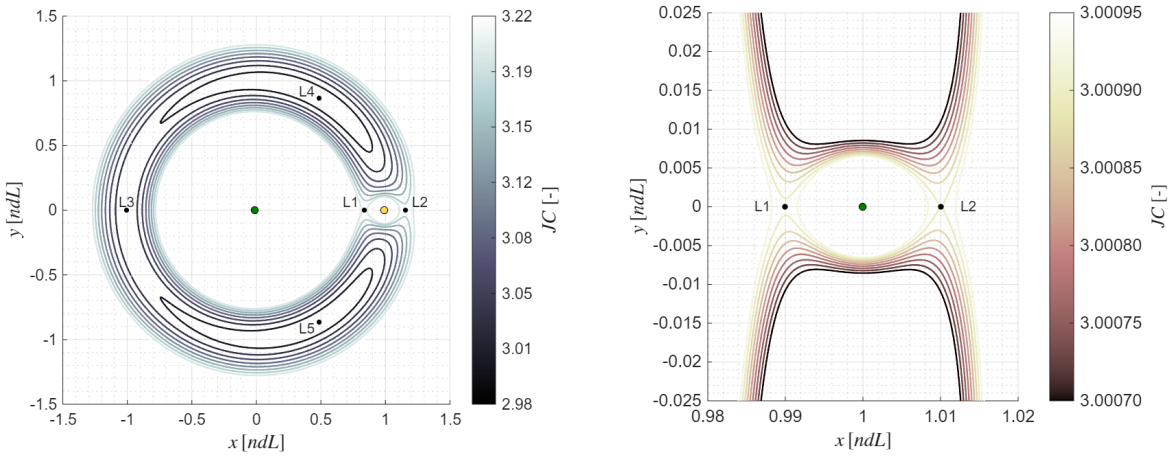

(a) Earth-Moon ZVC.

(b) Sun-Earth ZVC.

Figure 3.4: ZVCs in the rotating frame for the Earth-Moon and Sun-Earth systems at different values of the JC. For the Sun-Earth system, the view is restricted to the region of interest around the libration point to better highlight the local structure of the curves.

The region bounded by the ZVCs, shown in Fig. 3.4, corresponds to a dynamically forbidden domain, where the spacecraft cannot be located according to the constraint imposed by the JC. For a given configuration, lower values of the spacecraft energy are associated with higher values of JC, resulting in progressively more closed ZVC around the collinear Lagrange points. As a consequence, the accessibility of the neck regions near L_1 and L_2 strongly depends on the value of the JC.
This property is fundamental for determining whether a trajectory is allowed to pass through the neck regions associated with the collinear Lagrange points, thereby enabling or preventing access to different dynamical regions of the system. In particular, it plays a crucial role in heliocentric disposal analysis: if the spacecraft energy is insufficient, the ZVCs remain closed at the collinear points and escape from the cislunar system is not possible. The JC must therefore be such that the ZVCs are open at the relevant neck regions, allowing the spacecraft to leave the cislunar environment.

3.7. Periodic orbits and manifold dynamics

In addition to equilibrium points, the CR3BP admits families of periodic orbits. These solutions arise in the vicinity of the Lagrange points, in particular around the collinear ones, and correspond to motions that repeat after a fixed period in the rotating reference frame. Periodic orbits provide reference trajectories that are useful to describe the local dynamical behaviour of the system and for introducing the associated invariant manifold

structures. In particular, the dynamical structure of the CR3BP is further characterised by invariant manifolds associated with unstable periodic orbits, typically those surrounding the collinear Lagrange points. These manifolds are invariant sets of the flow and consist of families of trajectories that asymptotically approach or depart from a given periodic orbit, thereby shaping the global phase-space dynamics of the system.
Two distinct types of invariant manifolds can be identified:

- **Stable manifolds** consist of trajectories that asymptotically converge toward the periodic orbit in forward time
- **Unstable manifolds** consist of trajectories that asymptotically depart from a periodic orbit in forward time

From a physical perspective, invariant manifolds act as natural pathways that organise the transport within the CR3BP, guiding the motion of a spacecraft through different dynamical regions without requiring large control efforts. Fig.3.5 shows the stable and unstable manifold, respectively in orange and blue, for an Earth-Moon L2 LPO.

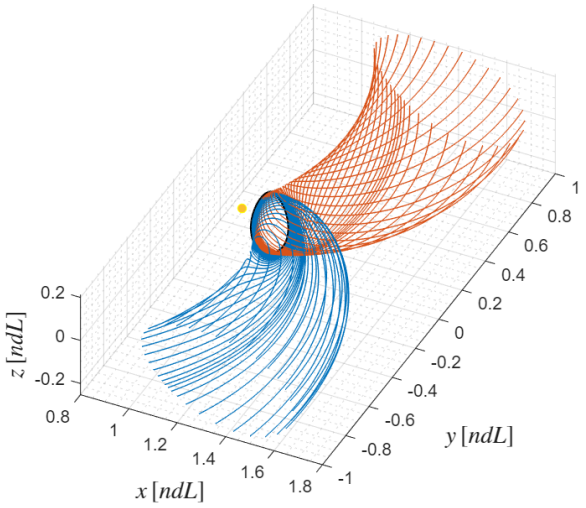

Figure 3.5: Stable and unstable invariant manifolds for a LPO

A key feature of invariant manifold dynamics is its role in enabling transport through the neck regions associated with the collinear Lagrange points. When the ZVCs are open, unstable manifolds provide dynamically admissible routes for escape from the cislunar region, while stable manifolds can guide trajectories toward capture. As such, invariant manifolds establish a direct connection between the local dynamics near LPOs and the global energy constraints imposed by the JC, making them a fundamental tool for the analysis of escape and disposal trajectories. The numerical computation and exploitation of invariant manifolds will be addressed in the following Chapter.

3.8. Coupled Circular Restricted Three-Body Problem

Throughout the Thesis, the CR3BP will be applied to both the Earth-Moon and the Sun-Earth systems. These two models will be used in a coupled manner to describe trajectories between the cislunar and heliocentric environments. This implies that the spacecraft dynamics are described by the Earth-Moon CR3BP when the gravitational influence of the Moon dominates over that of the Sun. As the trajectory evolves away from the cislunar region, the relative influence of the Sun increases and the propagation is accordingly performed within the Sun-Earth CR3BP. The transition between the two models is based on the definition of prevalence regions, which define the domain of validity of each formulation. The computation of these regions, as well as the transformation between the corresponding reference frames, is described in detail by Castelli [38]. The three bodies are assumed to be coplanar and lay on the ecliptic plane, Fig.3.6 shows the relation between the two reference frames.

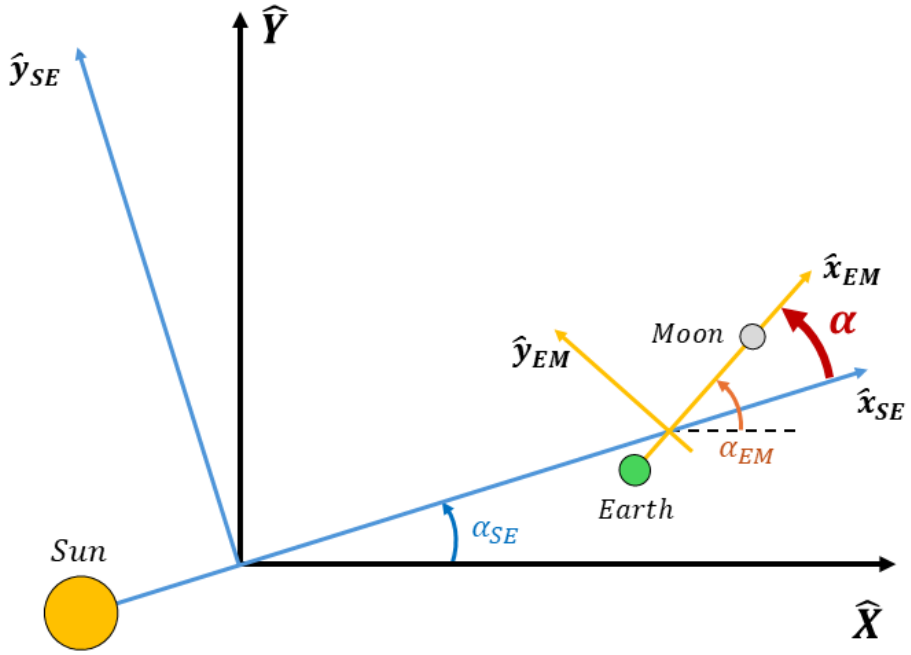

Figure 3.6: Relation between the Sun-Earth and Earth-Moon CR3BP rotating frames [38].

The angle α represents the relative rotation between the Earth-Moon and Sun-Earth rotating frames and fully characterises their instantaneous mutual orientation.
Following the approach proposed by Castelli [38], the coupled CR3BP approximation is constructed by comparing each restricted three-body model with a more complete

four-body description of the Sun-Earth-Moon system, represented by the BCR4BP. The discrepancy between the CR3BP dynamics and the BCR4BP one is evaluated locally in the configuration space by comparing the corresponding equations of motion once they are expressed in a common reference frame. In the Earth-Moon case, this comparison is performed by representing the position of the test particle in complex form in the Sun-Earth rotating frame. Denoting by X_m and Y_m the non-dimensional coordinates in the Earth-Moon synodic frame, the corresponding complex variable is defined as

$$\eta_m = X_m + i\, Y_m. \tag{3.29}$$

The position is then mapped to the Earth-Moon length scale by means of the characteristic distance L_m,

$$\bar{\eta}_{em} = L_m\, \eta_m, \tag{3.30}$$

where the overbar denotes quantities expressed in dimensional form.
The position of the Sun, Earth and Moon expressed in the Earth-Moon rotating frame under the planar assumption, can be written as

$$\begin{aligned} \bar{S}_{em} &= -L_s\, e^{i(-\alpha)}, \\ \bar{E}_{em} &= -\mu_m L_m, \\ \bar{M}_{em} &= (1-\mu_m) L_m. \end{aligned} \tag{3.31}$$

where L_s is the Sun-Earth characteristic distance. The perturbing acceleration induced by the Sun in the Bicircular model, relative to the reference acceleration at the Earth-Moon barycentre, can be expressed as

$$\delta_{EM} = GM_s \left| \frac{\bar{S}_{em} - \bar{\eta}_{em}}{\left|\bar{\eta}_{em} - \bar{S}_{em}\right|^3} - \frac{\bar{S}_{em} - \bar{B}_{em}}{\left|\bar{S}_{em} - \bar{B}_{em}\right|^3} \right|, \tag{3.32}$$

where G is the gravitational constant, M_s is the Sun mass, $\bar{B}_{em}$ denotes the Earth-Moon barycentre expressed in the same frame that is equal to 0. Fig. 3.7 shows the discrepancy between the Earth-Moon CR3BP and the BCR4BP. This difference arises from the fact that, in the Earth-Moon CR3BP, the gravitational influence of the Sun on the spacecraft is approximated by the acceleration experienced by the Earth-Moon barycentre. As a consequence, the discrepancy vanishes at the origin of the rotating frame and increases as the spacecraft moves away from it. In the following figures, ndL is normalised with respect to the Earth-Moon distance for the Earth-Moon system and to the Sun-(Earth+Moon) barycentre distance for the Sun-Earth system.

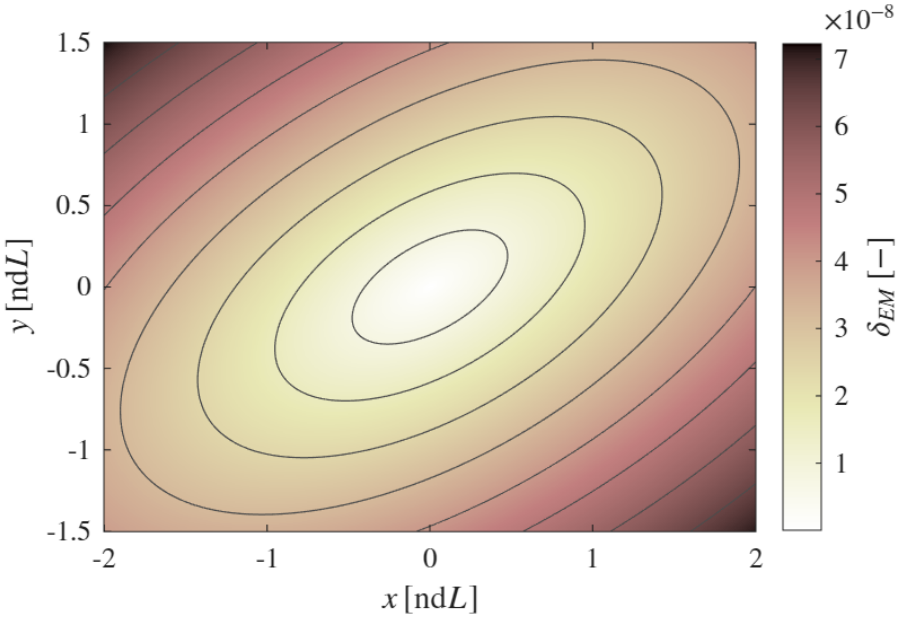

Figure 3.7: Level curves of Δ_{EM} for $\alpha = \pi/3$.

In the Sun-Earth rotating frame, the dimensional positions of the primaries are

$$\begin{aligned} \bar{S}_{se} &= -\mu_s L_s, \\ \bar{E}_{se} &= (1-\mu_s)L_s - \mu_m L_m e^{i(\alpha)}, \\ \bar{M}_{se} &= (1-\mu_s)L_s + (1-\mu_m)L_m e^{i(\alpha)}, \end{aligned} \tag{3.33}$$

and the Earth-Moon barycentre in the same frame is defined as

$$\bar{B}_{se} = \frac{M_e \bar{E}_{se} + M_m \bar{M}_{se}}{M_b}, \qquad M_b = M_e + M_m. \tag{3.34}$$

The discrepancy between the Bicircular model and the Sun-(Earth+Moon) CR3BP is then evaluated as

$$\delta_{SE}(\bar{\eta}) = G \left| -\frac{M_e(\bar{\eta} - \bar{E}_{se})}{\left|\bar{\eta} - \bar{E}_{se}\right|^3} - \frac{M_m(\bar{\eta} - \bar{M}_{se})}{\left|\bar{\eta} - \bar{M}_{se}\right|^3} + \frac{M_b(\bar{\eta} - \bar{B}_{se})}{\left|\bar{\eta} - \bar{B}_{se}\right|^3} \right|. \tag{3.35}$$

δ_{SE} originates from the approximation adopted in the Sun-Earth CR3BP, where the Earth-Moon system is modeled as a single body concentrated at its barycentre rather than as a binary system. As shown in Fig. 3.8, the difference between the Bicircular model and the restricted formulation is significant only in the vicinity of the Earth and the Moon, while it rapidly decreases as the evaluation point moves away from the primaries, becoming negligible outside two localised regions surrounding them.

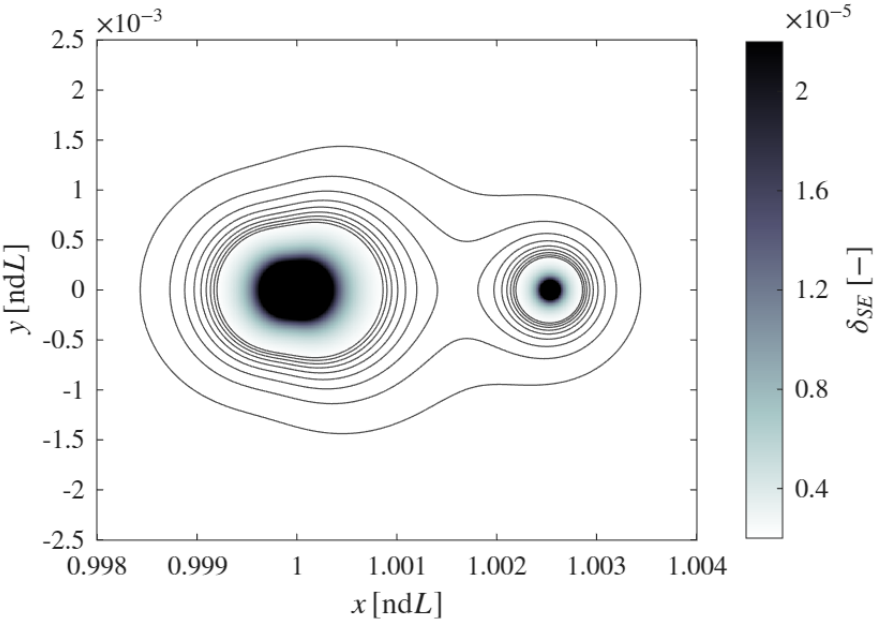

Figure 3.8: Level curves of Δ_{SE} for $\alpha = 0$.

By performing this analysis for both the Earth-Moon and the Sun-Earth CR3BP, regions of prevalence are identified, defining the spatial domains where one restricted problem provides a better local approximation of the Bicircular model than the other. The boundary between these regions is given by the zero level set of the difference between the two approximation errors, and it varies with the relative configuration of the primaries. These regions of prevalence provide a physically motivated criterion for selecting the appropriate CR3BP formulation along a trajectory. Figs. 3.9a and 3.9b show respectively the prevalence regions in Earth-Moon and Sun-Earth system.

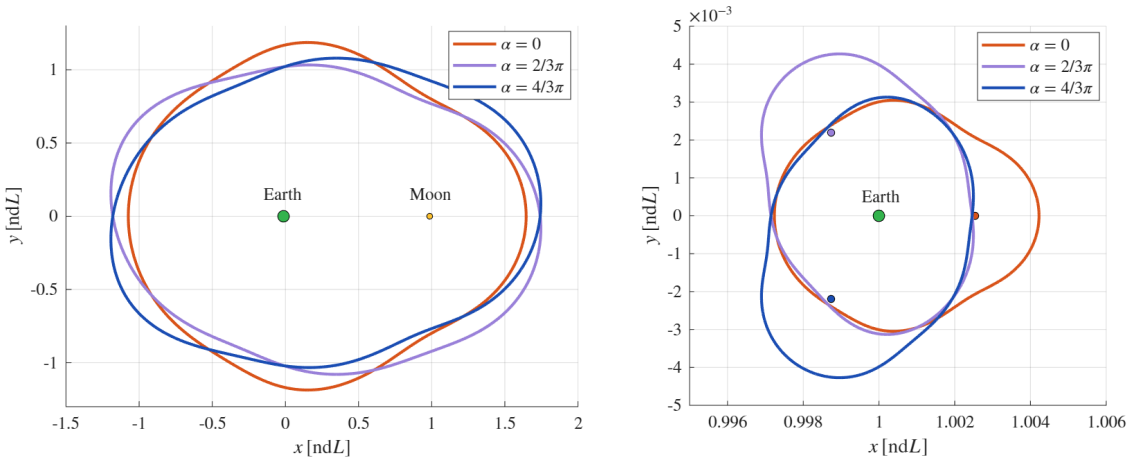

(a) Earth-Moon reference frames.

(b) Sun-Earth reference frame.

Figure 3.9: Regions of prevalence

Within this framework, the transition between the Earth-Moon and Sun-Earth models is performed when the trajectory crosses the prevalence boundary. This requires the transformation of the spacecraft state between the corresponding rotating reference frames, which involves both coordinate and velocity mappings accounting for the relative motion of the primaries.

For the implementation of the coupled CR3BP framework, it is necessary to convert the spacecraft state between the Earth-Moon and Sun-Earth rotating reference frames. Denoting by η_m and η_s the spacecraft position in the Earth-Moon and Sun-Earth synodic frames, respectively, the conversion from the Earth-Moon frame to the Sun-Earth frame reads

$$\eta_s = \frac{L_M}{L_S} e^{i\alpha} \eta_m + (1 - \mu_s), \tag{3.36}$$

The corresponding transformation of the velocity is given by

$$\frac{d\eta_s}{dt_s} = \frac{L_M}{L_S} \frac{\omega_{SE}}{\omega_{EM}} e^{i\alpha} \left[i \left(1 - \frac{\omega_{EM}}{\omega_{SE}} \right) \eta_m + \frac{d\eta_m}{dt_m} \right], \tag{3.37}$$

The out-of-plane coordinate has not been explicitly mentioned so far, since the two systems are assumed to be coplanar and the Z component is not relevant for the definition of the regions of prevalence. Nevertheless, the Z coordinate and its corresponding velocity component dZ/dt must also be transformed when switching between reference frames. In this case, the transformation reduces to a simple scaling, given by

$$Z_s = Z_m \frac{L_M}{L_S} \tag{3.38}$$

$$\frac{dZ_s}{dt_s} = \frac{dZ_m}{dt_m} \frac{L_M}{L_S} \frac{\omega_{EM}}{\omega_{SE}} \tag{3.39}$$

with ω_{EM} and ω_{SE} denoting the angular velocities of the Earth-Moon and Sun-Earth rotating frames.

The rotation angle α accounts for the relative orientation of the two synodic frames and evolves in time according to

$$\alpha = \alpha_0 + \frac{\omega_{EM} - \omega_{SE}}{\omega_{EM}} t_{EM}, \tag{3.40}$$

when expressed in Earth-Moon nondimensional time. Equivalently, in Sun-Earth nondimensional time, it can be written as

$$\alpha = \alpha_0 + \frac{\omega_{EM} - \omega_{SE}}{\omega_{SE}} t_{SE}. \tag{3.41}$$

These relations allow a consistent mapping of the spacecraft state between the two CR3BP formulations and provide the basis for the numerical implementation of the coupled model.

4 | Framework for Near Rectilinear Halo Orbits escape analysis

As introduced in Chapter 1, heliocentric escape is analysed to characterise its behaviour, with the aim of supporting the study of disposal strategies for NRHOs in the context of future missions. This Section describes the numerical methodology adopted to compute these orbits and the entire family of halo orbits around the Earth-Moon L2 point, highlighting the features that define NRHOs within this family.

4.1. Halo orbits family

Halo orbits are three-dimensional periodic solutions of the CR3BP that exist in the vicinity of the collinear libration points. In the Earth-Moon system, the family of halo orbits around the L_2 point includes members that range from nearly planar close periodic trajectories, corresponding Lyapunov orbit, to strongly three-dimensional orbits that extend toward the lunar region.

In the CR3BP, an orbit is periodic if the state of the system repeats exactly after a finite time period. Due to the symmetry of the EoMs with respect to the xz-plane, periodic orbits around the collinear libration points can be constructed by enforcing symmetry conditions at a plane crossing. In particular, as discussed in [3, 7], halo orbits are typically obtained by requiring an orthogonal crossing of the xz-plane at half-period. These conditions are enforced numerically through a differential correction procedure, which is described in the following Section. Fig. 4.1 shows the family of Earth-Moon L_2 halo orbits, with the trajectory colour varying according to the JC and the perilune radius in Figs. 4.1a and 4.1b, respectively.

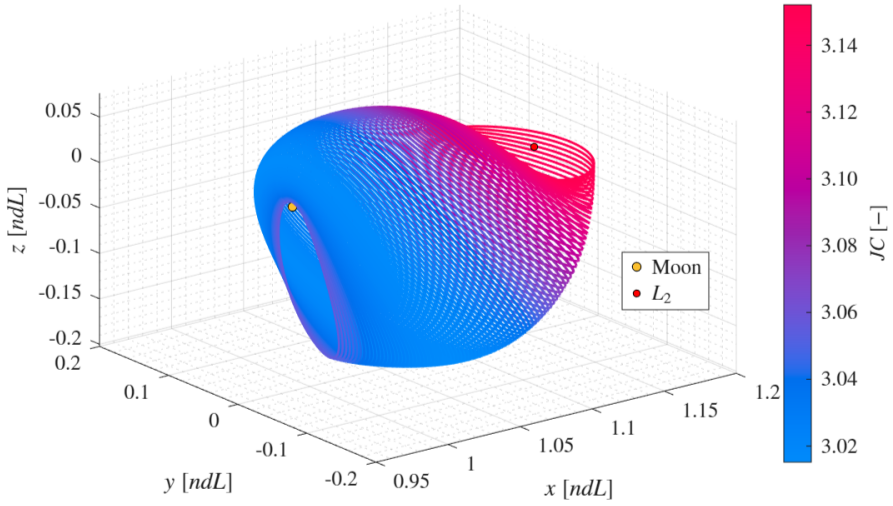

(a) Halo orbits as a function of JC.

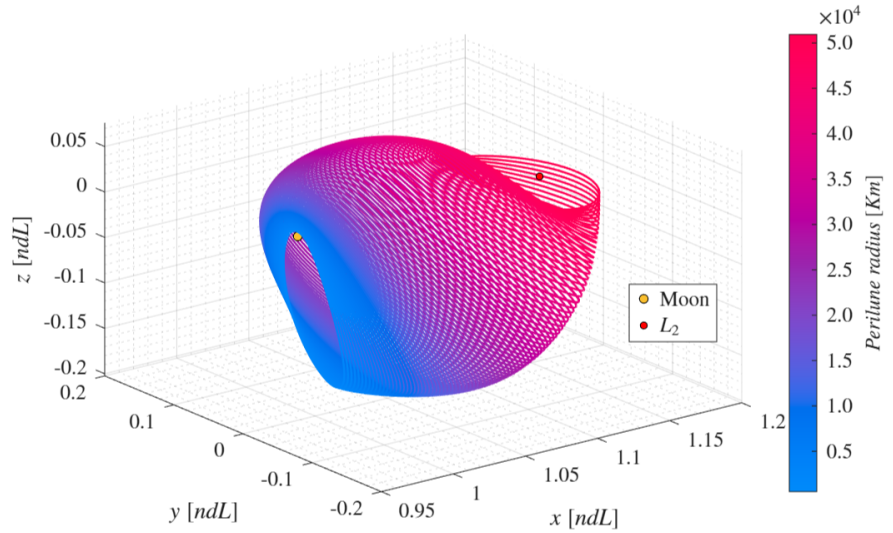

(b) Halo orbits family as a function of perilune radius.

Figure 4.1: Earth-Moon L2 Halo orbits family.

4.2. Numerical methods for periodic orbits computation

This Section describes the numerical techniques employed to compute families of periodic orbits, including differential correction and numerical continuation. The problem consists in determining suitable initial conditions such that the symmetry conditions required for periodicity, including an orthogonal crossing of the xz-plane, are satisfied. In this context, the State Transition Matrix (STM) is introduced as a key tool.
The STM describes the linearised evolution of small perturbations along a reference tra-

jectory of the dynamical system [3]. Let $\boldsymbol{\varphi}(t; \mathbf{x}_0)$ denotes the flow map of the CR3BP, mapping an initial state $\mathbf{x}_0$ at time t_0 to the corresponding state $\mathbf{x}(t)$ at time t. A small perturbation $\delta\mathbf{x}_0$ applied to the initial condition evolves according to

$$\delta\mathbf{x}(t) = \boldsymbol{\varphi}(t; \mathbf{x}_0 + \delta\mathbf{x}_0) - \boldsymbol{\varphi}(t; \mathbf{x}_0) \tag{4.1}$$

Linearising the flow map with respect to the initial condition yields

$$\delta\mathbf{x}(t) = \boldsymbol{\Phi}(t, t_0)\, \delta\mathbf{x}_0 \tag{4.2}$$

where $\boldsymbol{\Phi}(t, t_0)$ is the STM. The STM satisfies the variational equations

$$\dot{\boldsymbol{\Phi}}(t, t_0) = D\mathbf{f}(\mathbf{x}(t))\, \boldsymbol{\Phi}(t, t_0), \qquad \boldsymbol{\Phi}(t_0, t_0) = \mathbf{I} \tag{4.3}$$

with $D\mathbf{f}$ denoting the Jacobian of the vector field evaluated along the reference trajectory. In practice, the STM is computed numerically by integrating the variational equations simultaneously with the EoMs and plays a fundamental role in the implementation of differential correction schemes. The evolution of small perturbations described by the STM is illustrated schematically in Fig. 4.2.

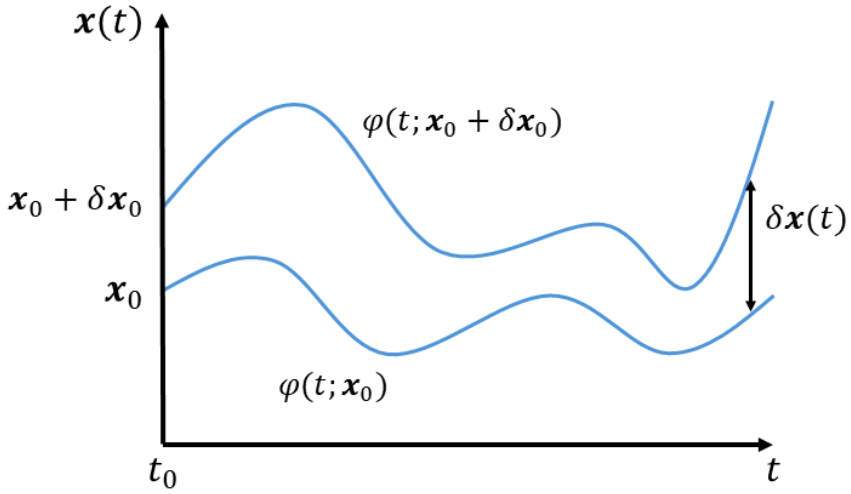

Figure 4.2: Reference and perturbed trajectories with the resulting displacement $\delta\mathbf{x}(t)$ [3].

Tab. 4.1 summarises the main definitions and relations introduced in this Section and used in the definition of the STM. The notation follows that of Koon et al. [3], where the explicit dependence on the initial time t_0 is omitted when not required for clarity.

Symbol	Description	Relation
$\boldsymbol{\varphi}(t, t_0)$	Flow map	$\boldsymbol{\varphi}(t, t_0) : \mathbf{x}(t_0) \mapsto \mathbf{x}(t)$
$\mathbf{f}(\boldsymbol{\varphi}(t; \mathbf{x}_0))$	RHS of the EoM	$\mathbf{f}(\boldsymbol{\varphi}(t; \mathbf{x}_0)) = \frac{d}{dt}\boldsymbol{\varphi}(t; \mathbf{x}_0)$
$\boldsymbol{\Phi}(t, t_0)$	STM	$\boldsymbol{\Phi}(t, t_0) = \frac{\partial}{\partial \mathbf{x}_0}\boldsymbol{\varphi}(t; \mathbf{x}_0)$
$D\mathbf{f}(\mathbf{x}(t))$	Jacobian of the vector field	$\delta\dot{\mathbf{x}} = D\mathbf{f}(\mathbf{x}(t))\,\delta\mathbf{x}$

Table 4.1: Notation and fundamental relations associated with the STM.

4.2.1. Differential correction

The differential correction scheme is introduced to compute the initial conditions of a periodic orbit. In order to enforce an orthogonal crossing of the xz-plane, the initial state is constrained to have the form

$$\mathbf{x}_0 = (x_0,\, 0,\, z_0,\, 0,\, v_{y0},\, 0)^T \tag{4.4}$$

This implies that the values of x_0, z_0, and v_{y0} must be determined such that, at the final time t_f, corresponding to the subsequent crossing of the xz-plane and therefore to half of the orbital period, the state again satisfies the symmetry conditions and can be written as

$$\mathbf{x}_f = (x_f,\, 0,\, z_f,\, 0,\, v_{yf},\, 0)^T. \tag{4.5}$$

The differential correction procedure allows to compute the correction to the initial conditions in order to drive the system toward periodicity. It starts from an initial guess providing both an initial state and a final time. If the guess on the final time is not available, the integration can be stopped at the subsequent xz-plane crossing during the first iteration by an *event function*. In this work, the initial guess is taken from the NASA JPL periodic orbit database[1] since the convergence of the method requires a sufficiently accurate initial guess. Starting from this initial state, the trajectory is propagated up to the final time t_f and the error vector is computed as the mismatch in the symmetry conditions at the final state as shown in Eq. (4.6)

$$\delta\mathbf{x_f} = \begin{bmatrix} 0 - y_f \\ 0 - v_{xf} \\ 0 - v_{zf} \end{bmatrix} \tag{4.6}$$

[1]NASA Jet Propulsion Laboratory (JPL), *Three-Body Periodic Orbits*, available at `https://ssd.jpl.nasa.gov/tools/periodic_orbits.html`, last accessed 17 October 2025.

a linear mapping is then employed to relate the deviations in the initial conditions to those observed at the final state. This relation is expressed through the following system:

$$\begin{bmatrix} \delta y_f \\ \delta v_{xf} \\ \delta v_{zf} \end{bmatrix} = \begin{bmatrix} \Phi_{21} & \Phi_{23} & \Phi_{25} & \left.\dfrac{\partial y_f}{\partial t}\right|_{\mathbf{x}_f} \\ \Phi_{41} & \Phi_{43} & \Phi_{45} & \left.\dfrac{\partial v_{xf}}{\partial t}\right|_{\mathbf{x}_f} \\ \Phi_{61} & \Phi_{63} & \Phi_{65} & \left.\dfrac{\partial v_{zf}}{\partial t}\right|_{\mathbf{x}_f} \end{bmatrix} \begin{bmatrix} \delta x_0 \\ \delta z_0 \\ \delta v_{y0} \\ \delta t_f \end{bmatrix} \tag{4.7}$$

each entry in the i-th row and j-th column of the matrix corresponds to the partial derivative of the i-th component of the final state correction with respect to the j-th component of the initial state correction.
The terms associated with the state variables are obtained from the STM, since it relates variations in the initial state to variations in the final state, according to $\delta\mathbf{x}_f = \mathbf{\Phi}\,\delta\mathbf{x}_0$. The remaining terms, instead, are directly related to the system dynamics. The time derivatives of the state are evaluated at the final time as shown in Eq. 4.8.

$$\begin{cases} \left.\dfrac{\partial y_f}{\partial t}\right|_{\mathbf{x}_f} = v_{yf} \\ \left.\dfrac{\partial v_{xf}}{\partial t}\right|_{\mathbf{x}_f} = \left.\dfrac{\partial U}{\partial x}\right|_{\mathbf{x}_f} + 2\,v_{yf} \\ \left.\dfrac{\partial v_{zf}}{\partial t}\right|_{\mathbf{x}_f} = \left.\dfrac{\partial U}{\partial z}\right|_{\mathbf{x}_f} \end{cases} \tag{4.8}$$

The correction to the initial state is obtained by solving the linear system Eq. (4.7) and updating the initial condition accordingly. The procedure is repeated iteratively until the residual falls below a prescribed tolerance.
The linear system in Eq. (4.7) is underdetermined, and therefore admits infinitely many solutions. In practice, a particular solution can be obtained directly, for instance by computing a minimum-norm correction. However, the presence of a free degree of freedom allows one component of the initial state to be prescribed, in order to control the characteristics of the resulting periodic orbit. In this work, the available degree of freedom is exploited by prescribing either the x or the z coordinate, depending on which choice is more convenient for the numerical continuation procedure described in the following Section.
To prescribe the x coordinate, the correction δx_0 is excluded from the vector of unknowns in Eq. (4.7). Consequently, the corresponding column of the matrix, the first one in this

case, is removed from the system. The resulting reduced system can be written as

$$\begin{bmatrix} \delta y_f \\ \delta v_{x,f} \\ \delta v_{z,f} \end{bmatrix} = \begin{bmatrix} \Phi_{23} & \Phi_{25} & \left.\frac{\partial y_f}{\partial t}\right|_{\mathbf{x}_f} \\ \Phi_{43} & \Phi_{45} & \left.\frac{\partial v_{x,f}}{\partial t}\right|_{\mathbf{x}_f} \\ \Phi_{63} & \Phi_{65} & \left.\frac{\partial v_{z,f}}{\partial t}\right|_{\mathbf{x}_f} \end{bmatrix} \begin{bmatrix} \delta z_0 \\ \delta v_{y0} \\ \delta t_f \end{bmatrix} \tag{4.9}$$

Similarly, when the z coordinate is defined a priori, the correction δz_0 is removed from the vector of unknowns, and the corresponding sensitivity terms are eliminated from Eq. (4.7), that is the second column of the matrix. The resulting reduced system becomes

$$\begin{bmatrix} \delta y_f \\ \delta v_{x,f} \\ \delta v_{z,f} \end{bmatrix} = \begin{bmatrix} \Phi_{21} & \Phi_{25} & \left.\frac{\partial y_f}{\partial t}\right|_{\mathbf{x}_f} \\ \Phi_{41} & \Phi_{45} & \left.\frac{\partial v_{x,f}}{\partial t}\right|_{\mathbf{x}_f} \\ \Phi_{61} & \Phi_{65} & \left.\frac{\partial v_{z,f}}{\partial t}\right|_{\mathbf{x}_f} \end{bmatrix} \begin{bmatrix} \delta x_0 \\ \delta v_{y0} \\ \delta t_f \end{bmatrix} \tag{4.10}$$

while the Eqs. (4.6) and (4.8) remain exactly the same.

4.2.2. Numerical continuation

The differential correction method described in the previous Section is employed to compute the initial condition of a single periodic orbit. The objective is now to extend this approach in order to generate the entire family of halo orbits. As discussed above, the differential correction scheme requires an accurate initial guess for convergence. For this reason, numerical continuation is adopted, in which successive periodic orbits are obtained by using a slightly modified converged solution as the initial guess for a nearby one.

In this work, numerical continuation is implemented starting from a halo orbit located approximately in the middle of the family, corresponding to a $JC = 3.09$. This choice does not follows any specific optimal criterion, but provides a convenient starting point. From this intermediate orbit, the family can be continued toward the Moon and toward the L_2 point by prescribing suitable coordinates that vary monotonically along the respective branches, without encountering bifurcations in the considered range. The initial guess is taken from the NASA JPL database and corresponds to the state at the apocentre of the orbit.

Starting from this reference orbit, the continuation is first carried out toward the orbit branch approaching the Moon. Due to the known structure of the Earth-Moon L_2 halo

orbit family, the variation of the x coordinate is dominant along this branch. Therefore, differential correction is performed by prescribing the x coordinate of the initial condition. Successive periodic solutions are then obtained by using the converged orbit as the initial guess for the next one, while progressively decreasing the prescribed value of x_0, so that each orbit is closer to the Moon than the previous one.
The continuation toward the opposite branch of the family, so toward the L_2 point, is carried out in an analogous manner. In this case, the variation along the family is more pronounced in the out-of-plane direction, and the z coordinate is therefore prescribed as a continuation parameter. The family is generated by using each corrected orbit as the initial guess for the subsequent one while progressively increasing the value of z_0.

4.3. Stability analysis and definition of Near Rectilinear Halo Orbits

NRHOs are identified as a region within the halo orbit family, characterised by favourable linear stability properties. In particular, they are generally defined as the subset of halo orbits that approach the Moon and are either linearly stable or only weakly unstable.
The stability of periodic orbits within the CR3BP is evaluated using the SI, whose definition is derived from the eigenvalues of the monodromy matrix $\mathbf{\Phi}(T)$, i.e. the STM evaluated over one period T of the periodic orbit.
The monodromy matrix $\mathbf{\Phi}(T)$ associated with a periodic orbit of the CR3BP has six eigenvalues, which can be conveniently grouped into three pairs. Due to the time-independent nature of the CR3BP, one pair of eigenvalues is always equal to unity and does not affect the orbital stability.
The remaining two eigenvalue pairs determine the linear stability characteristics of the orbit. Within the NRHOs regime, two configurations can be identified:

- **Linear stability:** both nontrivial eigenvalue pairs are complex conjugates and lie on the unit circle, i.e. (λ_i, λ_i^*) with $\|\lambda_i\| = 1$. In this case, small perturbations remain bounded and give rise to oscillatory motion about the periodic orbit.
- **Linear instability:** one nontrivial pair is complex conjugate with unit modulus, while the other pair consists of real reciprocal eigenvalues $(\lambda_i, 1/\lambda_i)$ with $\|\lambda_i\| > 1$. This configuration is characterised by the presence of stable and unstable directions along which perturbations decay or grow exponentially.

Additional stability configurations may arise when complex conjugate eigenvalues with modulus different from unity are present. These cases correspond to complex instability

and are typically associated with bifurcations [39].
Following this discussion on the relation between the monodromy matrix eigenvalues and linear stability, the SI can be introduced. For each pair of nontrivial eigenvalues a SI ν_i can be defined, as reported by Zimovan et al. [14]. In this work, only the index associated with the eigenvalue of maximum modulus is used, since it is sufficient to determine whether the orbit is linearly stable or unstable. Its expression is:

$$\nu_{\max} = \frac{1}{2}\left(\|\lambda_{\max}\| + \frac{1}{\|\lambda_{\max}\|}\right) \tag{4.11}$$

For linearly unstable orbits, the SI takes values greater than unity, since the eigenvalue with maximum modulus belongs to the real reciprocal pair and has modulus larger than one. Conversely, for linearly stable orbits, all nontrivial eigenvalue pairs lie on the unit circle, and the SI is therefore equal to unity.
The evolution of the SI along the halo family near the Moon is shown as a function of the perilune radius (r_p) in Fig. 4.3.

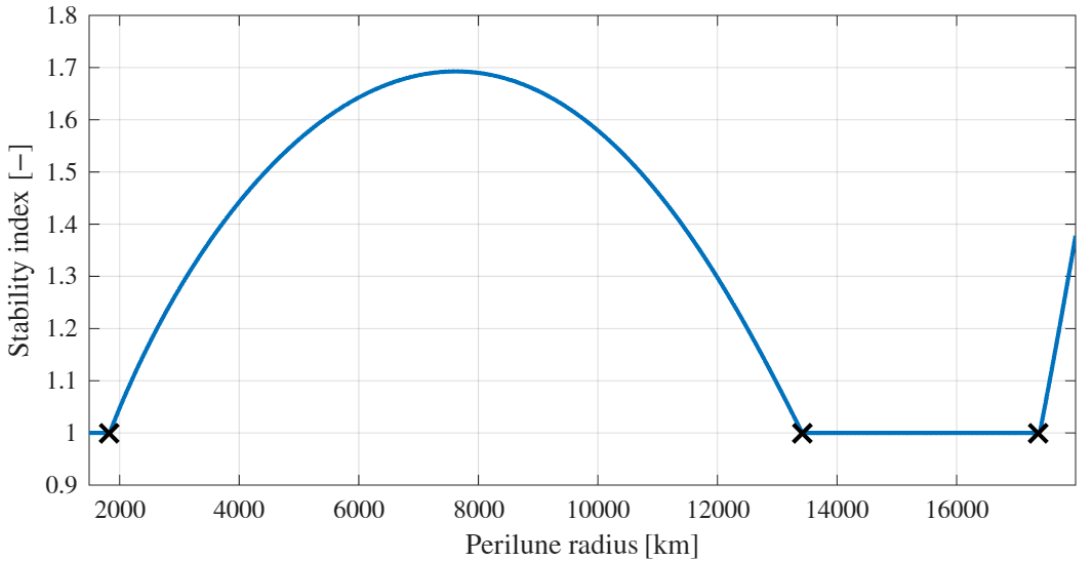

Figure 4.3: Stability index.

The black crosses highlight the points at which the SI changes its behaviour, i.e. stability changes. In the Earth-Moon system, the L_2 NRHOs can be defined as the portion of the halo orbit family associated with trajectories that approach the smaller primary and occur between the first and the third stability changes along the family [40]. In the Earth-Moon system, these bounds correspond to halo orbits with perilune radii of approximately 1832 km and 17390 km, respectively [14].

Beyond the third stability change, as the halo family is continued toward the L_2 point, the SI increases rapidly, indicating a significant growth of linear instability. Notably, the third stability change is also associated with an extremum in the orbital energy along the halo family [41]. Fig. 4.4 shows the trajectories of the NRHOs as a function of JC and r_p.

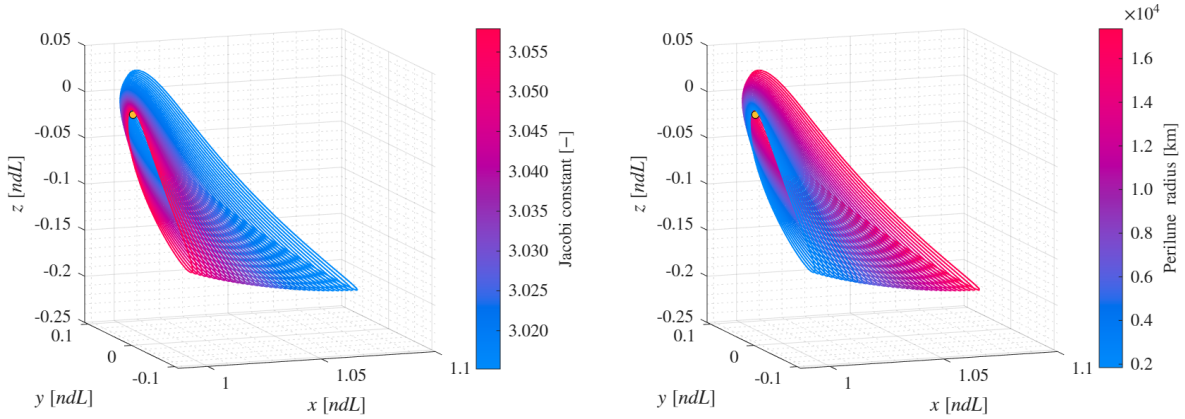

(a) NRHOs as a function of JC.

(b) NRHOs as a function of perilune radius.

Figure 4.4: Earth-Moon L2 NRHOs.

4.4. Selection of representative orbits

The candidates for the analyses presented in this Thesis are four representative orbits, selected according to their characteristics. The corresponding orbital parameters are summarized in Tab. 4.2, where r_p denotes the perilune radius and T the orbital period, while the associated trajectories are shown in Fig. 4.5.

JC [-]	SI [-]	r_p [km]	T [days]
3.0546	1.0962	2 184.1295	6.1427
3.0474	1.2971	3 106.9708	6.5193
3.0271	1.6908	7 932.0236	8.0206
3.0176	1.0944	12 996.7394	9.3312

Table 4.2: Parameters of the NRHOs considered for the analysis.

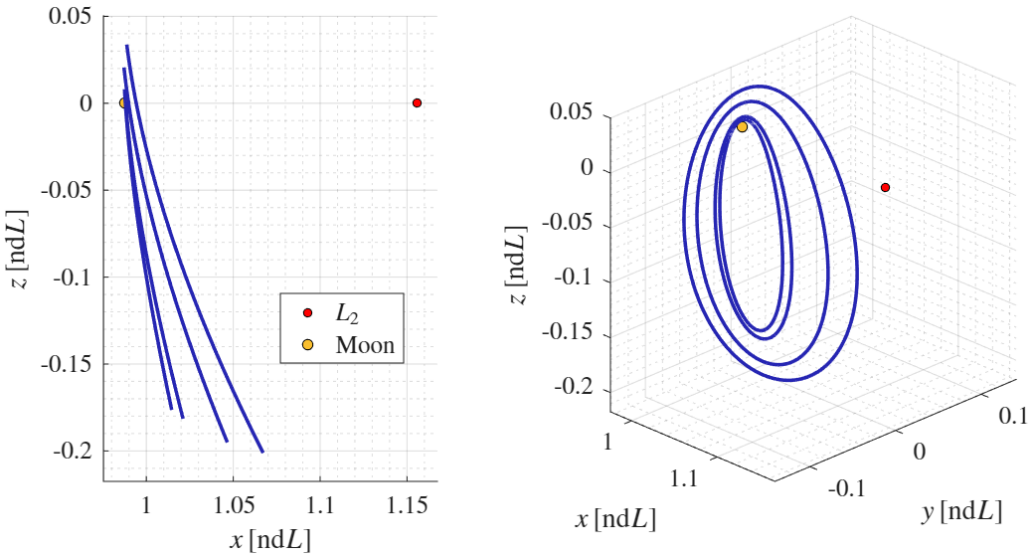

Figure 4.5: Trajectories of the NRHOs considered for the analysis.

The location of the selected orbits within the overall NRHO is illustrated in Fig. (4.6) in terms of the orbital parameters, with the corresponding values highlighted along the family trends.

The four orbits considered in the present analysis are selected in order to capture a range of stability and geometric characteristics within the NRHO subfamily. One of the selected orbits is characterised by a high stability index, close to the upper end of the range observed for NRHOs. This case is included to investigate the escape behaviour associated with relatively high linear instability within this family, and it is consistent with configurations previously analysed in the literature [36].

A second orbit, the one with $JC = 3.0474$ and $SI = 1.2971$, corresponds to the orbit selected for the Lunar Gateway mission. This orbit is included due to its operational relevance and its favorable dynamical properties, which make it a reference configuration for long-term cislunar missions.

The remaining two orbits are characterized by comparatively low and similar values of the SI, while exhibiting significantly different perilune radii. These orbits are located near opposite extremes of the NRHO subfamily and are selected to assess how the escape dynamics vary between geometrically distinct NRHOs that share similar linear stability properties.

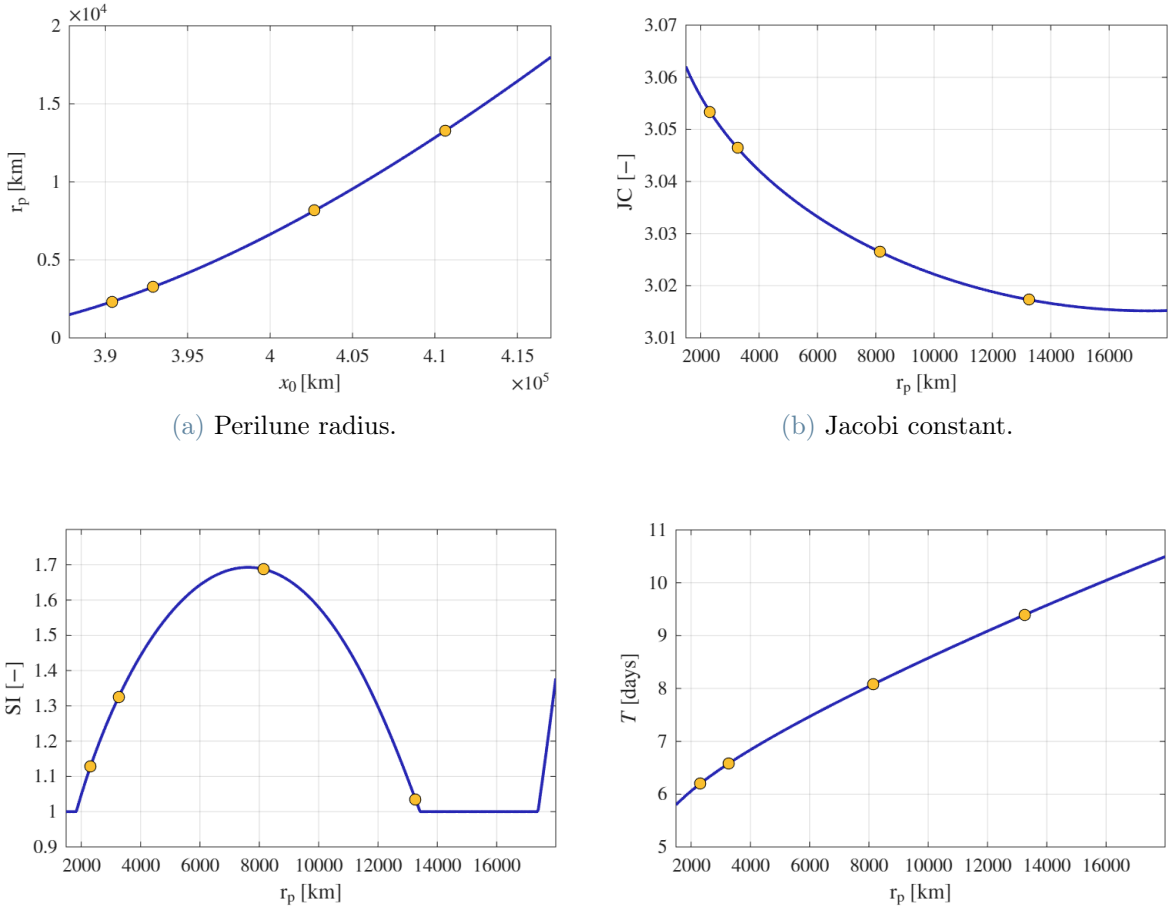

(a) Perilune radius.

(b) Jacobi constant.

(c) Stability index.

(d) Orbital period.

Figure 4.6: Parameters of the NRHOs considered for the analysis.

4.5. Invariant manifold construction

In this analysis, the dynamics of invariant manifolds is exploited to design escape trajectories from the cislunar region. The concept of invariant manifold was introduced in Sec. 3.7, here, the procedure adopted to compute these structures is described in detail.
Linearly unstable periodic orbits are characterised by the presence of stable and unstable directions, along which small perturbations decay or grow exponentially with time, respectively. These directions define the stable and unstable invariant manifolds associated with the orbit, as already introduced in the discussion of the SI in the previous Section [22, 42].
In practice, invariant manifolds are generated by applying small perturbations to a state along a periodic orbit, in the corresponding stable and unstable directions, which depend on the phase θ along the orbit. For linearly unstable periodic orbits, the monodromy matrix $\mathbf{\Phi}(T)$ admits a pair of real reciprocal eigenvalues λ_s and λ_u, with $\|\lambda_s\| < 1$ and

$\|\lambda_u\| > 1$, as discussed in the stability analysis. The corresponding eigenvectors define the local stable and unstable directions. In particular, perturbations applied along the unstable eigenvector $\mathbf{\Lambda}^u(\theta_0)$, associated with the eigenvalue of maximum modulus of $\mathbf{\Phi}(T)$, generate trajectories that asymptotically depart from the periodic orbit, thereby forming the unstable invariant manifold. The unstable direction at any phase angle along the periodic orbit can be obtained without recomputing the monodromy matrix at each point, but propagating the corresponding eigenvector along the orbit using the STM, as expressed in Eq. (4.12).

$$\mathbf{\Lambda}^u(\theta) = \mathbf{\Phi}(t_0, t)\, \mathbf{\Lambda}^u(\theta_0) \tag{4.12}$$

The directions are then normalised:

$$\hat{\mathbf{\Lambda}}^u(\theta) = \frac{\mathbf{\Lambda}^u(\theta)}{\|\mathbf{\Lambda}^u(\theta)\|} \tag{4.13}$$

A perturbation ε is then applied in this direction

$$\mathbf{x}_0^u(\theta) = \mathbf{x}_0(\theta) \pm \varepsilon\, \hat{\mathbf{\Lambda}}^u(\theta) \tag{4.14}$$

The perturbation magnitude ε must be sufficiently large to ensure that the trajectory departs from the periodic orbit along the unstable manifold, while remaining small enough for the linear approximation to be valid [42]. In the present analysis, a value of $\varepsilon = 10^{-4}$ is adopted.

4.5.1. Eigenvalues sign and manifold orientation

The sign of the perturbation parameter ε determines the orientation of the invariant manifold along a given unstable direction. However, its effect depends on the sign of the associated eigenvalue.

When the considered eigenvalue is positive, the two possible signs of ε select the two distinct branches of the invariant manifold, corresponding to opposite initial orientations along the unstable direction. One branch initially evolves toward the smaller primary, while the other departs from it. In this case, for a phase angle $\theta = 360°$, used here as an angular parametrisation of the orbital phase, the resulting behaviour is identical to that at $\theta = 0°$, as expected from the periodicity of the orbit. The situation changes when the maximum eigenvalue is negative, as occurs for NRHOs. In this case, the unstable direction undergoes an orientation reversal over one orbital period. As a consequence, the orientation of the unstable manifold at $\theta = 360°$ is opposite to that at $\theta = 0°$.

Due to this inversion, the two possible signs of the perturbation parameter ε no longer

uniquely identify the expected inward and outward branches. Instead, each perturbation sign generates a distinct manifold branch whose local evolution may be directed either toward or away from the smaller primary, depending on the phase along the orbit.
The observed inversion of the manifold orientation for negative eigenvalues can be explained by considering the eigenstructure of the monodromy matrix. Let $\mathbf{\Phi}(T)$ denote the monodromy matrix associated with the periodic orbit, and let $\mathbf{\Lambda}^u$ be the unstable eigenvector associated with the eigenvalue λ_u, such that the eigenvalue problem in Eq. (4.15) is satisfied:

$$\mathbf{\Phi}(T)\,\mathbf{\Lambda}^u = \lambda_u\,\mathbf{\Lambda}^u \tag{4.15}$$

As previously discussed, the unstable direction at a generic phase θ along the orbit is obtained by transporting the reference eigenvector through the STM, as shown in Eq. (4.12). After one full orbital period, corresponding to $\theta = 360°$, the STM used to map the manifold direction along the orbit coincides with the monodromy matrix $\mathbf{\Phi}(T)$, yielding

$$\mathbf{\Lambda}^u(T) = \mathbf{\Phi}(T)\,\mathbf{\Lambda}^u(\theta_0) \tag{4.16}$$

exploiting the eigenvalue relation in Eq. (4.15), Eq. (4.16) can be rewritten as

$$\mathbf{\Lambda}^u(T) = \lambda_u\,\mathbf{\Lambda}^u(\theta_0) \tag{4.17}$$

When the unstable eigenvalue λ_u is negative, this operation introduces a sign inversion in the resulting direction. As a consequence, the unstable direction at $\theta = 360°$ is opposite to that at $\theta = 0°$. This behaviour directly results from the negative real eigenvalue of the monodromy matrix and governs the phase-dependent orientation of the invariant manifold. It is worth noting that eigenvectors are defined up to a sign. As a consequence, when they are computed numerically, in this case using MATLAB®, the returned eigenvector may have either orientation. Both choices are equally valid, as they satisfy the eigenvalue relation in Eq. (4.15), and therefore do not affect the correctness of the analysis, also considering that both unstable directions are included. The distinction between positive and negative perturbations is thus purely conventional and depends on the orientation of the eigenvector returned by MATLAB®. Exchanging the two signs would not alter the physical interpretation of the results.
Figure 4.7 shows the unstable manifold directions for the orbit selected for the present analysis with $JC = 3.0271$ and $SI = 1.6908$. The corresponding results for the other selected orbits are reported in Appendix A.

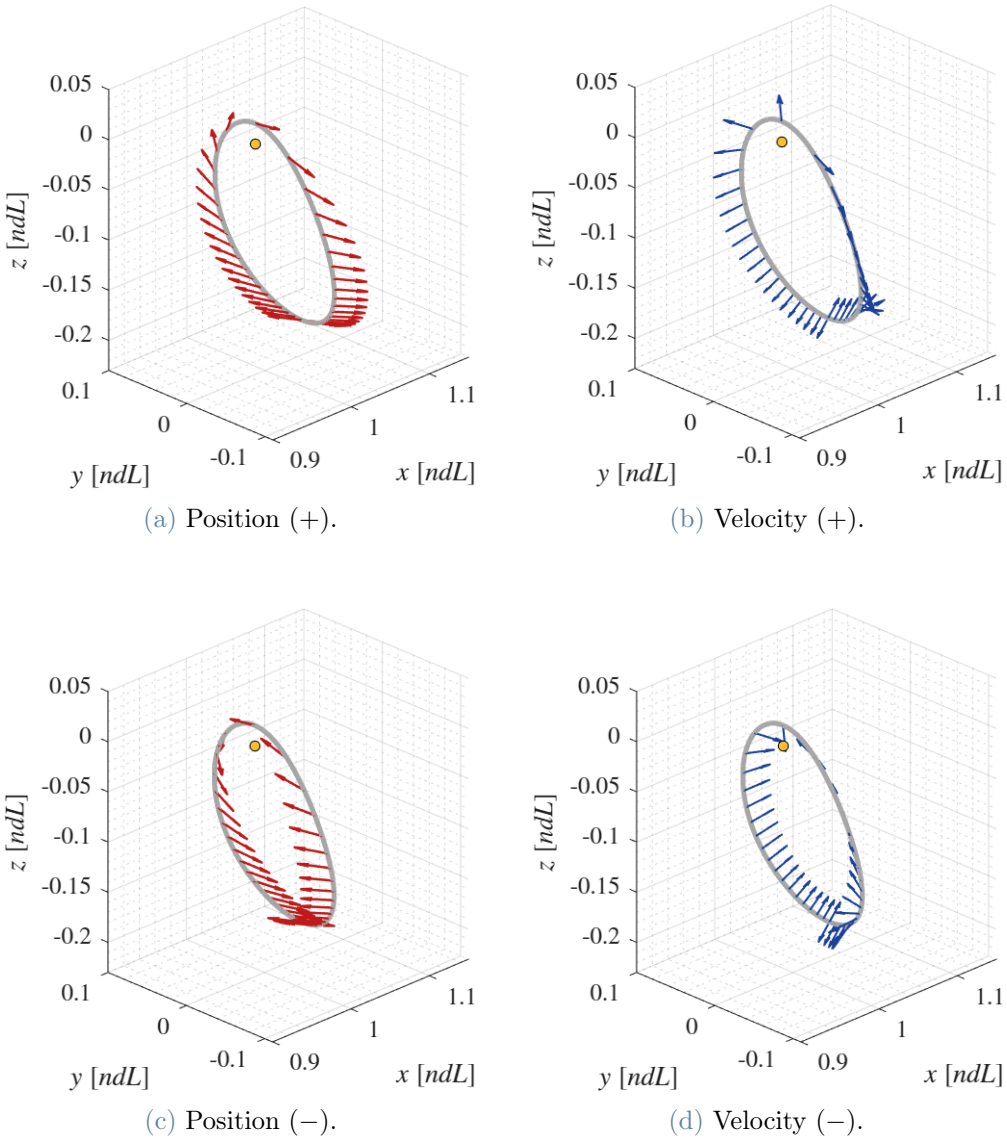

(a) Position (+). (b) Velocity (+).

(c) Position (−). (d) Velocity (−).

Figure 4.7: Positive and negative state perturbations.

4.6. Escape analysis

This Section presents the methodology adopted to investigate escape trajectories from the selected NRHOs. The analysis is performed within the dynamical framework introduced in the previous Chapters, considering trajectories generated through the unstable manifolds in the coupled CR3BP model.

The main objective is to understand how the relative configuration of the Earth, Moon, and Sun affects the success of the escape. To account for this effect, the parameter α introduced in Sec. 3.8 is considered, recalling that it represents the relative angle between

the Sun-Earth and the Earth-Moon reference frames (see Fig. 3.6). In particular, the study focuses on the phasing between the Earth-Moon system and the Sun at the departure epoch, indicated with α_0, and at the time of the spacecraft's first crossing into the Sun's sphere of influence, indicated with α_{cross}.
In addition to the geometrical analysis, further investigations are carried out on the system energy and its chaotic behaviour. These aspects are examined to better understand how energy variations and dynamical sensitivity influence the escape outcome.

4.6.1. Classification of possible outcomes and escape criteria

A parametric analysis is carried out by varying the values of α_0 and the phase angle θ. For each selected combination of these parameters, the corresponding manifold trajectory is generated and propagated.
The analysis is performed according to the following discretisation and propagation settings:

- **Discretisation:** the angles α_0 and θ are discretised with a resolution of 1°
- **Propagation time:** each trajectory is propagated for a maximum duration of 10 months.

The relatively long propagation time, although larger than the typical dynamical timescales of the cislunar environment [36], is adopted to capture a wide range of possible dynamical behaviours and to ensure that late escape events are not overlooked.
The propagated manifold trajectories exhibit different dynamical behaviours depending on the initial configuration. Based on their long-term evolution within the coupled CR3BP framework, five distinct outcomes are identified and classified as follows:

- **Escape through L_1:** the trajectory escapes the cislunar region through the L_1 gateway of the Sun-Earth system.
- **Escape through L_2:** the trajectory escapes the cislunar region through the L_2 gateway of the Sun-Earth system.
- **No escape:** the trajectory does not escape the Earth vicinity within the considered propagation time.
- **Earth impact:** the trajectory impacts the Earth within the considered propagation time.
- **Moon impact:** the trajectory impacts the Moon within the considered propagation time.

After introducing the possible dynamical outcomes, it is necessary to clarify how each of them is identified. The classification relies on specific criteria used to identify escape through L_1 and L_2, as well as impact events, within the considered time span.
In order to classify the trajectory as an escape through L_1 or L_2, both geometrical and energetic conditions must be satisfied. From the geometrical point of view, the x-coordinate of the trajectory must cross the corresponding Lagrange point location. In particular, an escape through L_1 is identified when

$$x < x_{L_1} \tag{4.18}$$

whereas an escape through L_2 requires

$$x > x_{L_2}. \tag{4.19}$$

The geometrical condition alone is not sufficient. In a complete disposal design, the ZVCs should be closed around the involved Lagrange point. Although this step is not explicitly addressed in the present work, an energetic consistency condition is introduced to ensure that the trajectory lies in a dynamically accessible region beyond the closed ZVC associated with the corresponding Lagrange point [42]
The energetic condition is then satisfied when

$$V^2 - \Delta JC > 0 \tag{4.20}$$

where V^2 is the squared velocity magnitude and ΔJC is the difference between the JC of the considered Lagrange point and that of the trajectory in the Sun-Earth system, defined as $\Delta JC = JC_{L_{1,2}} - JC$.
Earth and Moon impacts instead, are detected during the propagation through dedicated event functions. At each integration step, the distance of the spacecraft from the centre of the Earth and of the Moon is evaluated as

$$d_E = \|\mathbf{x} - \mathbf{x}_E\|, \qquad d_M = \|\mathbf{x} - \mathbf{x}_M\| \tag{4.21}$$

therefore the corresponding distances from the surface are then defined as

$$s_E = d_E - r_E, \qquad s_M = d_M - r_M \tag{4.22}$$

where r_E and r_M are the normalised radii of the Earth and the Moon in the Earth-Moon system. When $s_E = 0$ or $s_M = 0$, the integration is stopped and an impact with the

Earth or the Moon is detected, respectively. With the classification criteria defined, the parametric analysis is now introduced.

4.6.2. Analysis on different initial configurations

The first analysis investigates the influence of the initial geometrical configuration on the escape dynamics. For each value of α_0, manifold trajectories are generated by applying a small perturbation along the unstable manifold direction. Both positive and negative perturbations are considered, leading to two distinct cases that are analysed separately. The objective of this analysis is to construct a map that report the outcome of the analysis for each value θ and α_0. This allows the identification of favourable or characteristic configurations that could serve as a preliminary basis for a complete operational design. The overall procedure adopted to construct the escape map is summarised in Algorithm 4.1.

Algorithm 4.1 Construction of the escape map as a function of α_0 and θ

for each α_0 **do**
  for each θ **do**
    Set the perturbed initial condition $\mathbf{x}_0(\theta) \pm \varepsilon \hat{\mathbf{\Lambda}}^u(\theta)$ and propagate for 10 months
    Compute V and JC
    Evaluate geometrical condition at final time:
      $x < x_{L_1}$ or $x > x_{L_2}$
    Evaluate energetic condition:
      $V^2 - \Delta JC > 0$
    if geometrical and energetic conditions for L_1 escape are satisfied **then**
      Classify as Escape through L_1
    else if geometrical and energetic conditions for L_2 escape are satisfied **then**
      Classify as Escape through L_2
    else if Earth impact detected **then**
      Classify as Earth impact
    else if Moon impact detected **then**
      Classify as Moon impact
    else
      Classify as No escape
    end if
    Store outcome in the escape map
  end for
end for

4.6.3. Analysis of the configuration at first entrance into the Sun's sphere of influence

A second analysis is now introduced, its logical structure is identical to that adopted in the previous Section. The main difference lies in the definition of the parameter α used for the mapping.

In the previous analysis, the escape map is constructed as a function of θ and α_0 while in the present one, the considered parameters are θ and α_{cross}.

The motivation for this second analysis is to create a direct relation with the Sun's position. The Sun plays a dominant role in the long-term evolution of escape trajectories. Its effective influence depends on the relative position of the spacecraft with respect to the Earth-Moon system, but when the spacecraft remains in the immediate vicinity of the Moon, the local dynamics is still governed by the Earth-Moon interaction. For this reason, the Sun's role becomes dominant after the first entrance into the its sphere of influence, that is adopted as a reference condition.

From an algorithmic point of view, the procedure remains the same as in the previous Section. However, an additional step is required. Since the propagation function takes α_0 as an input parameter, it is necessary to determine, for each value of θ, the corresponding α_0 that yields the desired value of α_{cross}. The procedure adopted to compute this relationship is described in the following.

The first entrance into the Sun's sphere of influence corresponds to the first crossing of the region of prevalence, as discussed in Sec. 3.8.

To determine α_0, it is necessary to recall that the region of prevalence depends on α, as shown in Fig. 3.9, and that α evolves in time according to Eq. (3.40) in the Earth-Moon and Eq. (3.41) in the Sun-Earth nondimensionalisation, respectively.

The relation between α_0 and α_{cross} at the first crossing from the Earth-Moon to the Sun-Earth system is given by

$$\alpha_{\text{cross}} = \alpha_0 + \frac{\omega_{EM} - \omega_{SE}}{\omega_{EM}} t_{\text{EM,cross}}, \tag{4.23}$$

where $t_{\text{EM,cross}}$ denotes the time of the first crossing in the Earth-Moon non-dimensional Time (ndT) units, directly provided by the propagation function.

To obtain the desired α_{cross}, a dedicated propagation function is employed in which only the Earth-Moon dynamics is integrated. The selected value of α_{cross} is imposed as input, thereby fixing the region of prevalence at the prescribed configuration. The trajectory is then propagated until the crossing occurs, and the corresponding $t_{\text{EM,cross}}$ is recorded.

By inverting Eq. (4.23), the associated value of α_0 is obtained as

$$\alpha_0 = \alpha_{\text{cross}} - \frac{\omega_{EM} - \omega_{SE}}{\omega_{EM}} t_{\text{EM,cross}}. \tag{4.24}$$

This procedure is consistent with the adopted framework, as α does not enter the equations of motion within a single frame but only determines the transition condition between frames. The Earth-Moon dynamics is therefore not altered.
The computation is repeated for each θ and α_{cross}, and the corresponding values of α_0 are collected in a matrix, which is then used as input for the algorithm described in the previous Section.

4.7. Finite Time Lyapunov Exponent

Following the escape analysis methodology described in the previous Section, the Finite-Time Lyapunov Exponent (FTLE) is introduced to provide additional insight into the local dynamical behaviour of the trajectories.
The FTLE is a quantity that measures how fast two initially close trajectories separate over a given time [43, 44]. In practice, it quantifies the rate of stretching of an infinitesimal perturbation applied to a reference trajectory during a finite time $T_{ref} = t - t_0$.
From a physical point of view, the FTLE provides an indication of local sensitivity to initial conditions, if it assumes large positive values, small perturbations grow rapidly and the motion is locally unstable. On the contrary, small or negative values indicate weak stretching or contraction, corresponding to locally more regular behaviour. For this reason, the FTLE is often used to identify dynamically significant regions of the phase space characterised by strong deformation of nearby trajectories.
The FTLE, here denoted with $\sigma_{T_{ref}}$, is computed from the Cauchy-Green deformation tensor, defined as $\mathbf{C} = \mathbf{\Phi}^{\mathrm{T}}\mathbf{\Phi}$, where $\mathbf{\Phi}$ is the STM evaluated at the time t. It can be written as

$$\sigma_{T_{ref}} = \frac{1}{|T_{ref}|} \ln \lambda_{\max}\left(\sqrt{\mathbf{C}}\right), \tag{4.25}$$

Where $\lambda_{\max}(\cdot)$ indicates the maximum eigenvalue. In this analysis T_{ref} is equal to 1 day.

5 | Results

The results obtained from the analysis detailed in Sec. 4.6 are presented and discussed in the following. The described methodology is applied to the four selected orbits, whose parameters are summarised in Tab. 4.2. The objective of this analysis is to investigate the dynamical evolution of the invariant manifolds associated with each orbit and to identify the resulting escape mechanisms. Particular attention is given to how the Earth-Moon-Sun configuration affects the resulting escape structures.
For each orbit, the corresponding escape maps are presented, which provide a global view of the escape regions and their geometry. Selected trajectories are then examined to characterise the different dynamical behaviours and to support the interpretation of the observed patterns.
After discussing the four cases individually, a broader analysis is carried out, focusing on the role of energy and on the emergence of chaotic behaviour in shaping the overall escape dynamics.

5.1. Escape maps and trajectories

5.1.1. Orbit with JC = 3.0271 and SI = 1.6908

The orbit corresponding to these parameters is selected as the reference case, as it is associated with the highest value of SI. This condition facilitates the departure of trajectories from the orbit, leading to a wider variety of dynamical behaviours. Fig. 5.1 shows the corresponding escape maps , where the analysis final outcomes are shown as function of α_0, the relative phase between the Earth-Moon and Sun-Earth systems at departure, and θ, the NRHO departure point phase angle.
First, it is important to note that, as will also be observed for the other NRHOs, the results at $\theta = 0°$ and $\theta = 360°$ do not coincide, even though these two values of the phase angle correspond to the same geometrical configuration. This behaviour is fully consistent with what is explained in Sec. 4.5.1 regarding the reversal of the manifold orientation after one orbital period, caused by the negative sign of the monodromy matrix eigenvalue

of the NRHOs. Indeed, the outcomes at $\theta = 0°$ in Fig. 5.1a perfectly match those at $\theta = 360°$ in Fig. 5.1b, and vice versa.

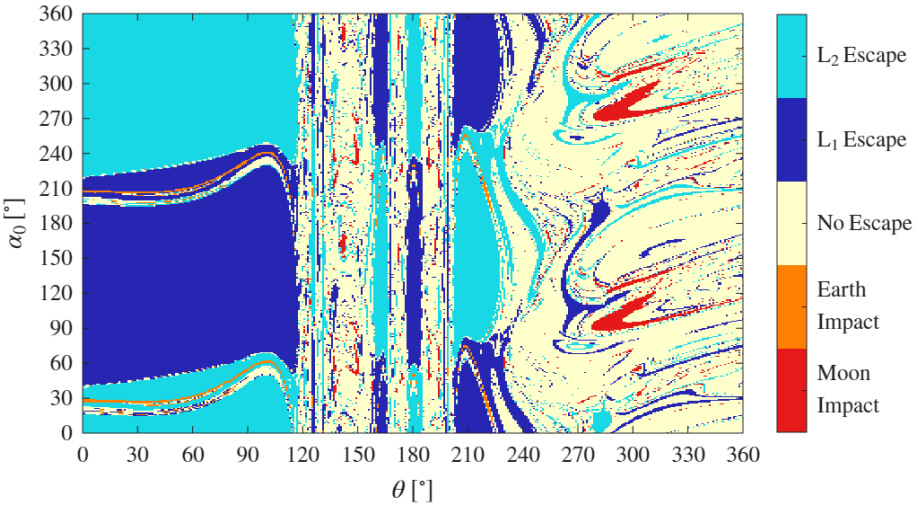

(a) Positive manifold perturbation.

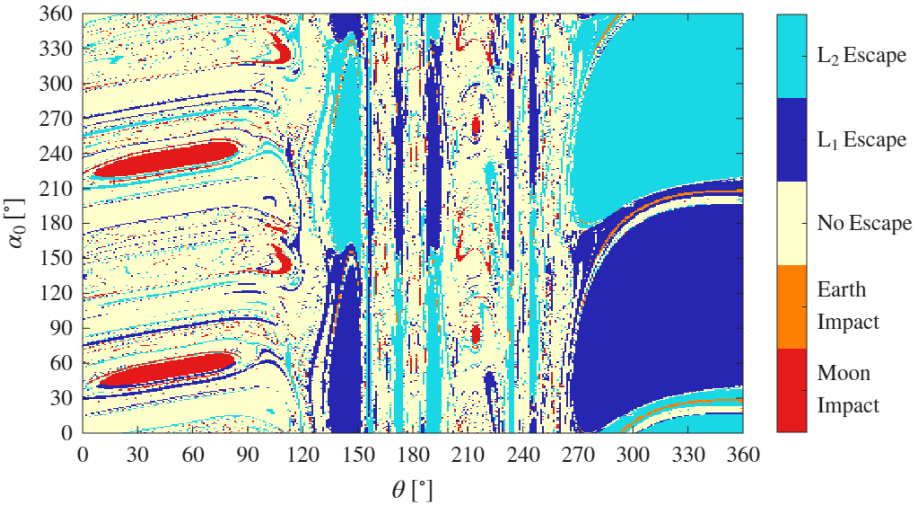

(b) Negative manifold perturbation.

Figure 5.1: Escape maps as a funtion of α_0 for the orbit with $JC = 3.0271$ and $SI = 1.6908$.

The maps clearly highlight the presence of distinct dynamical regions. From an operational perspective, particular attention is devoted to the domains in which escape occurs consistently. For the positive manifold perturbation, relatively wide and uniform escape regions are observed approximately in the interval $0° \lesssim \theta \lesssim 110°$, whereas for the negative perturbation they appear roughly in the range $270° \lesssim \theta \lesssim 360°$. In these intervals, small variations in the parameters α_0 and θ do not significantly alter the final escape outcome,

indicating a higher degree of robustness within the considered parameters.
In contrast, the central range of θ, coincident with the NRHO perilune, is characterised by a highly fragmented structure, indicative of enhanced chaotic dynamics. This behaviour is consistent with the stronger gravitational influence of the Moon in this phase of the orbit, where higher values of the FTLE have been observed [45]. Near perilune, the stable and unstable eigenvectors become less separated [31]. This reduced separation makes the corresponding invariant manifolds less distinct and increases the local sensitivity to perturbations.
Additional remarkable features include the Earth-impact stripes, which appear as thin structured regions embedded within the escape domains, and the Moon-impact islands. A more detailed interpretation of these behaviours is provided in the subsequent analysis.
With respect to the parameter α_0, a symmetry between the upper and lower portions of the maps can be observed. α_0 alone does not determine whether the escape occurs through L_1 or L_2. For a fixed value of α_0, both gateways may be accessed depending on θ. To further deepen the analysis, the parameter α_{cross} is now introduced in order to account for the relative configuration between the Earth-Moon and Sun-Earth systems at the first crossing of the Sun's sphere of influence. Fig. 5.2 shows the relationship between α_0 and α_{cross} as a function of θ.

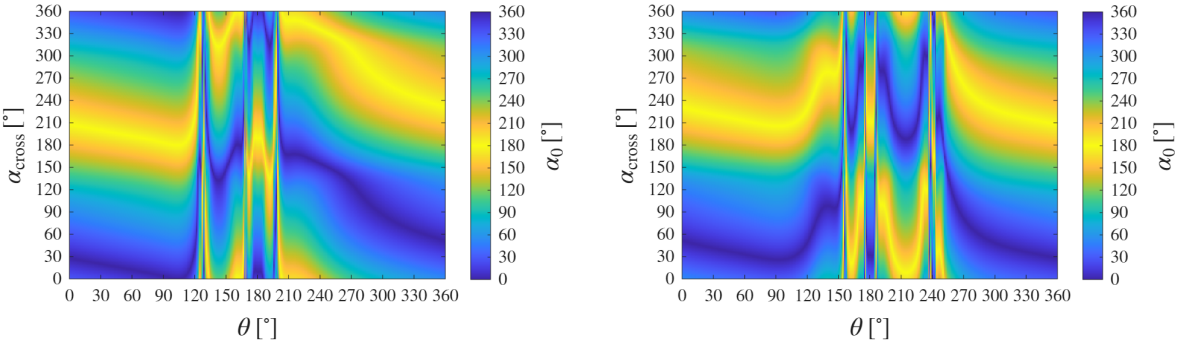

(a) Positive manifold perturbation.

(b) Negative manifold perturbation.

Figure 5.2: Relation between α_0 and α_{cross} for the orbit with $JC = 3.0271$ and $SI = 1.6908$.

The relationship between α_0 and α_{cross} as a function of θ reveals a consistent variation between the two angular parameters. The same interval of θ previously identified as dynamically complex exhibits a more irregular behaviour in the α_0-α_{cross} relation. In this region, the mapping between the two angles becomes less smooth, reflecting the increased dynamical sensitivity already observed in the corresponding escape maps, which is also associated with a greater variability in the timing of the first crossing.

Based on this alternative parametrisation, the escape maps are now reformulated in terms of α_{cross}. The corresponding results are shown in Fig. 5.3.

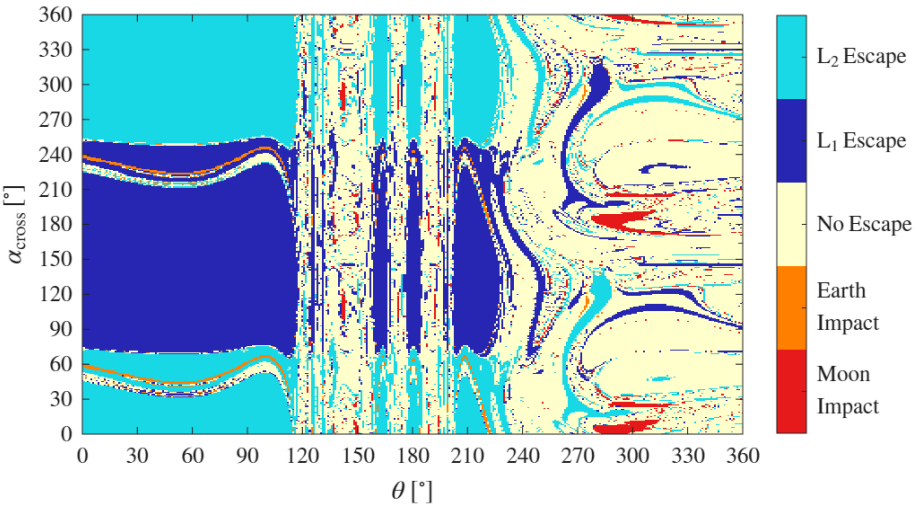

(a) Positive manifold perturbation.

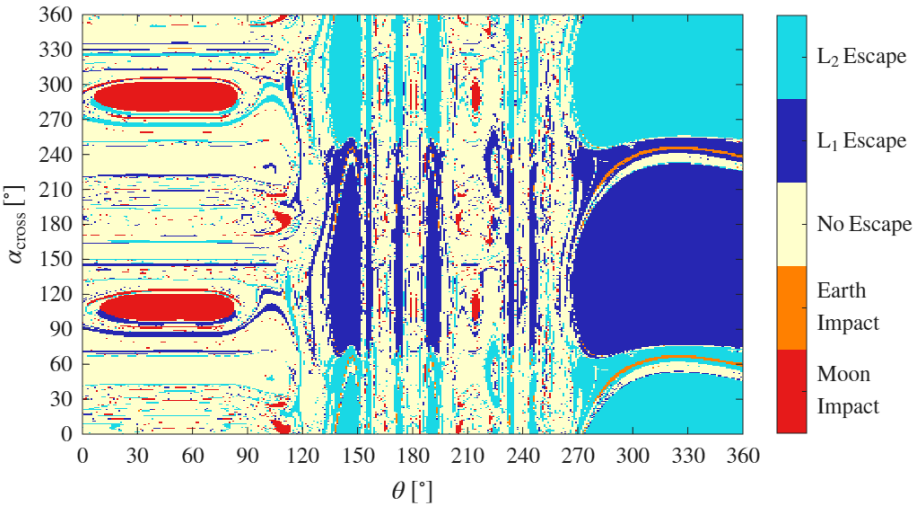

(b) Negative manifold perturbation.

Figure 5.3: Escape maps as a funtion of α_{cross} for the orbit with $JC = 3.0271$ and $SI = 1.6908$.

The escape maps as a function of α_{cross} exhibit a global structure that remains consistent with the one previously observed as a function of α_0. The main dynamical regions, including the wide escape domains and the central fragmented zone, are preserved, indicating that the overall escape behaviour is not radically altered by the change of parametrisation. However, when the escape occurs, the distinction between trajectories escaping through L_1 and L_2 appears more directly organised in this case. In this representation, the selection of the escape pathway can be more clearly associated with the relative configuration

of the primaries at the first crossing of the Sun's sphere of influence, confirming that the final outcome is strongly influenced by geometrical factors.
A three-dimensional representation of the relationship between θ, α_0, and α_{cross} is reported in Appendix B for completeness.
To better understand the dynamics in these regions, selected trajectories are shown in the following. In particular, all trajectories leading to Earth and Moon impacts are plotted together in the Sun-Earth system in Figs. 5.4 and 5.5, in order to highlight their overall behaviour.

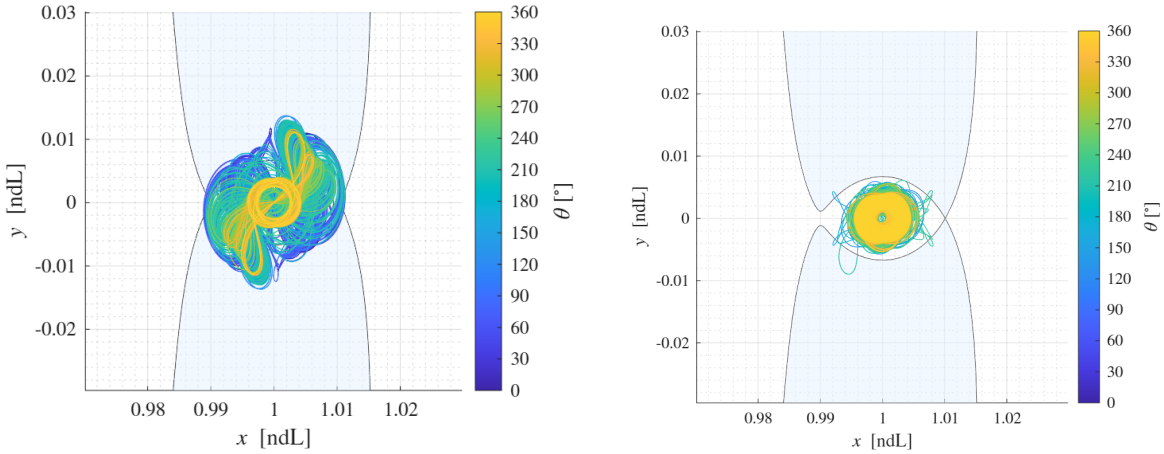

(a) Earth Impacts. (b) Moon Impacts.

Figure 5.4: Impact trajectories for the positive perturbed manifold of the orbit with $JC = 3.0271$ and $SI = 1.6908$.

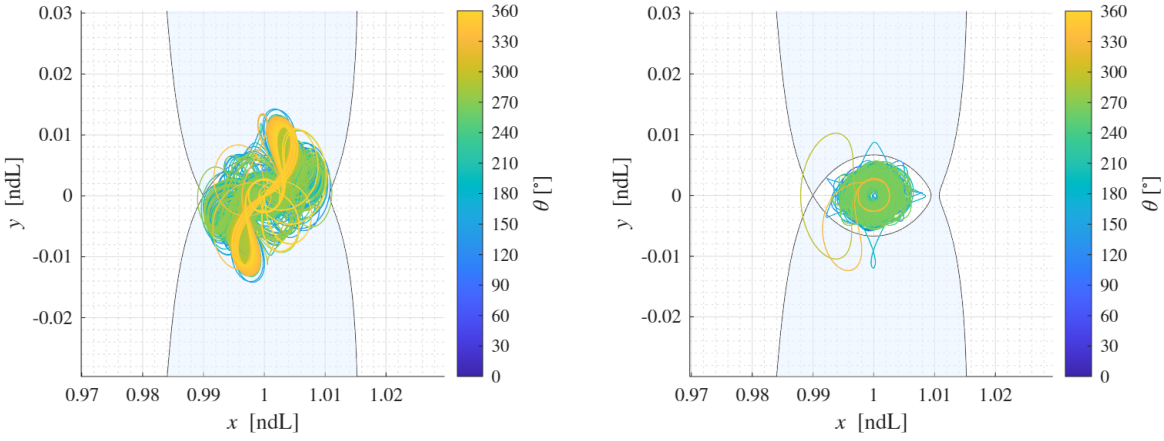

(a) Earth Impacts. (b) Moon Impacts.

Figure 5.5: Impact trajectories for the negative perturbed manifold of the orbit with $JC = 3.0271$ and $SI = 1.6908$.

Fig. 5.4a and 5.5a show all trajectories leading to an Earth impact. Several distinct behaviours can be identified, therefore to better characterise these patterns, subsets of trajectories are analysed separately below. With regard to the Moon impacts, shown in Figs. 5.4b and 5.5b, no clearly structured behaviour can be identified. Nevertheless, also for this case a representative selection of these trajectories is analysed in the following.
Fig. 5.6 highlights the regions of the escape map considered for the detailed trajectory analysis. In particular, the Earth-impact stripes and the Moon-impact island are indicated by the red boxes, the escape regions by the green boxes, and the area enclosed by the black square is also examined. Although this latter region is predominantly characterised by non-escaping trajectories, a limited number of escapes are present, making it relevant to investigate the associated dynamical behaviour.

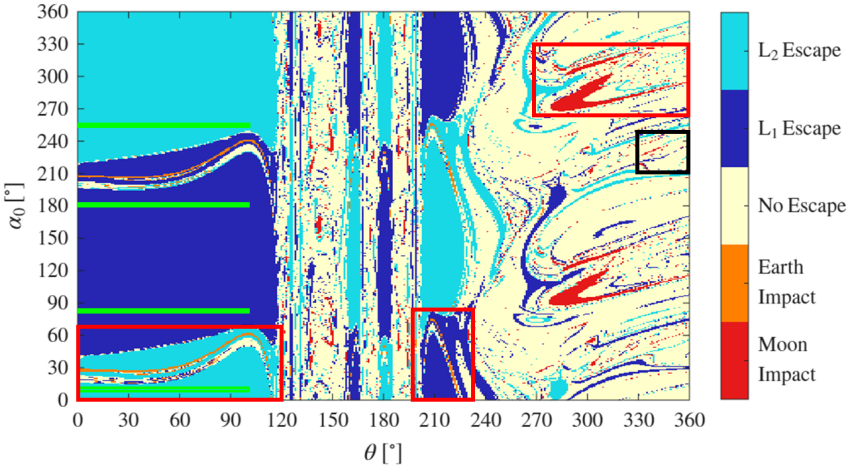

Figure 5.6: Regions of the escape map considered for the detailed trajectory analysis.

Fig. 5.7 the selected regions associated with Earth impacts. In particular, Fig. 5.7a illustrates the trajectories corresponding to the interval $0° \leq \theta \leq 120°$ and $0° \leq \alpha_0 \leq 75°$, while Fig. 5.7b presents those within the ranges $190° \leq \theta \leq 230°$ and $0° \leq \alpha_0 \leq 85°$. Several of these trajectories resemble a reverse Weak Stability Boundary (WSB) transfer, in which the unstable manifold associated with the considered NRHO is captured by a stable manifold leading towards the Earth, resulting in an impact. However, the two selected regions cannot be associated with a single defined dynamical behaviour.
Similar trajectories are reported in [29], where it is observed that the apogee typically lies within the first or third quadrants (illustrated in Fig. 2.1). In these configurations, the solar perturbation contributes to lowering the perigee, thereby favouring Earth impact. This mechanism is consistent with the majority of the trajectories analysed in the present work. Nevertheless, some trajectories exhibit more peculiar behaviours. In order to better characterise them, the evolution of the Earth distance is also presented in Fig. 5.8.

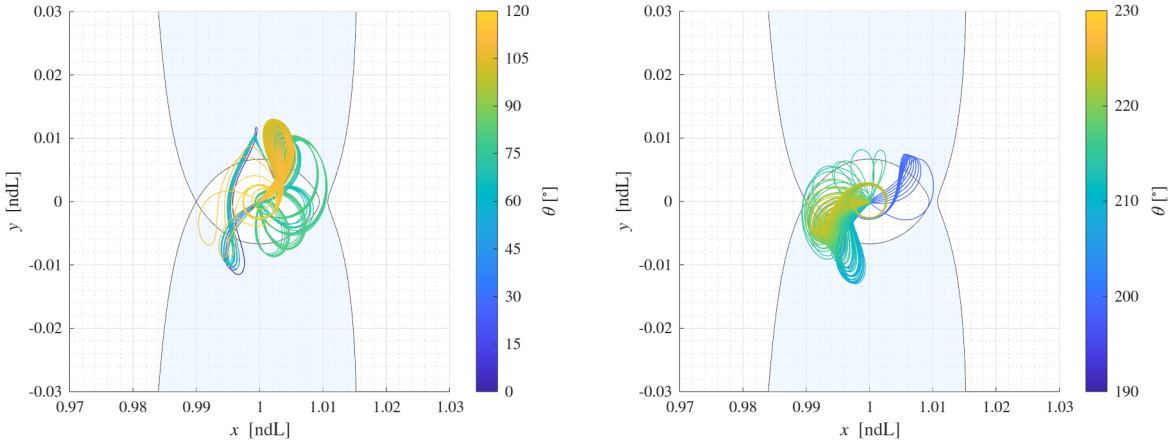

(a) Earth impacts within the interval $0° \leq \theta \leq 120°$ and $0° \leq \alpha_0 \leq 75°$.

(b) Earth impacts within the interval $190° \leq \theta \leq 230°$ and $0° \leq \alpha_0 \leq 85°$.

Figure 5.7: Earth impact trajectories for the positive perturbed manifold of the orbit with $JC = 3.0271$ and $SI = 1.6908$.

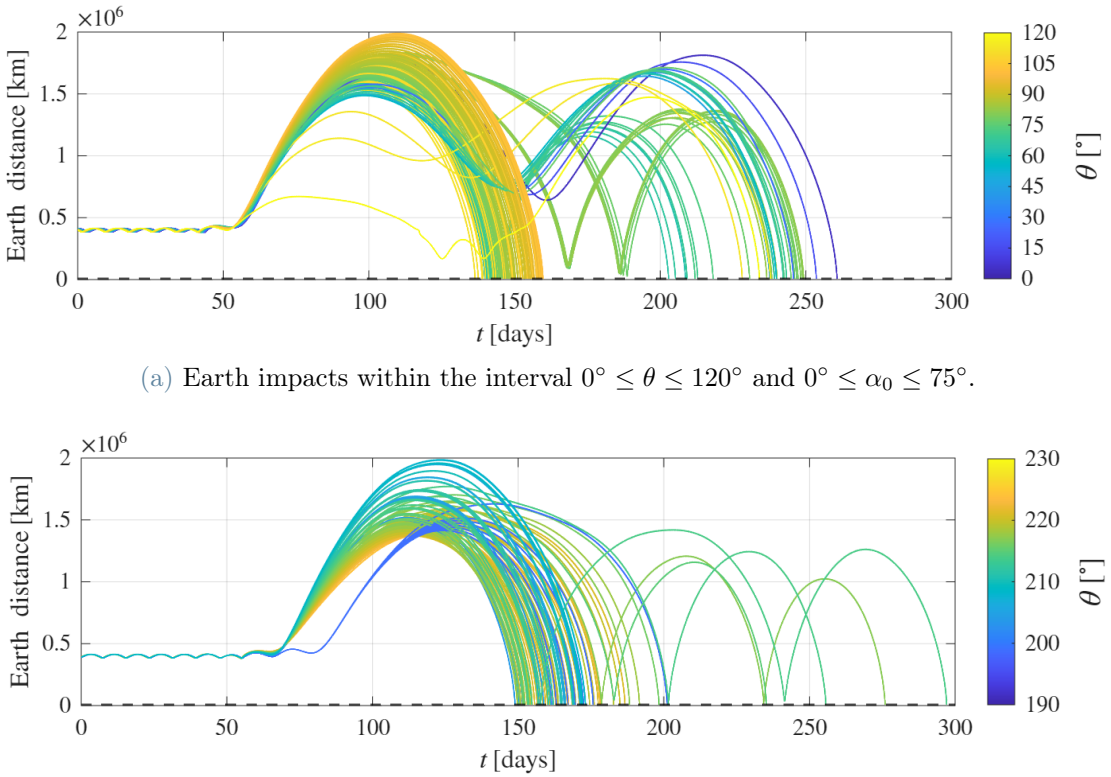

(a) Earth impacts within the interval $0° \leq \theta \leq 120°$ and $0° \leq \alpha_0 \leq 75°$.

(b) Earth impacts within the interval $190° \leq \theta \leq 230°$ and $0° \leq \alpha_0 \leq 85°$.

Figure 5.8: Distance from the Earth of the trajectories for the positive perturbed manifold of the orbit with $JC = 3.0271$ and $SI = 1.6908$.

From these plots, it is possible to clearly identify when the departure from the orbit occurs (the concepts of departure and escape, introduced by Boudad and Davis, are discussed in Sec. 2.3.3), as well as when the trajectory moves away from the Earth and subsequently approaches it again. By observing Figs. 5.7a and 5.8a, an interesting behaviour can be observed for trajectories with θ close to 70°. Although this feature is not clearly distinguishable from the trajectory plot alone, the Earth-distance evolution reveals that the spacecraft moves away from the Earth and approaches it again twice before impact. For this reason, one of these trajectories is isolated and shown separately in Fig. 5.9. This trajectory corresponds to $\alpha_0 = 28°$ and $\theta = 72°$. The beginning of the propagation is indicated by a black dot. The path followed by the spacecraft can be clearly distinguished: after departure, the trajectory undergoes a WSB-like evolution. However, instead of directly impacting the Earth, it performs a fly-by on the Earth, followed by a further apogee in the Earth-Moon region. Subsequently, the spacecraft encounters the Earth again and ultimately impacts it. This recurrent behaviour makes the trajectory particularly interesting for further analysis.

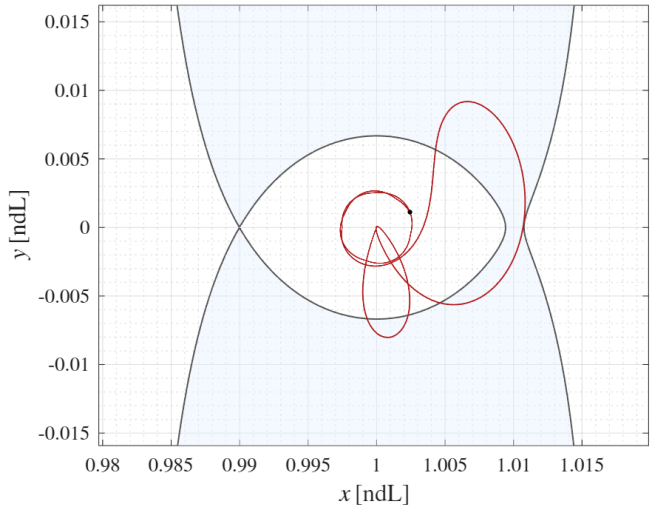

Figure 5.9: Earth impact trajectory at $\alpha_0 = 28°$ and $\theta = 72°$.

The trajectories resulting in a Moon impact within the interval $270° \leq \theta \leq 360°$ and $260° \leq \alpha_0 \leq 330°$ are illustrated instead in Fig. 5.10, while the corresponding evolution of the distance from the Moon is reported in Fig. 5.11.
From the trajectories representation, limited information can be extracted regarding the detailed dynamical evolution. However, it can be observed that several trajectories approach the central region of the Earth-Moon system before impacting the Moon. This suggests that some trajectories re-enter the Earth-Moon ZVC region prior to the final im-

pact. Additional insight can be obtained from the evolution of the Moon distance shown in Fig. 5.11. The majority of the trajectories exhibit a sequence of departures and re-approaches with respect to the Moon, characterised by successive increases and decreases in the lunar distance. In some cases, the final portion of the distance evolution resembles the initial phase observed before departure, indicating that the spacecraft temporarily returns to a Moon-centred orbital motion before impacting the surface. This recurring behaviour, represents an interesting feature that may deserve further investigation.

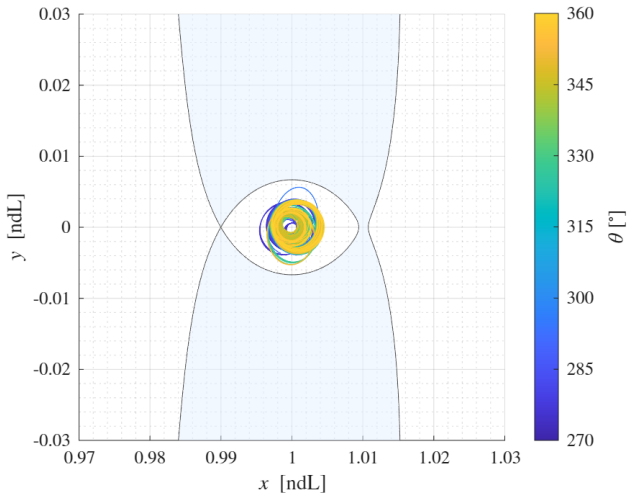

Figure 5.10: Moon impacts within the interval $270° \leq \theta \leq 360°$ and $260° \leq \alpha_0 \leq 330°$.

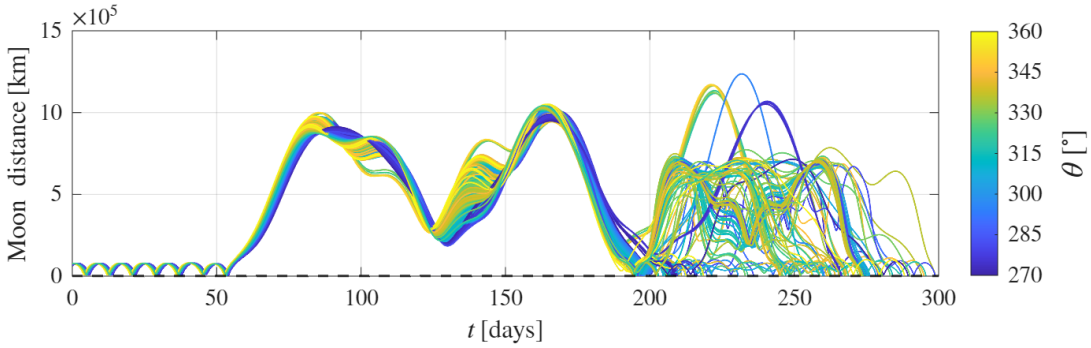

Figure 5.11: Distance from the Moon of the trajectories within the interval $270° \leq \theta \leq 360°$ and $260° \leq \alpha_0 \leq 330°$ that result in lunar impact.

The escape trajectories are shown in Fig. 5.12 and Fig. 5.13 and they exhibit a very similar global behaviour for both L_1 and L_2 escape cases. In all configurations, the parameter θ varies within the interval $0° \leq \theta \leq 100°$, while α_0 assumes fixed representative values. In agreement with the classification proposed by Boudad, these trajectories can be iden-

tified as direct escapes. The spacecraft departs from the NRHO and rapidly leaves the Earth-Moon region without undergoing long intermediate capture phases. This suggests that the corresponding regions of the escape map are not only dynamically robust, but also associated with relatively fast escape mechanisms. A clear influence of the initial Earth-Moon-Sun configuration can be observed, as the value of α_0 primarily determines the direction of departure. The individual trajectory shapes then exhibit moderate variations as a function of θ, while preserving the same global escape pattern. An additional feature can be observed in Fig. 5.12a, and can also be noticed in Fig. 5.13b, where trajectories associated with higher values of θ exhibit small oscillatory deviations before definitely departing.

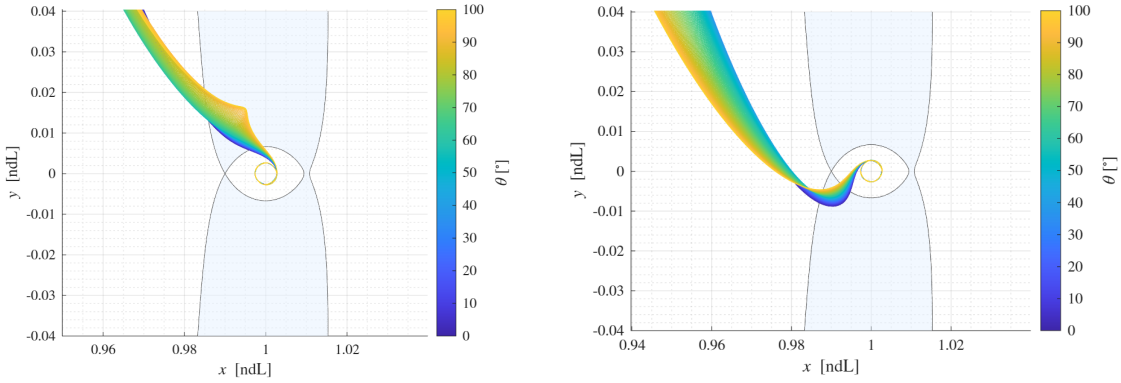

(a) L_1 direct escapes within the interval $0° \leq \theta \leq 100°$ and $\alpha_0 = 80°$.

(b) L_1 direct escapes within the interval $0° \leq \theta \leq 100°$ and $\alpha_0 = 180°$.

Figure 5.12: L_1 direct escapes from the orbit with $JC = 3.0271$ and $SI = 1.6908$.

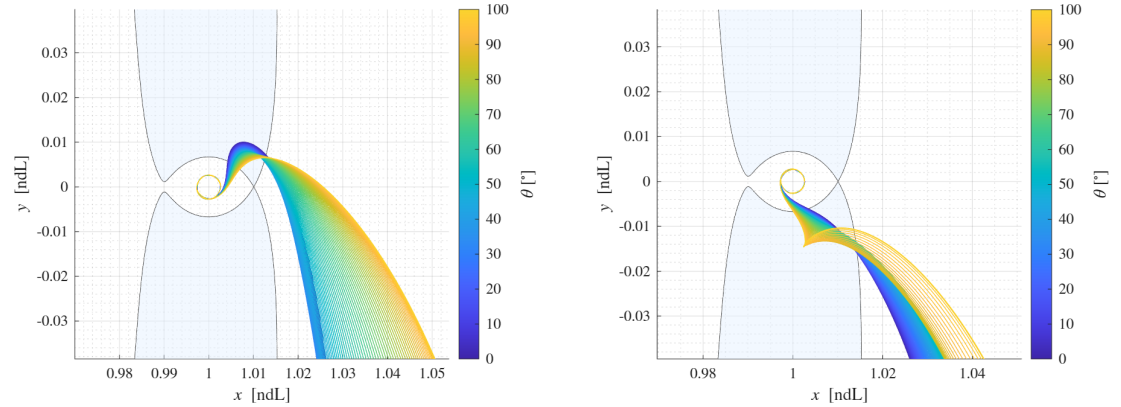

(a) L_2 direct escapes within the interval $0° \leq \theta \leq 100°$ and $\alpha_0 = 10°$.

(b) L_2 direct escapes within the interval $0° \leq \theta \leq 100°$ and $\alpha_0 = 255°$.

Figure 5.13: L_2 direct escapes from the orbit with $JC = 3.0271$ and $SI = 1.6908$.

Finally, the trajectories shown in Fig. 5.14 correspond to the interval $330° \leq \theta \leq 360°$ and $210° \leq \alpha_0 \leq 250°$. All trajectories within this region have been propagated and are classified according to their final outcome as L_1 escape, L_2 escape, or no escape.
Although the corresponding escape map suggests that the majority of these initial conditions are associated with non-escaping trajectories, the figure above reveals a more significant behaviour. Several trajectories classified as no escape exhibit a progressive drift toward an escape configuration, indicating that escape may occur for longer propagation times. In this sense, the distinction between slow escape and bounded motion appears to be strongly influenced by the selected propagation time.
Indeed, both L_1 and L_2 escapes observed in this region are characterised by relatively long departure and escape times. Considering that a propagation interval of ten months, that is a very long time, is adopted in the present analysis, therefore trajectories requiring comparable or longer times to satisfy the escape criteria cannot be regarded as particularly favourable from a disposal design perspective.

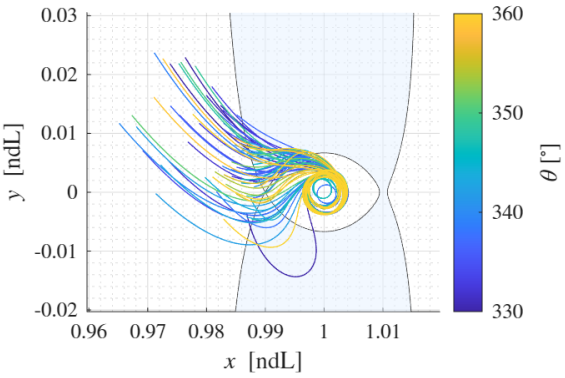

(a) L_1 escape trajectories.

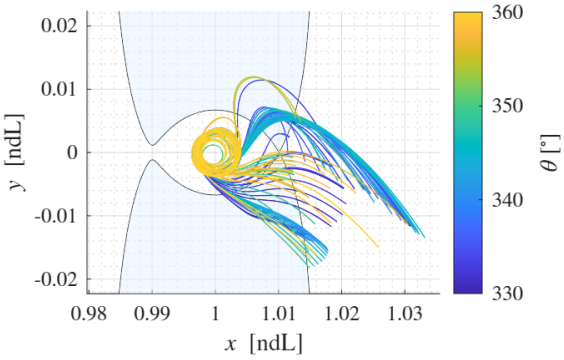

(b) L_2 escape trajectories.

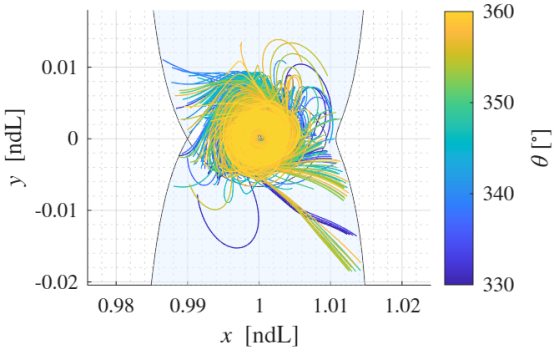

(c) No escape trajectories.

Figure 5.14: Trajectories within the interval $330° \leq \theta \leq 360°$ and $210° \leq \alpha_0 \leq 250°$ of the orbit with $JC = 3.0271$ and $SI = 1.6908$.

5.1.2. Orbit with JC = 3.0474 and SI = 1.2971

The escape maps corresponding to the Gateway orbit, characterised by a 9:2 synodic resonance, are shown in Fig. 5.15.

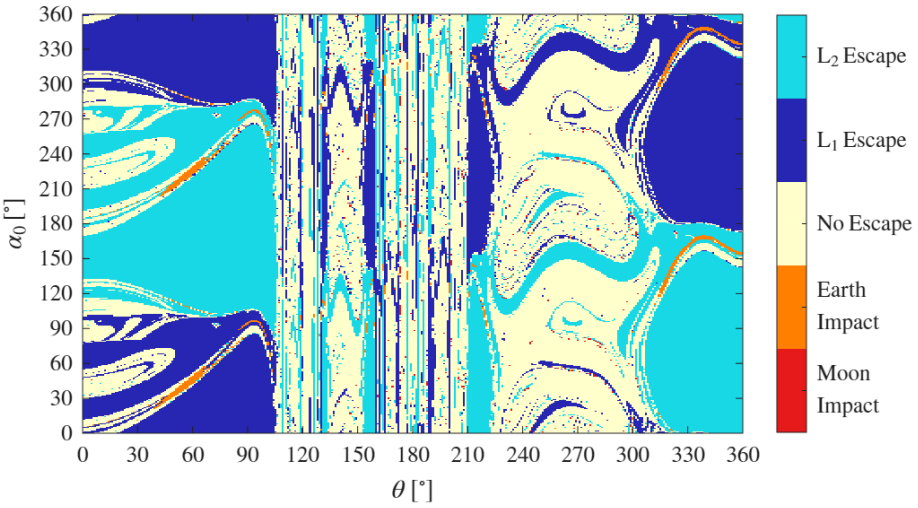

(a) Positive manifold perturbation.

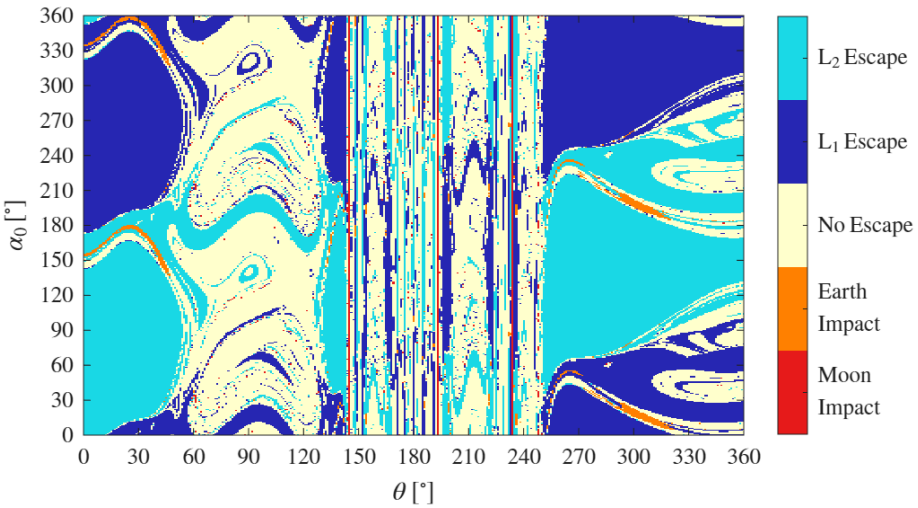

(b) Negative manifold perturbation.

Figure 5.15: Escape maps as a funtion of α_0 for the orbit with $JC = 3.0474$ and $SI = 1.2971$.

As in the previous case, invariant manifolds are generated through both positive and negative perturbations. The general considerations discussed for the first orbit are still valid, therefore, the analysis here focuses on the distinctive features of this configuration. A notable aspect is the apparent symmetry between the escape maps associated with the two manifold directions. The overall structure of the escape regions exhibits a mirrored

organisation, which is probably related to the resonant nature of the orbit.
As previously observed, a fragmented and highly structured region appears for specific values of θ, corresponding to passages near the Moon. This region suggests the presence of chaotic dynamics, whereas other intervals of θ present more coherent and robust escape domains. Also in this case, the relation between α_0 and α_{cross} as a function of θ is reported in Fig. 5.16.

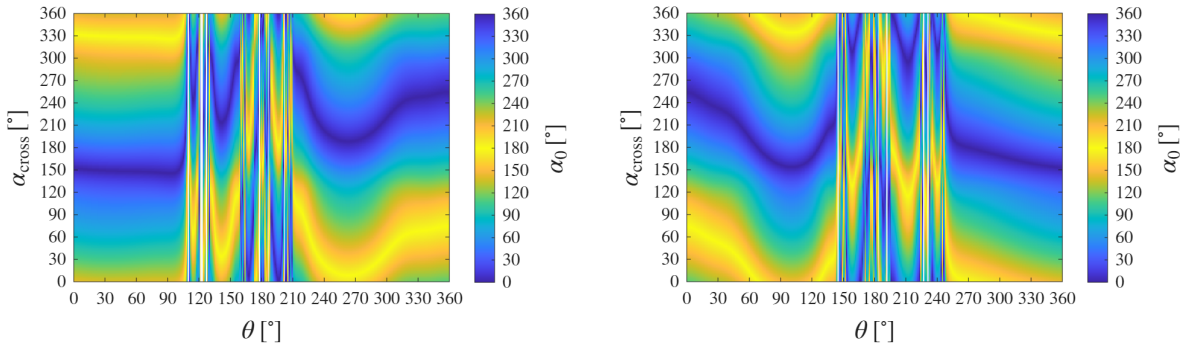

(a) Positive manifold perturbation.

(b) Negative manifold perturbation.

Figure 5.16: Relation between α_0 and α_{cross} for the orbit with $JC = 3.0474$ and $SI = 1.2971$.

The relation between α_0 and α_{cross} exhibits a behaviour consistent with that observed for the previous orbit. The overall structure suggests a well-defined mapping between the initial configuration and the configuration at the first crossing of the Sun's sphere of influence, with variations depending on θ. As expected from the resonant nature of the Gateway orbit, the two maps associated with positive and negative manifold perturbations display an almost symmetric organisation.
A distinctive feature in this case is the presence of vertical white bands in the plots. These regions correspond to values of θ for which the trajectory does not satisfy the switching condition between the Earth-Moon and Sun-Earth reference frames. In such cases, the spacecraft remains entirely within the Earth-Moon sphere of influence throughout the considered propagation interval. The escape maps reformulated in terms of α_{cross} are shown in Fig. 5.17.

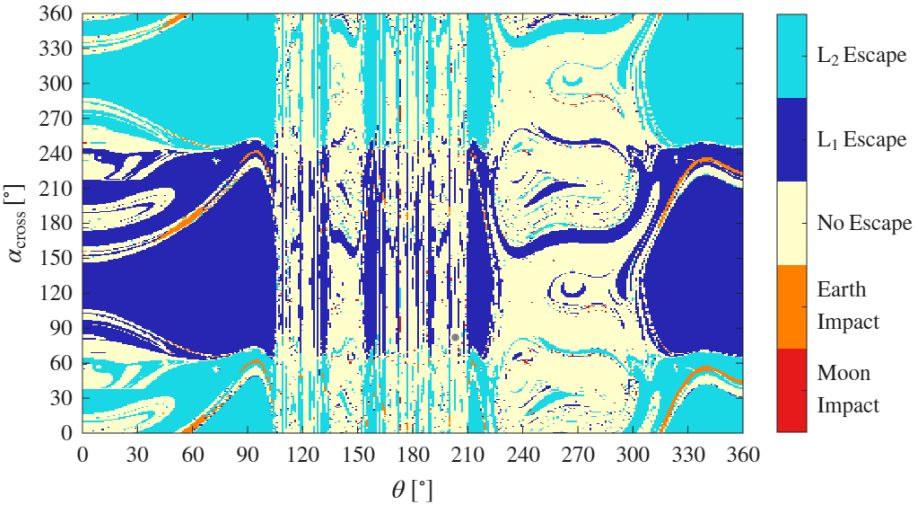

(a) Positive manifold perturbation.

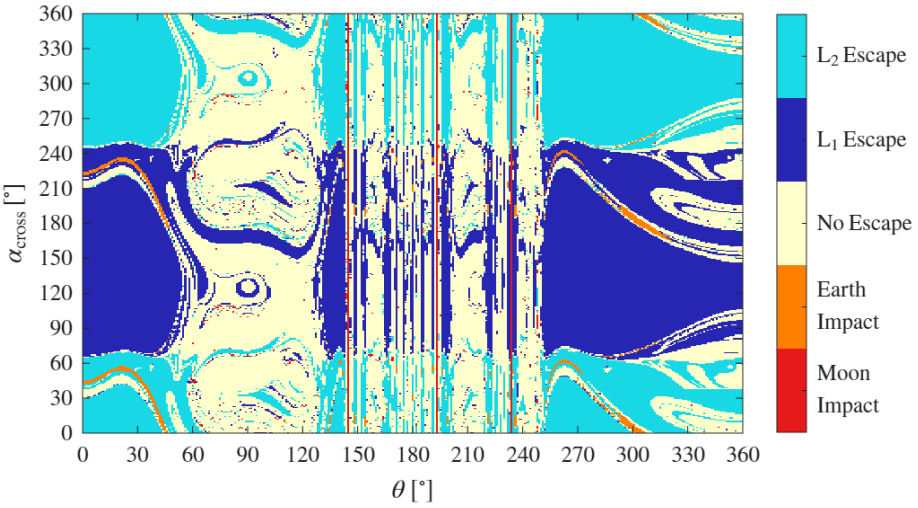

(b) Negative manifold perturbation.

Figure 5.17: Escape maps as a funtion of α_{cross} for the orbit with $JC = 3.0474$ and $SI = 1.2971$.

When expressed in terms of α_{cross}, the overall structure of the escape regions remains largely consistent with that observed in the α_0 parametrisation. The main dynamical features, including the robust escape domains and the fragmented central region, are preserved. However, the distinction between L_1 and L_2 escapes appears more regular in this representation. The escape regions show a clearer separation as a function of α_{cross}, suggesting a more direct geometrical dependence of the escape direction on the configuration at the switching condition. Apart from this increased regularity, the global organisation of the map does not exhibit substantial differences with respect to the α_0 formulation.

The trajectories leading to Earth and Moon impacts for both positive and negative manifold perturbations are shown in Fig. 5.18 and Fig. 5.19, respectively.
The general considerations discussed for the previous orbit remain applicable also in this case. The trajectories exhibit similar global behaviours, with Earth and Moon impacts occurring through dynamical mechanisms analogous to those already described.

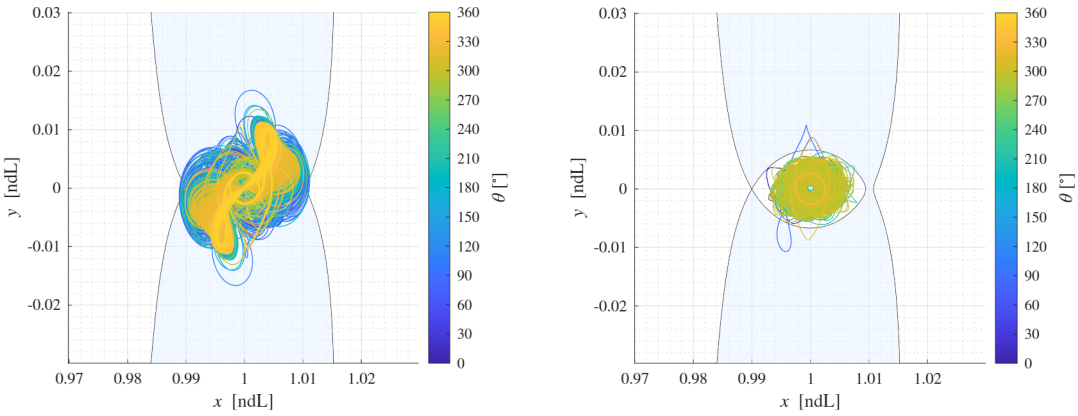

(a) Earth impacts. (b) Moon impacts.

Figure 5.18: Impact trajectories for the positive perturbed manifold of the orbit with $JC = 3.0474$ and $SI = 1.2971$.

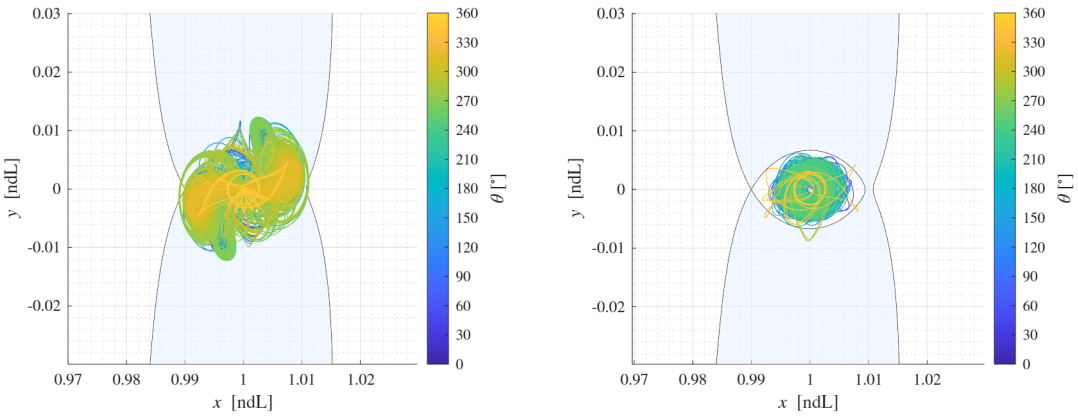

(a) Earth impacts. (b) Moon impacts.

Figure 5.19: Impact trajectories for the negative perturbed manifold of the orbit with $JC = 3.0474$ and $SI = 1.2971$.

However, two particularly distinctive behaviours emerge in Fig. 5.19a. These trajectories deviate from the dominant patterns observed in the rest of the dataset and therefore deserve a more detailed inspection. For this reason, representative trajectories associated

with these behaviours have been isolated and are shown individually in Fig. 5.20. These trajectories correspond to $\theta = 338°$, $\alpha_0 = 186°$, and $\theta = 337°$, $\alpha_0 = 11°$.
The trajectory reported in Fig. 5.20a exhibits a structured motion characterised by repeated loops around the Earth-Moon region before the final evolution. Such behaviour suggests the presence of a temporary resonant interaction, where the spacecraft undergoes multiple revolutions in a quasi-periodic manner prior to impacting the Earth.
The trajectory in Fig. 5.20b, although less regular, displays a similarly intricate geometry, including a sharp excursion before re-entering the central region. These two behaviours were not observed in the previous case and therefore deserve a more detailed analysis.

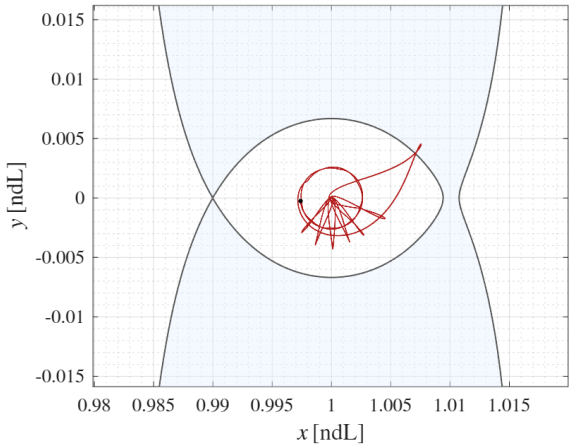

(a) Earth impact trajectory at $\theta = 338°$ and $\alpha_0 = 186°$.

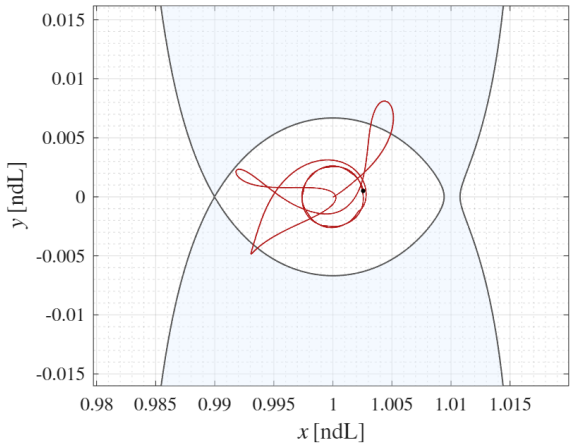

(b) Earth impact trajectory at $\theta = 337°$ and $\alpha_0 = 11°$.

Figure 5.20: Escape maps as a funtion of α_{cross} for the orbit with $JC = 3.0474$ and $SI = 1.2971$.

5.1.3. Orbit with JC = 3.0546 and SI = 1.0962

The escape maps for the orbit characterised by $JC = 3.0546$ and $SI = 1.0962$ are shown in Fig. 5.21.

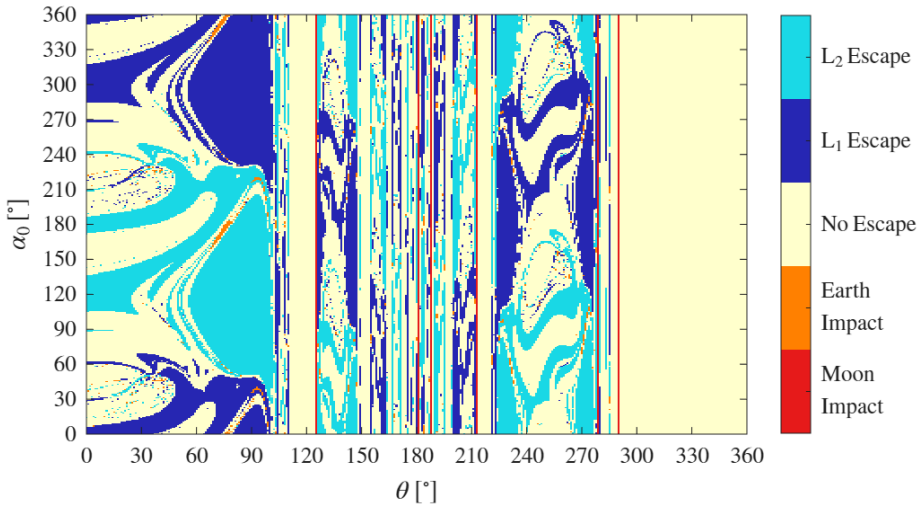

(a) Positive manifold perturbation.

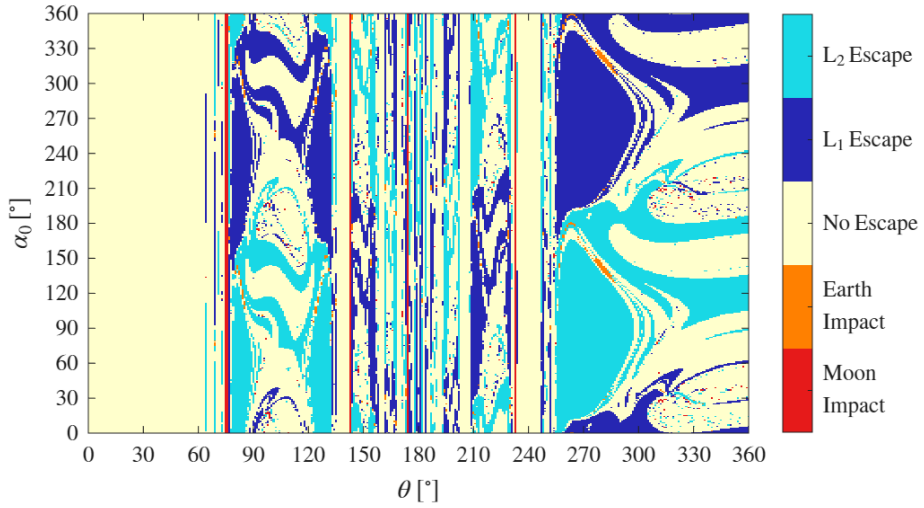

(b) Negative manifold perturbation.

Figure 5.21: Escape maps as a funtion of α_0 for the orbit with $JC = 3.0546$ and $SI = 1.0962$.

This configuration corresponds to the orbit with the lowest SI among the cases considered and is also the one located closest to the Moon. As in the previous cases, a certain degree of symmetry between positive and negative manifold perturbations can be observed, although it is less pronounced than for the resonant Gateway orbit. This may be attributed to the proximity of the present orbit to the 9:2 resonant configuration, which results in

partially comparable dynamical features.
The most fragmented and irregular structures are again observed for values of θ associated with close passages to the Moon, confirming the strong influence of lunar gravity in shaping the escape dynamics. However, in contrast with the previous cases, the robust escape regions are less extended. This behaviour is likely related to the low SI, which implies a weaker intrinsic instability of the orbit and therefore a reduced tendency of the manifolds to diverge rapidly.
Both maps exhibit well-defined vertical bands of no escape, probably corresponding to intervals of θ for which the switching condition between the Earth-Moon and Sun-Earth systems is not satisfied. In addition, distinct Moon-impact vertical stripes appear for specific values of θ, extending across almost the entire range of α_0. The fact that, for those θ, impact occurs independently of α_0 suggests that the Sun's influence is not the dominant factor in these cases. Instead, the trajectories remain confined within the Earth-Moon vicinity and ultimately impact the Earth regardless of the relative Sun-Earth-Moon configuration.

The relation between α_0 and α_{cross} for this configuration is shown in Fig. 5.22. The overall behaviour is consistent with that observed for the previous orbits, with a structured dependence on θ reflecting the geometrical link between the initial configuration and the one at the first crossing of the Sun's sphere of influence. The presence of well-defined vertical white bands confirms that, for specific values of θ, the switching condition between the Earth-Moon and Sun-Earth systems is not satisfied, so that the trajectory remains entirely within the Earth-Moon sphere of influence and α_{cross} cannot be defined.

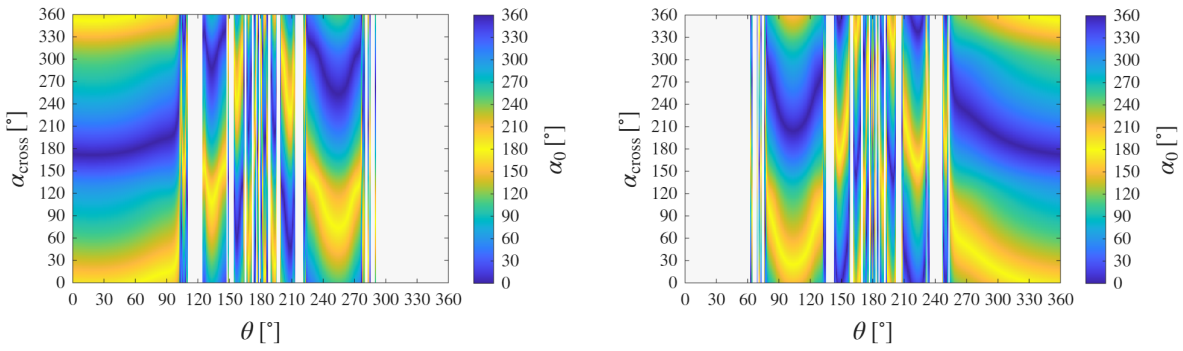

(a) Positive manifold perturbation.

(b) Negative manifold perturbation.

Figure 5.22: Relation between α_0 and α_{cross} for the orbit with $JC = 3.0546$ and $SI = 1.0962$.

The escape maps expressed in terms of α_{cross} are shown in Fig. 5.23. The overall structure is consistent with the α_0 parametrisation, and no additional qualitative features emerge with respect to the cases in the previous Sections. The global dynamical behaviour remains unchanged in this representation.

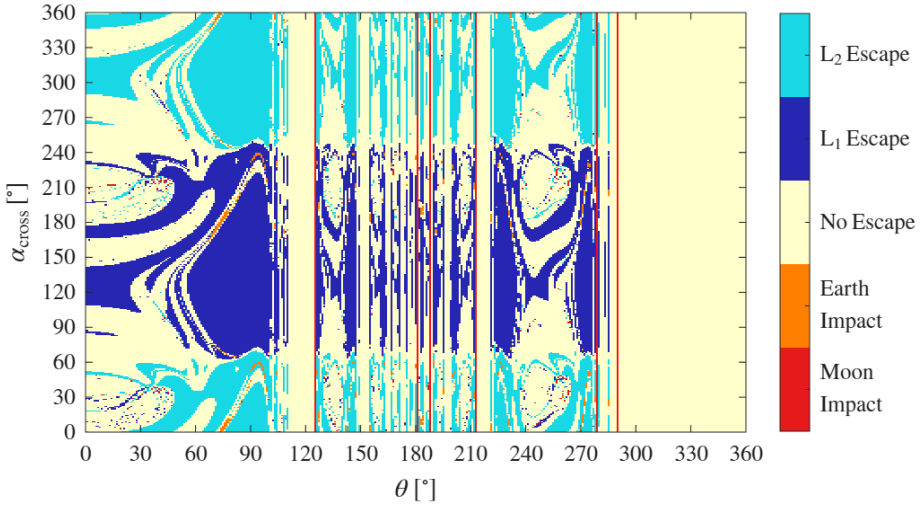

(a) Positive manifold perturbation.

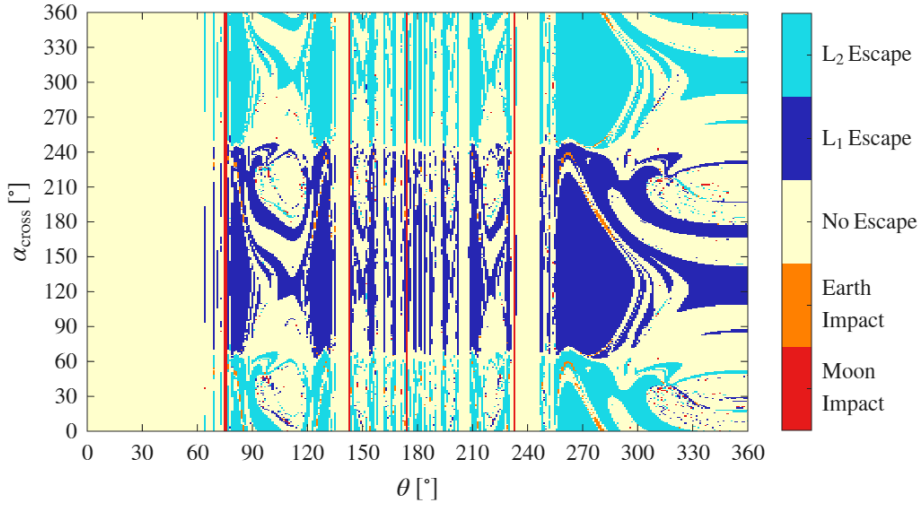

(b) Negative manifold perturbation.

Figure 5.23: Escape maps as a funtion of α_{cross} for the orbit with $JC = 3.0546$ and $SI = 1.0962$.

The trajectories leading to Earth and Moon impacts for both positive and negative manifold perturbations are shown in Fig. 5.24 and Fig. 5.25. The general dynamical behaviour is consistent with that observed for the previous configurations, and no additional distinctive features emerge. The impact trajectories follow patterns analogous to those already discussed, without exhibiting particularly structured or resonant behaviours that would

require separate analysis.

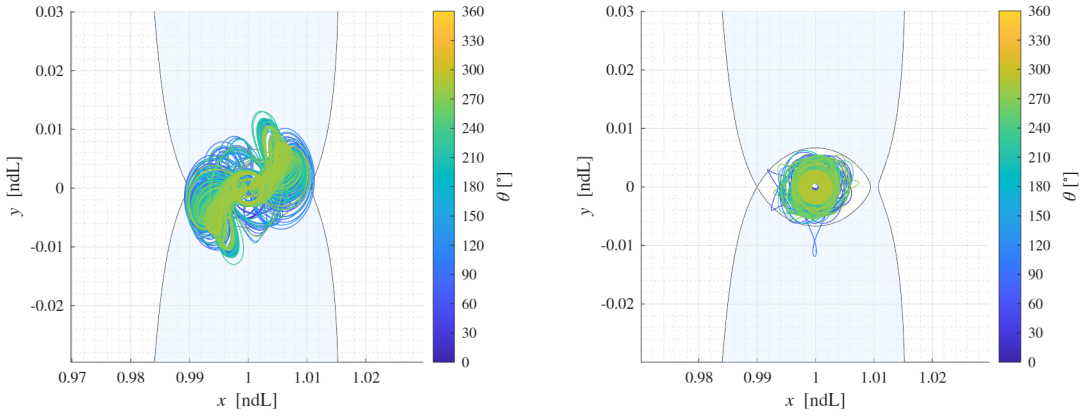

(a) Earth impacts. (b) Moon impacts.

Figure 5.24: Impact trajectories for the positive perturbed manifold of the orbit with $JC = 3.0546$ and $SI = 1.0962$.

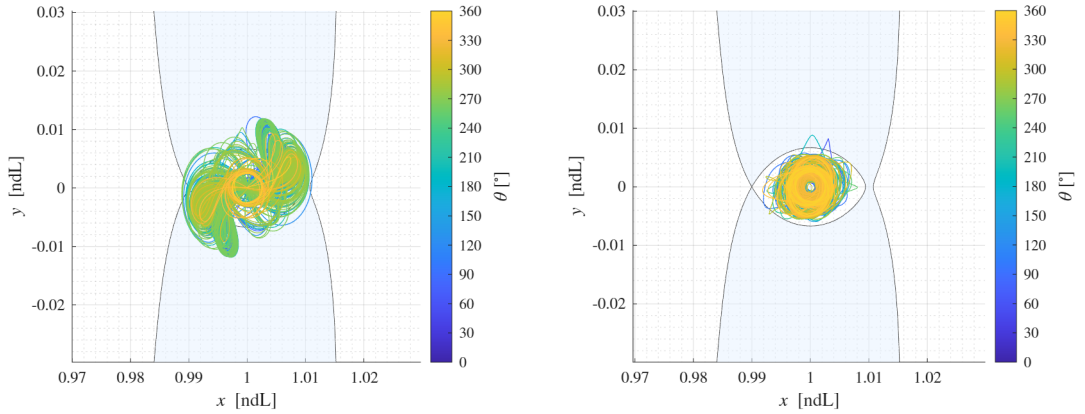

(a) Earth impacts. (b) Moon impacts.

Figure 5.25: Impact trajectories for the negative perturbed manifold of the orbit with $JC = 3.0546$ and $SI = 1.0962$.

5.1.4. Orbit with JC = 3.0176 and SI = 1.0944

Fig. 5.26 presents the escape maps corresponding to the orbit with $JC = 3.0176$ and $SI = 1.0944$, which lies close to the boundary of the analysed NRHO family and is characterised by a very low SI, similar to the one of the previous Section.

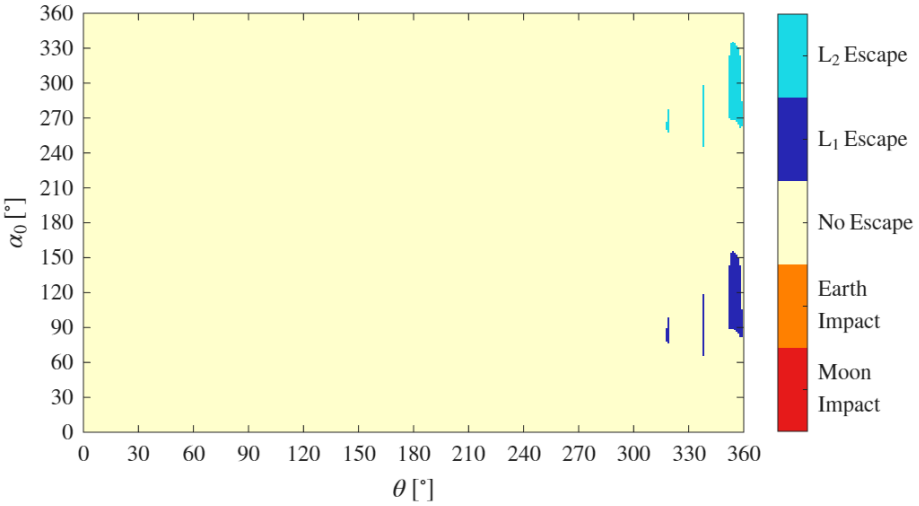

(a) Positive manifold perturbation.

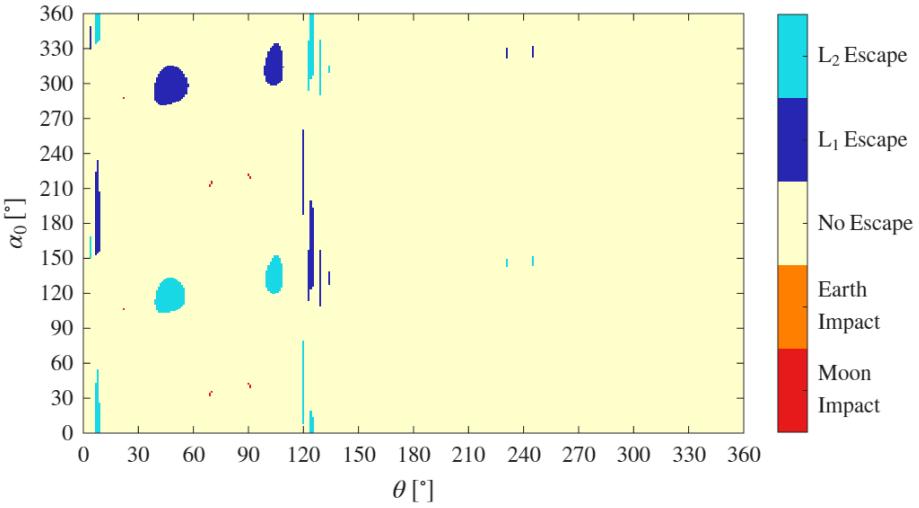

(b) Negative manifold perturbation.

Figure 5.26: Escape maps as a funtion of α_0 for the orbit with $JC = 3.0176$ and $SI = 1.0944$.

A predominant non-escaping behaviour is immediately evident, as the majority of initial conditions do not escape over the considered propagation interval. This behaviour is consistent with the very low SI, indicating a weak intrinsic instability of the orbit and a limited divergence of the associated invariant manifolds. Comparing it to the previous configurations, characterised by almost the same SI, strong difference can be noted, the escape regions are almost absent, and only isolated escape or impact events can be identified.

To better understand the behaviour it is useful to know when the switch of the dynamical model occurs. From the escape maps alone it is not possible to clearly determine whether

this condition is satisfied. For this reason, it is necessary to look at the relation between α_0 and α_{cross} reported in Fig. 5.27. This representation explicitly indicates the intervals of θ for which the switching occurs. From this mapping it can be observed that, for a large portion of the parameter space, the trajectories do not reach the switching condition and remain entirely within the Earth-Moon sphere of influence. This suggests a particularly slow manifold evolution, with trajectories requiring long times to depart from the vicinity of the nominal orbit.

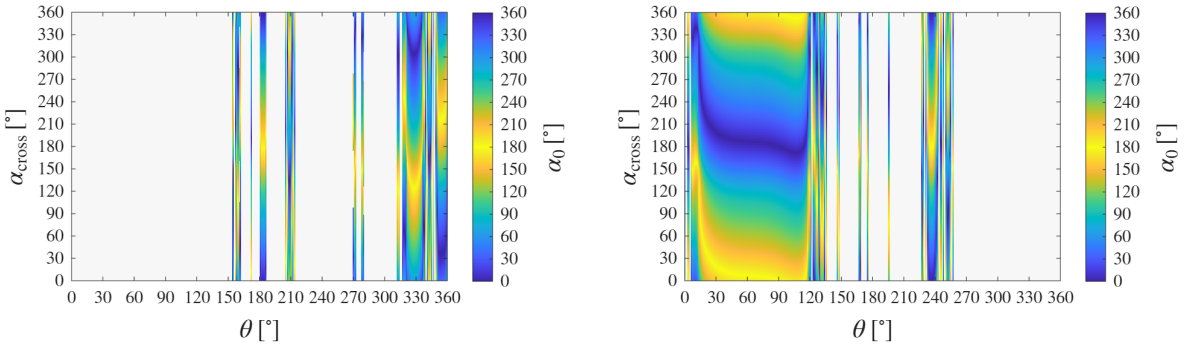

(a) Positive manifold perturbation.

(b) Negative manifold perturbation.

Figure 5.27: Relation between α_0 and α_{cross} for the orbit with $JC = 3.0176$ and $SI = 1.0944$.

For completeness, the escape maps expressed as a function of α_{cross} are reported in Fig. 5.28. The overall behaviour is fully consistent with that observed in the α_0 parametrisation, and no additional qualitative features emerge. As expected from the limited occurrence of switching events, the map is largely dominated by non-escaping trajectories, confirming the slow manifold evolution discussed above.

With regard to impact trajectories, only the case shown in Fig. 5.29 is reported, since impacts occur exclusively on the Moon and only for one manifold direction. No additional distinctive features emerge from the trajectory analysis, and the dynamical behaviour is consistent with the trends discussed in the previous configurations.

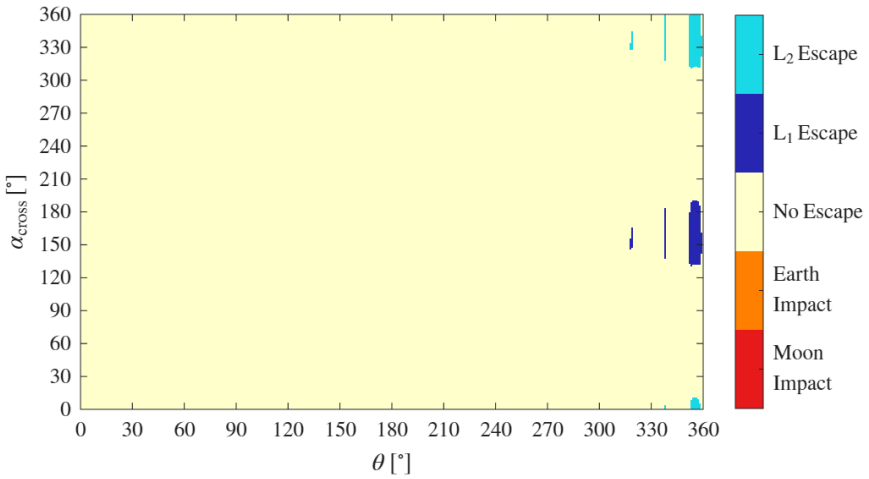

(a) Positive manifold perturbation.

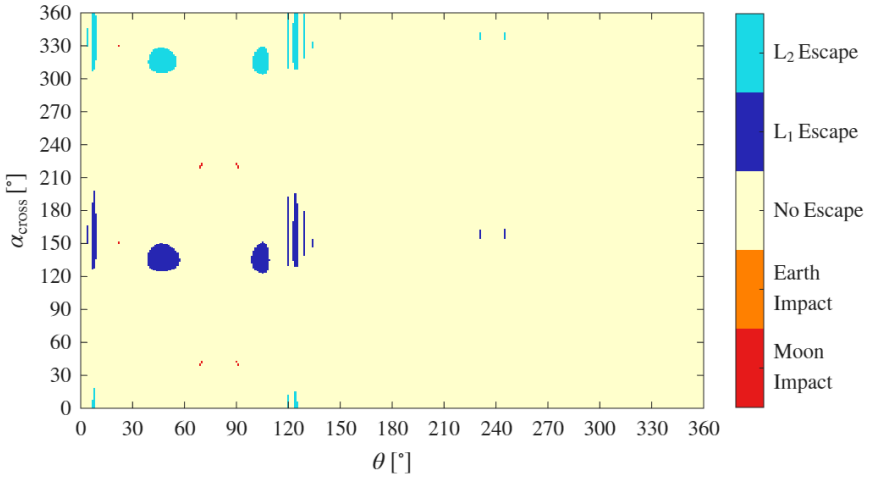

(b) Negative manifold perturbation.

Figure 5.28: Escape maps as a funtion of α_{cross} for the orbit with $JC = 3.0176$ and $SI = 1.0944$.

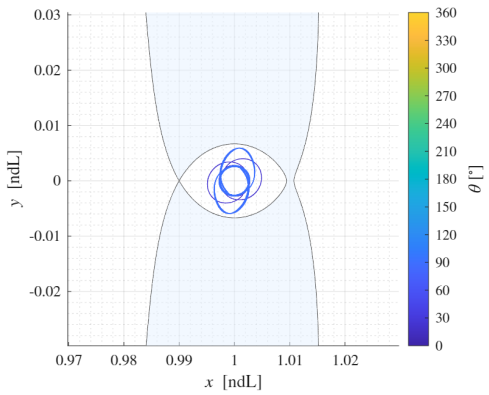

Figure 5.29: Impact trajectories for the negative perturbed manifold of the orbit with $JC = 3.0176$ and $SI = 1.0944$.

5.2. Interpretation of the escape dynamics

To better understand the mechanisms governing heliocentric escape, a dedicated analysis of two dynamical indicators is performed. The aim is to identify which factors may influence or characterise the different escape behaviours observed in the previous maps. In particular, attention is focused on the JC, as an energetic parameter, and on the FTLE, as a measure of local dynamical sensitivity.

5.2.1. Energy consideration

As discussed in Sec. 3.6, the JC defines the energy level of the system. For this reason, a dedicated analysis is performed with specific focus on its evolution along the propagated manifolds.
It is important to recall that the L_1 and L_2 gateways close when the system energy is equal to, or lower than, the energy associated with the respective Lagrange point. Under such conditions, transit through these equilibrium regions is not permitted. Therefore, for escape through L_1 or L_2 to occur, the corresponding energetic condition must be satisfied in both the Earth-Moon and Sun-Earth systems.
In this Section, the orbit with $JC = 3.0271$ and $SI = 1.6908$ is considered, as it exhibits well-defined dynamical regions. In particular, to study the evolution along the manifold, trajectories starting at $\alpha_0 = 0$ are analysed. For clarity, θ is varied from $0°$ to $360°$, considering one trajectory every $10°$.

The evolution of the JC in the Earth-Moon frame is shown in Fig. 5.30. As expected, the JC remains constant while the spacecraft is within the Earth-Moon system, and varies only after the switching to the Sun-Earth frame occurs. This confirms the consistency of the multi-frame propagation.
For trajectories that eventually escape, a clear increase of the JC in the EM representation is observed after the escape instant, indicated by the marker. This behaviour reflects the progressive dominance of the Sun's gravitational influence once the spacecraft departs from the Earth-Moon vicinity.
Conversely, for trajectories that remain bounded or result in impact within the Earth-Moon system, the JC remains confined within a limited range and does not exhibit the same growth trend.

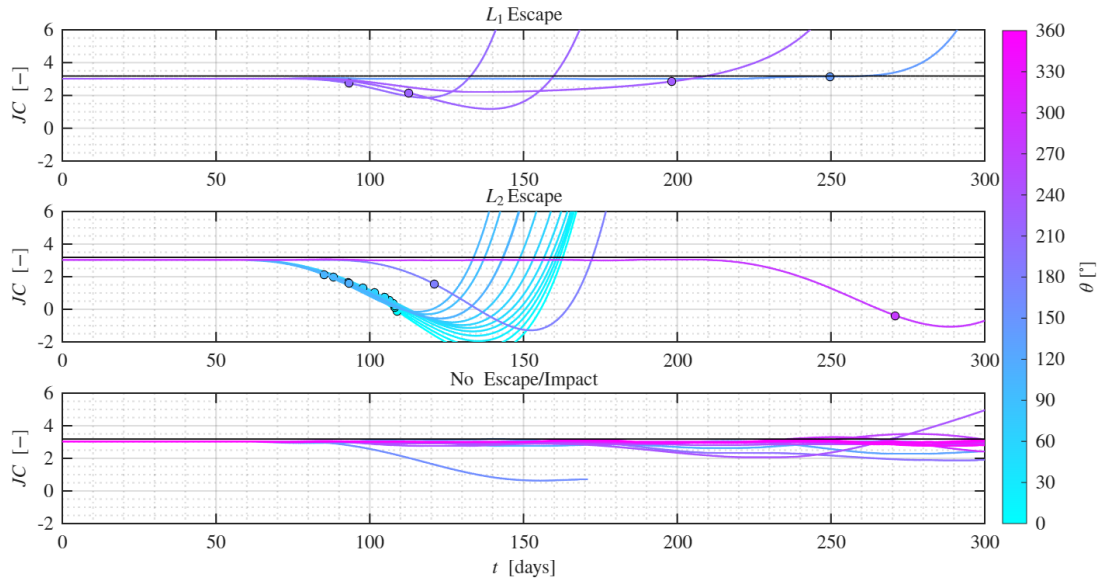

Figure 5.30: JC evolution in the Earth-Moon system.

The evolution of the JC in the Sun-Earth frame is reported instead in Fig. 5.31. In this case, the JC remains constant while the spacecraft is within the Sun-Earth system and varies during the Earth-Moon phase, as expected.
The trend of the JC is comparable to the evolution of the Hamiltonian reported in the studies by Boudad and Davis. It should be recalled that their analysis is conducted within the BCR4BP framework, in which the energy parameter is the Hamiltonian. Since this model does not admit an integral of motion, the Hamiltonian is not conserved along the trajectory. Nevertheless, its evolution shows a stabilising behaviour as the spacecraft moves away from the Earth-Moon vicinity, in agreement with the trend observed here for the JC.
For escaping trajectories, the JC in the Sun-Earth frame decreases below the value associated with the L_1 and L_2 equilibrium points. Since lower JC corresponds to higher energy, this condition is necessary to allow transit through the gateway and thus enable escape. In contrast, many of the non-escaping trajectories do not satisfy this energetic requirement.

The analysis of the JC in the Sun-Earth frame reveals an additional important aspect. From the time evolution along the manifolds, it can be observed that trajectories leading to escape already exhibit lower JC values since the first entrance into the Sun's sphere of influence.
Motivated by this observation, a JC map is constructed as a function of α_0 and θ, where the colorbar represents the value of the JC evaluated at the first switching instant as

shown in Fig. 5.32.

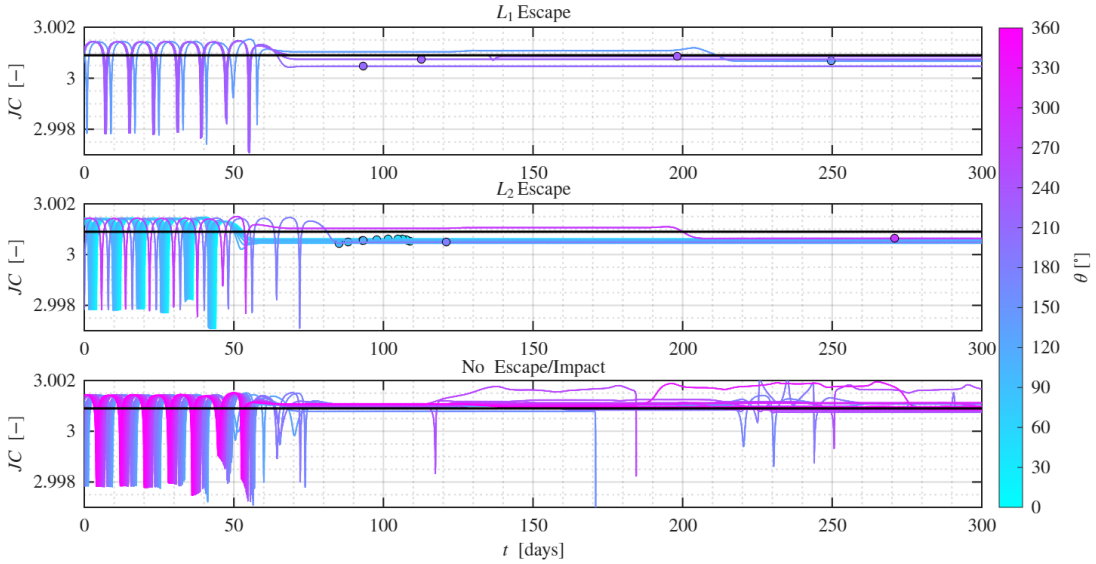

Figure 5.31: JC evolution in the Sun-Earth system.

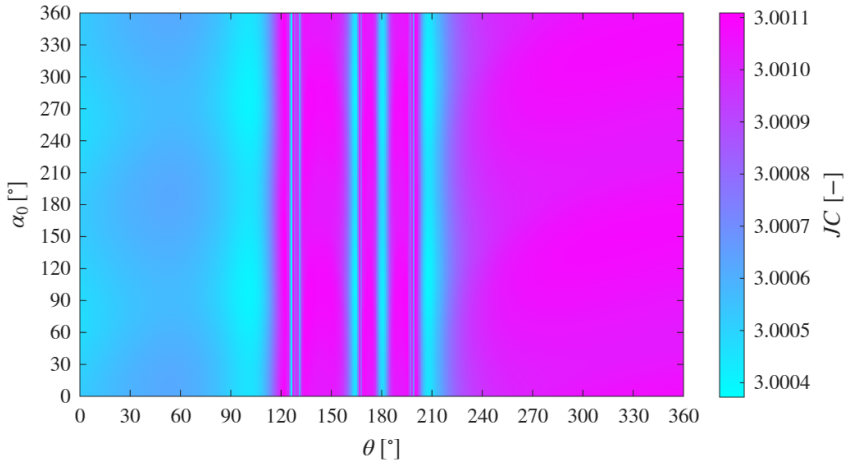

Figure 5.32: JC map at the forst cross in the Sun's sphere of influence in the Sun-Earth system.

A relation seems to emerge between the JC value at first switch and the final outcome of the trajectory (reported in Fig.5.1a). Regions characterised by lower JC values correspond to those previously identified as direct escapes through the trajectory analysis. Conversely, higher JC values are associated with bounded motion or impact cases, or trajectories that escape with higher time of flight.

This result indicates that the JC evaluated at the first Sun-Earth transition provides a reliable early indicator of the final dynamical behaviour. In this sense, the map represents

a useful predictive tool, potentially allowing the identification of escape regions without requiring full propagation over the entire time interval.

5.2.2. Chaotic behaviour

The FTLE, introduced in Sec. 4.7, is now analysed along the trajectories to investigate its possible relation to the escape outcome. The FTLE evolution in the Earth-Moon frame is reported in Fig. 5.33. Since the exponent is computed only within the active dynamical model, gaps in the curves correspond to time intervals during which the spacecraft evolves in the Sun-Earth system.

In the Earth-Moon frame, the FTLE does not reveal particularly distinctive features associated with the final outcome. Prior to departure, its evolution resembles the behaviour reported by [42] for the NRHO itself, reflecting the intrinsic instability properties of the orbit. However, no clear separation between escape and non-escape trajectories can be identified in this frame.

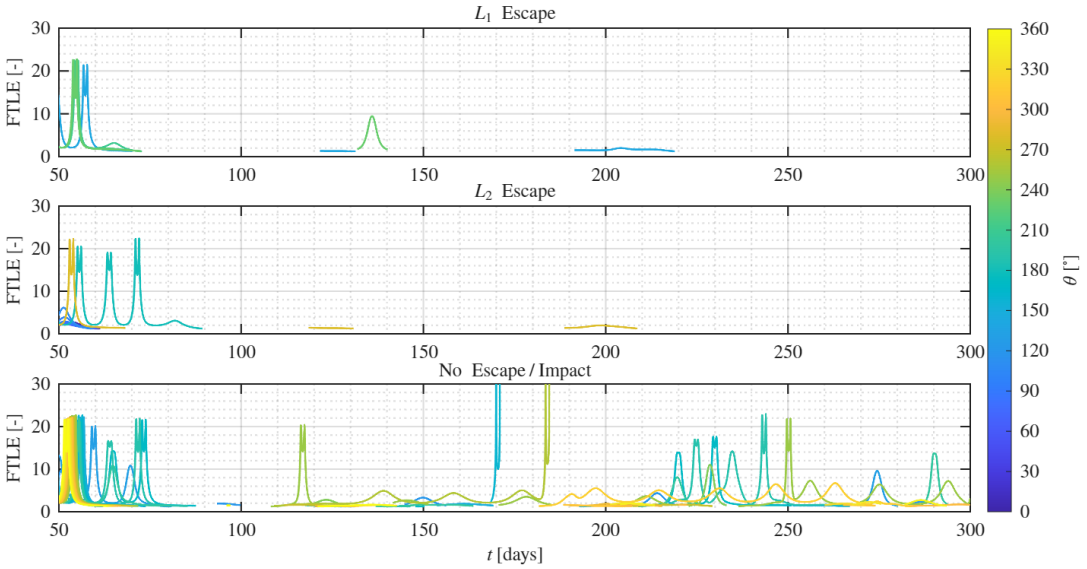

Figure 5.33: FTLE evolution in the Earth-Moon system.

The situation is different in the Sun-Earth frame shown in Fig. 5.34. For trajectories leading to escape, the FTLE exhibits a decreasing trend after the first switching instant, eventually stabilising at relatively low values. This behaviour suggests that, once the energetic gateway condition is satisfied, the motion becomes progressively less sensitive to local perturbations to small variations in the initial conditions in the Sun-Earth environment.

Conversely, trajectories that remain bounded or result in impact display a more irregular

and fluctuating FTLE evolution, indicating persistent local sensitivity to initial conditions.

Similarly to the analysis performed for the JC, particular attention is devoted to the FTLE value at the first switching instant. It can be observed that escaping trajectories tend to exhibit lower FTLE values already at their first entrance into the Sun-Earth sphere of influence.
Motivated by this observation, an FTLE map is constructed as a function of α_0 and θ, where the colour scale represents the exponent evaluated at the first switching event as shown in Fig. 5.35.

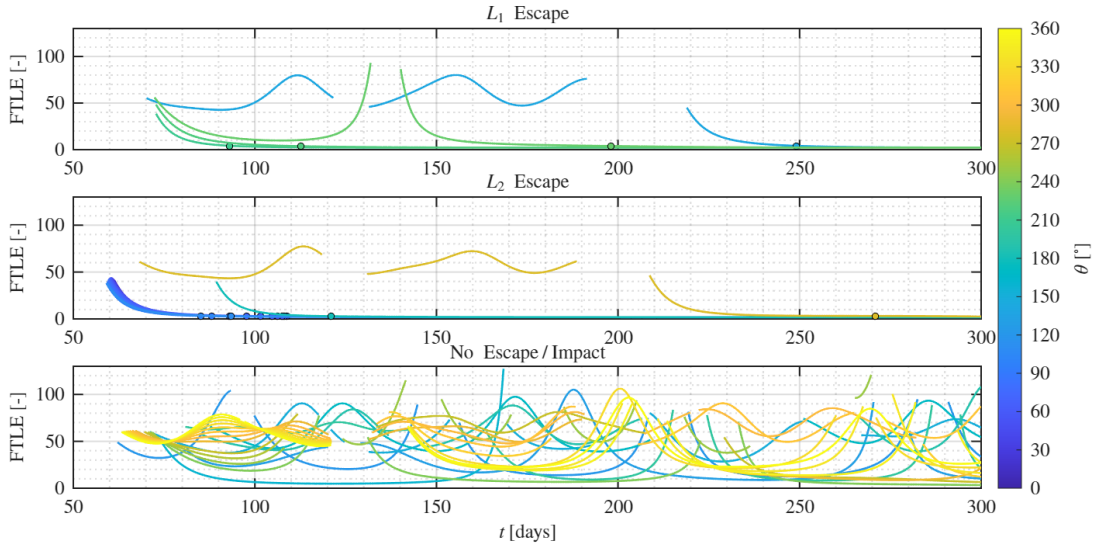

Figure 5.34: FTLE evolution in the Sun-Earth system.

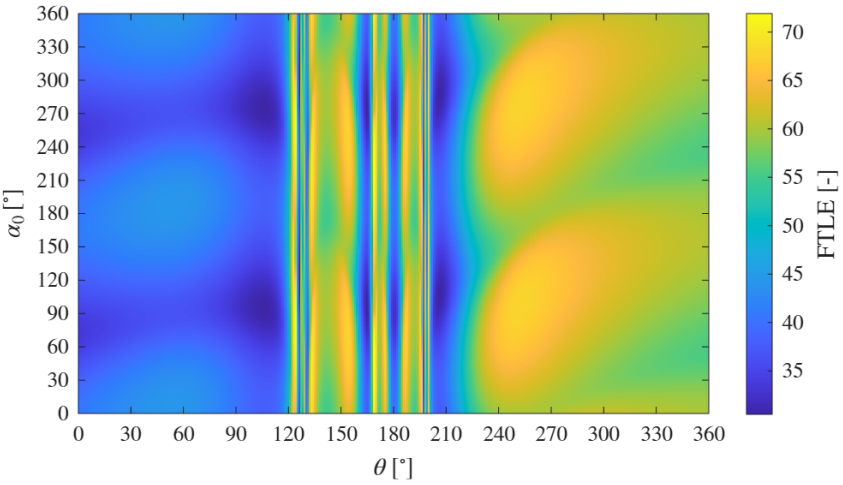

Figure 5.35: FTLE map at the forst cross in the Sun's sphere of influence in the Sun-Earth system.

A connection emerges between the FTLE at first switch and the final outcome: regions characterised by lower FTLE values correspond predominantly to direct escape cases, whereas higher FTLE values are associated with bounded motion or impacts. Compared to the JC map, the FTLE map appears even more sensitive in discriminating between different dynamical behaviours.

5.2.3. Combined analysis of Jacobi Constant and Finite Time Lyapunov Exponent

To further explore the combined role of energy and local dynamical instability at the Sun-Earth transition, the values of the JC and the FTLE evaluated at the first switching instant are plotted against each other in Fig. 5.36, for different values of α_0 and θ.

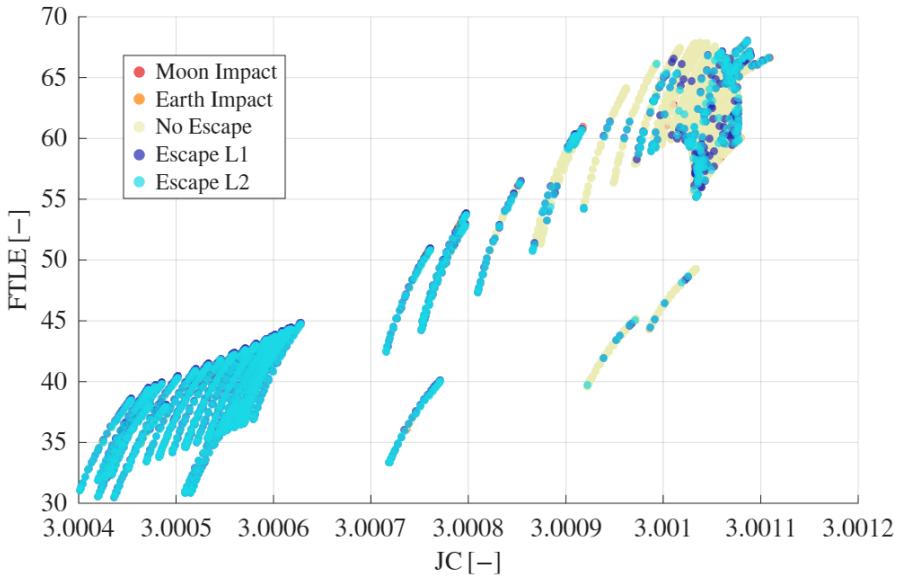

Figure 5.36: Relation between JC and FTLE.

Although the explicit dependence on α_0 and θ is not retained in this representation, the plot provides a global view of the relationship between energetic and dynamical indicators at the transition. It can be observed that lower values of both JC and FTLE are generally associated with direct escape cases. In contrast, higher FTLE values and/or higher JC values correspond to a wider variety of outcomes, including bounded motion and impacts. However, the separation between different dynamical behaviours is not sharp, and overlapping regions are present. This suggests that neither parameter alone is sufficient to uniquely determine the final outcome. Rather, escape appears to result from a combined condition involving both energetic accessibility and a favourable local dynamical structure.

6 | Conclusions and future works

This Chapter summarises the main results achieved in this work and provides an overall view of the study. Sec. 6.1 presents the conclusions drawn from the analyses carried out throughout the Thesis, whereas Sec. 6.2 outlines possible extensions and future research that could further develop and apply the results presented.

6.1. Summary and conclusions

The increasing number of lunar missions and the expected long-term use of NRHOs make the definition of effective EoL strategies a relevant topic. Among the possible solutions, heliocentric disposal is generally preferred from mitigation guidelines if supported by long-term simulations in accurate dynamical models. For this reason, the present Thesis focuses on heliocentric escape from Earth-Moon L2 NRHOs.
Previous investigations have shown that the success of heliocentric disposal strongly depends on the relative configuration of the Sun, Earth, and Moon. However, this dependence has not been deepen analysed.
More recently, Bolis et al. [36] introduced an approach based on the coupled CR3BP model and on invariant manifold dynamics. This framework has been adopted in the present Thesis and further developed to perform a detailed parametric analysis of the influence of the Sun-Earth-Moon configuration on heliocentric escape from NRHOs, with particular emphasis on geometrical phasing and dynamical structures.

The present work has investigated the conditions under which a spacecraft departing from an Earth-Moon L2 NRHO can successfully escape the cislunar region and enter a heliocentric disposal trajectory. The analysis has been carried out by verifying when the trajectory crosses the Sun-Earth ZVCs, therefore satisfying both geometrical and energetic escape conditions.
A systematic parametric study has been performed by varying the phase angle θ along the NRHO and the initial Sun-Earth-Moon configuration α_0. For each configuration, trajectories generated along the unstable manifold have been propagated within the cou-

pled CR3BP framework. The resulting escape maps, constructed for four representative NRHOs, provide a global view of the possible dynamical outcomes.
The escape maps reveal the presence of well-defined regions characterised by regular and coherent behaviour, as well as fragmented areas associated with increased dynamical sensitivity. Despite the complexity of the dynamics, these maps constitute a useful tool for preliminary mission design, as they allow the identification of favourable and robust escape windows depending on the orbital phase and on the relative configuration of the primaries.
In order to highlight more physically meaningful correlations, the analysis has been reformulated using the parameter α_{cross}, defined as the phase angle α related to the Sun-Earth-Moon configuration at the time in which the dynamical model is first switched from Earth-Moon to Sun-Earth CR3BP. When expressed in terms of α_{cross}, the overall structure of the escape maps remains substantially unchanged. However, this alternative parametrisation allows a clearer geometrical interpretation of the results. In particular, although a structured organisation is already visible when parametrising with respect to α_0, a clearer correlation emerges between α_{cross} and the selection of the escape gateway through L_1 or L_2.
A deeper understanding of the observed patterns has been achieved by analysing representative trajectories and by introducing additional dynamical indicators. The JC and the FTLE have been evaluated along the trajectories, with particular attention to their values at the first crossing into the Sun's sphere of influence. Both parameters proved to be significant in interpreting the escape behaviour. In particular, their values at the first crossing show a relation with the success or failure of the heliocentric escape, suggesting that both energetic constraints and local dynamical sensitivity may contribute to the mechanism governing the escape.

6.2. Future works

The results obtained in this Thesis open several possible directions for further investigation, both from a dynamical and from an operational perspective.

A first natural extension concerns the dynamical model. The present analysis has been conducted within the coupled CR3BP framework under the assumption that the Earth-Moon orbital plane is coplanar with the ecliptic. As an intermediate step toward higher-fidelity modelling, the same coupled formulation could be extended by including the inclination of the Moon's orbit when performing the coordinate transformation between reference frames. This would allow assessing the impact of the coplanar assumption on the

identified escape structures. Subsequently, higher-fidelity models, such as the BCR4BP or ephemeris-based propagations, could be adopted to further evaluate the robustness of the escape windows highlighted in the present work.

A second relevant aspect concerns the temporal characteristics of the escape. The present study primarily focuses on the success or failure of the heliocentric escape, while only limited attention is devoted to the corresponding escape times. A systematic investigation of the time required to reach the Sun's sphere of influence and to satisfy the escape conditions, would provide additional insight into the practical viability of the identified configurations. The inclusion of escape time as an explicit analysis parameter could reveal further trade-offs between robustness and mission duration.

From an operational perspective, the escape maps constructed in this work may serve as a preliminary design tool for disposal strategies and as a structured basis for future optimisation procedures. The dynamical regions identified through the parametric analysis could be used to initialise optimisation algorithms aimed at minimising propellant consumption, transfer time, or a combination of mission objectives. In this context, the analysis could be extended to include explicit energetic cost metrics, assessing the effort required to close the ZVCs and enable escape under realistic constraints. The combined evaluation of configuration, escape time, and cost would provide a more complete framework for disposal design.

Overall, the framework developed in this Thesis establishes a structured basis for connecting dynamical systems analysis with practical disposal strategy development in the cislunar environment, and it may contribute to the definition of more systematic and reliable EoL solutions for future NRHO missions.

Bibliography

[1] L. Euler. De motu rectilineo trium corporum se mutuo attrahentium. *Novi commentarii academiae scientiarum Petropolitanae*, pages 144–151, 1767.

[2] J. L. Lagrange. Essai sur le probleme des trois corps. *Prix de l'académie royale des Sciences de paris*, 9:292, 1772.

[3] W. S. Koon, M. W. Lo, J. E. Marsden, and S. D. Ross. *Dynamical Systems, the Three-Body Problem and Space Mission Design*. Marsden Books, 2011.

[4] European Space Agency. Esa's annual space environment report. Technical Report GEN-DB-LOG-00288-OPS-SD, Issue 9.1, European Space Agency, October 2025.

[5] European Space Agency. Esa space debris mitigation requirements. Technical Report ESSB-ST-U-007, Issue 1, Revision 0, European Space Agency, October 2023.

[6] National Aeronautics and Space Administration. Process for limiting orbital debris. Technical Report NASA-STD-8719.14C, NASA, 2019.

[7] V. Szebehely. *Theory of Orbits: The Restricted Problem of Three Bodies*. Academic Press, 1967.

[8] K. C. Howell. Three-dimensional, periodic,'halo'orbits. *Celestial mechanics*, 32(1):53–71, 1984.

[9] P. Guardabasso, D. K. Skoulidou, L. Bucci, F. Letizia, S. Lemmens, and S. Lizy-Destrez. Cislunar debris mitigation: Development of a methodology to assess the sustainability of lunar missions. In *72nd International Astronautical Congress (IAC), Dubai*, 2021.

[10] P. Guardabasso, S. Lizy-Destrez, and M. Ansart. Lunar orbital debris mitigation: Characterisation of the environment and identification of disposal strategies. In *8th European Conference on Space Debris*, volume 8, 2021.

[11] D. Guzzetti, E. M. Zimovan-Spreen, K. C. Howell, and D. C. Davis. Stationkeeping analysis for spacecraft in lunar near rectilinear halo orbits. In *27th AAS/AIAA Space*

Flight Mechanics Meeting, volume 160, pages 3199–3218. American Astronautical Society San Antonio, 2017.

[12] K. K. Boudad, K. C. Howell, and D. C. Davis. Near rectilinear halo orbits in cislunar space within the context of the bicircular four-body problem. In *2nd IAA/AAS SciTech Forum, Moscow, Russia*, 2019.

[13] E. M. Zimovan-Spreen, K. C. Howell, and D. C. Davis. Near rectilinear halo orbits and their application in cis-lunar space. In *3rd IAA Conference on Dynamics and Control of Space Systems, Moscow, Russia*, volume 20, page 40, 2017.

[14] E. M. Zimovan-Spreen, K. C. Howell, and D. C. Davis. Near rectilinear halo orbits and nearby higher-period dynamical structures: orbital stability and resonance properties. *Celestial Mechanics and Dynamical Astronomy*, 132(5):28, 2020.

[15] W. S. Koon, M. W. Lo, J. E. Marsden, and S. D. Ross. Low energy transfer to the moon. *Celestial mechanics and dynamical astronomy*, 81(1-2):63–73, 2001.

[16] H. Lei and B. Xu. Transfers between libration point orbits of sun–earth and earth–moon systems by using invariant manifolds. *Journal of Engineering Mathematics*, 98(1):163–186, 2016.

[17] J. Zhang, E. Fantino, C. Du, Y. Wang, and H. Dai. Optimal transfers from an earth-moon unstable libration point orbit to the lunar surface. *Advances in Space Research*, 2025.

[18] V. K Srivastava, J. Kumar, and B. S. Kushvah. Halo orbit transfer trajectory design using invariant manifold in the sun-earth system accounting radiation pressure and oblateness. *Astrophysics and Space Science*, 363(1):17, 2018.

[19] C. Colombo, E. M. Alessi, W. Van der Weg, S. Soldini, F. Letizia, M. Vetrisano, M. Vasile, A. Rossi, and M. Landgraf. End-of-life disposal concepts for libration point orbit and highly elliptical orbit missions. *Acta Astronautica*, 110:298–312, 2015.

[20] R. Armellin, P. Di Lizia, M. Rasotto, G. Di Mauro, and M. Landgraf. Disposal strategies for spacecraft in lagrangian point orbits. In *The 24th AAS/AIAA Space Flight Mechanics Meeting*, pages 26–30, 2014.

[21] R. Armellin, M. Rasotto, P.i Di Lizia, and F. Renk. End-of-life disposal of libration point orbit missions: The case of gaia. *Advances in Space Research*, 56(3):461–478, 2015.

[22] Z. P. Olikara, G. Gómez, and J. J. Masdemont. Dynamic mechanisms for spacecraft disposal from sun–earth libration points. *Journal of Guidance, Control, and Dynamics*, 38(10):1976–1989, 2015.

[23] S. Soldini, C. Colombo, and S. Walker. The end-of-life disposal of satellites in libration-point orbits using solar radiation pressure. *Advances in Space Research*, 57(8):1664–1679, 2016.

[24] C. Colombo, F. Letizia, S. Soldini, and F. Renk. Disposal of libration point orbits on a heliocentric graveyard orbit: the gaia mission. In *Proceedings of the 25th International Symposium on Space Flight Dynamics, ISSFD, Munic, Germany*, 2015.

[25] W. J. Van der Weg and M. Vasile. Sun–earth l 1 and l 2 to moon transfers exploiting natural dynamics. *Celestial Mechanics and Dynamical Astronomy*, 120(3):287–308, 2014.

[26] E. M. Alessi, C. Colombo, and M. Landgraf. Re-entry disposal analysis for libration point orbit missions. In *24th International Symposium on Space Flight Dynamics ISSFD 2014*, pages 5–9, 2014.

[27] E. M. Alessi. The reentry to earth as a valuable option at the end-of-life of libration point orbit missions. *Advances in Space Research*, 55(12):2914–2930, 2015.

[28] K. K. Boudad. Disposal dynamics from the vicinity of near rectilinear halo orbits in the earth-moon-sun system. Master's thesis, Purdue University, 2018.

[29] K. K. Boudad, D. C. Davis, and K. C. Howell. Disposal trajectories from near rectilinear halo orbits. In *AAS/AIAA Astrodynamics Specialists Conference*, number JSC-E-DAA-TN60056, 2018.

[30] D. C. Davis, K. K. Boudad, S. M. Phillips, and K. C. Howell. Disposal, deployment, and debris in near rectilinear halo orbits. In *AAS/AIAA Space Flight Mechanics Meeting*, number JSC-E-DAA-TN64520, 2019.

[31] D. C. Davis, K. K. Boudad, R. J. Power, K. C. Howell, and D. J. Sweeney. Heliocentric escape and lunar impact from near rectilinear halo orbits. In *AAS/AIAA Astrodynamics Specialists Conference*, number JSC-E-DAA-TN72013, 2019.

[32] S. T. Scheuerle, D. C. Davis, E. M. Zimovan-Spreen, B. P. McCarthy, D. B. Henry, and K. C. Howell. Jettison and disposal from near rectilinear halo orbits, part 1: Theory. In *American Astronautical Society Astrodynamics Specialists Conference*, number AAS 23-311, 2023.

[33] D. C. Davis, S. T. Scheuerle, S. L. McCarty, E. M. Zimovan-Spreen, B. P. McCarthy, M. L. McGuire, and K. C. Howell. Jettison and disposal from near rectilinear halo orbits, part 2: Applications. In *AAS/AIAA Astrodynamics Specialist Conference*, number AAS 23-306, 2023.

[34] D. C. Davis. *Multi-body trajectory design strategies based on periapsis Poincaré maps*. PhD thesis, Purdue University, 2011.

[35] K. K. Boudad, K. C. Howell, and D. C. Davis. Departure and escape dynamics from the near rectilinear halo orbits in the earth-moon-sun system. *The Journal of the Astronautical Sciences*, 69(4):1076–1114, 2022.

[36] M. Bolis, E. M. Alessi, and C. Colombo. End-of-life disposal design for near-rectilinear halo orbits. In *76th International Astronautical Congress (IAC 2025)*, pages 1–14, 2025.

[37] K. F. Wakker. Fundamentals of astrodynamics. *TU Delft Repository, Delft*, 2015.

[38] R. Castelli. On the relation between the bicircular model and the coupled circular restricted three-body problem approximation. In *Nonlinear and Complex Dynamics: Applications in Physical, Biological, and Financial Systems*, pages 53–68. Springer, 2011.

[39] D. C. Heggie. Bifurcation at complex instability. *Celestial mechanics*, 35(4):357–382, 1985.

[40] E. M. Zimovan-Spreen, K. C. Howell, and D. C. Davis. Near rectilinear halo orbits and their application in cis-lunar space. In *3rd IAA Conference on Dynamics and Control of Space Systems, Moscow, Russia*, volume 20, page 40, 2017.

[41] E. M. Zimovan-Spreen, K. C. Howell, and D. C. Davis. Near rectilinear halo orbits and nearby higher-period dynamical structures: orbital stability and resonance properties. *Celestial Mechanics and Dynamical Astronomy*, 132(5):28, 2020.

[42] M. Bolis, E. M. Alessi, and C. Colombo. End-of-life disposal parametric analysis in cislunar space: Earth-moon l2 escape no-return trajectories. In *9th European Conference on Space Debris, ESA/ESOC*, pages 1–13, 2025.

[43] C. R. Short. *Flow-Informed Strategies for Trajectory Design and Analysis*. PhD thesis, Purdue University, West Lafayette, Indiana, 2016.

[44] L. Bucci. *Mission Analysis and Operational Aspects for a Lunar Exploration Architecture*. PhD thesis, Politecnico di Milano, Milan, Italy, 2019.

[45] M. Bolis, E. M. Alessi, and C. Colombo. Long-term evolution of orbits in cislunar space: characterisation and stability analysis. In *76th International Astronautical Congress (IAC 2025)*, pages 1–14, 2024.

A | Appendix A

A.1. Orbit with JC = 3.0474 and SI = 1.2971

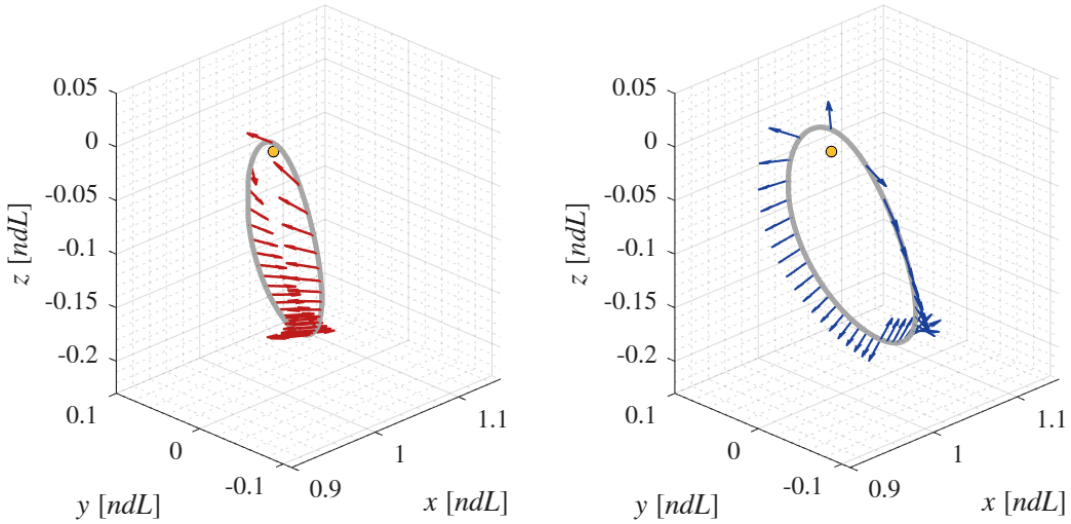

(a) Position (+).

(b) Velocity (+).

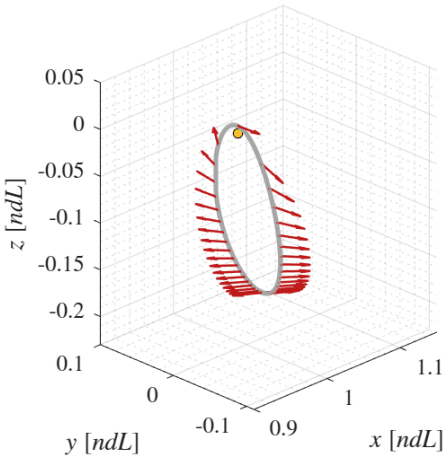

(c) Position (−).

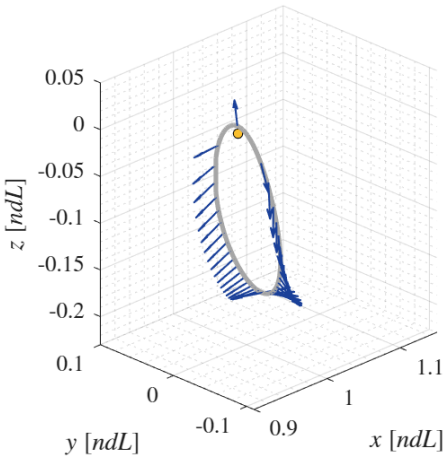

(d) Velocity (−).

Figure A.1: Positive and negative state perturbation

A.2. Orbit with JC = 3.0546 and SI = 1.0962

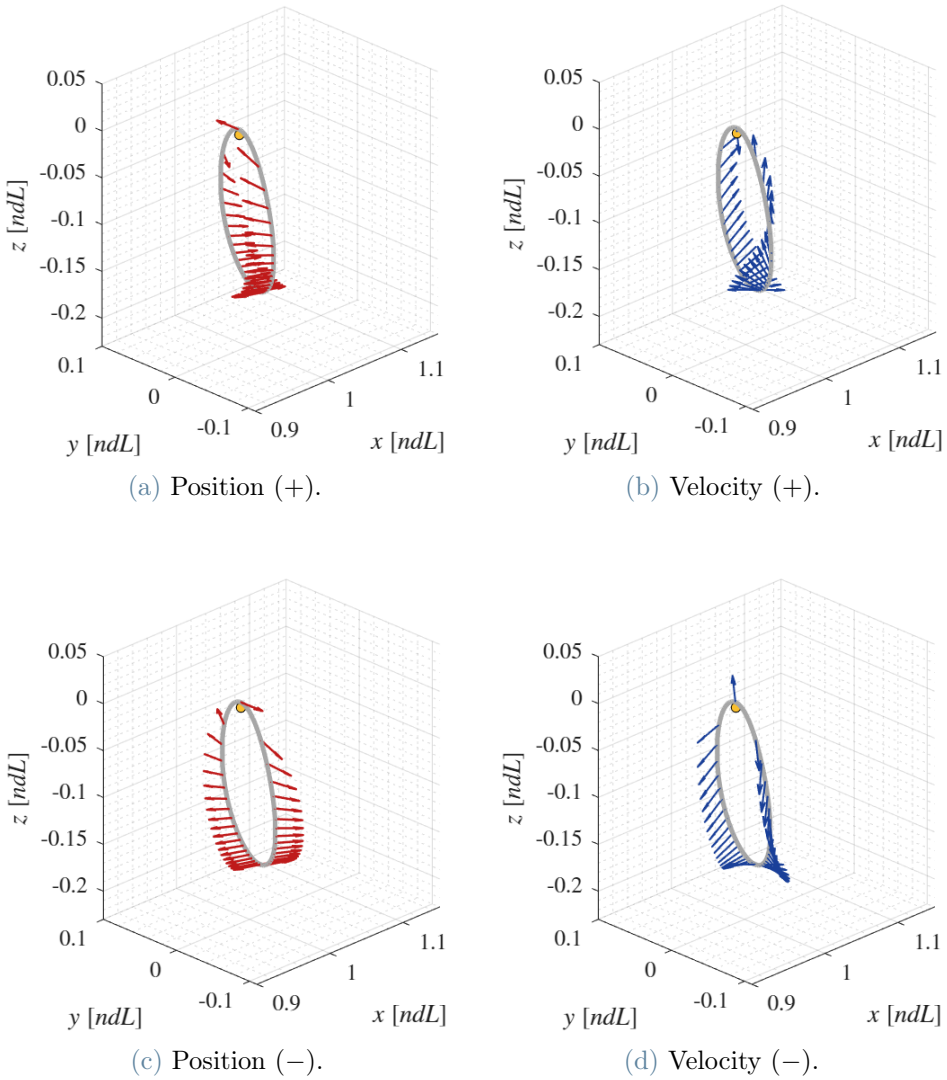

(a) Position (+).

(b) Velocity (+).

(c) Position (−).

(d) Velocity (−).

Figure A.2: Positive and negative state perturbation

A.3. Orbit with JC = 3.0176 and SI = 1.0944

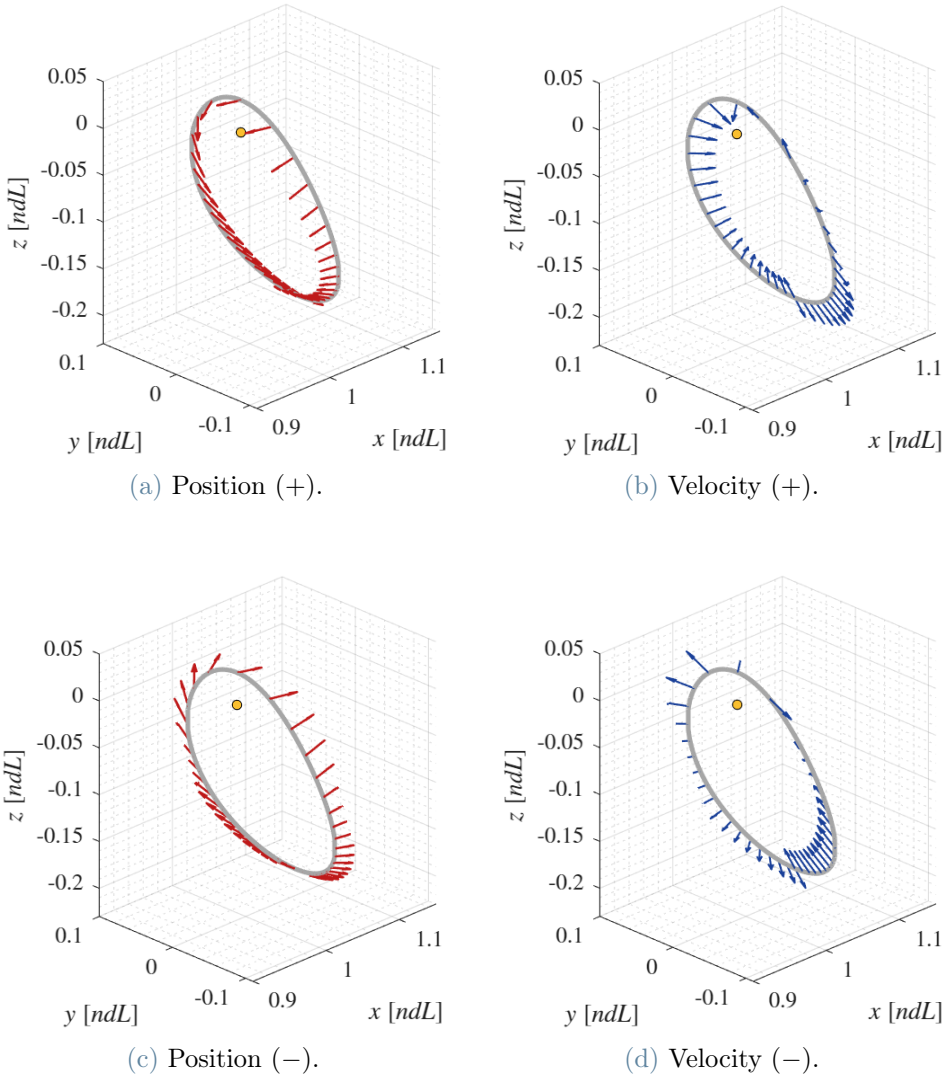

(a) Position (+). (b) Velocity (+).

(c) Position (−). (d) Velocity (−).

Figure A.3: Positive and negative state perturbation

B | Appendix B

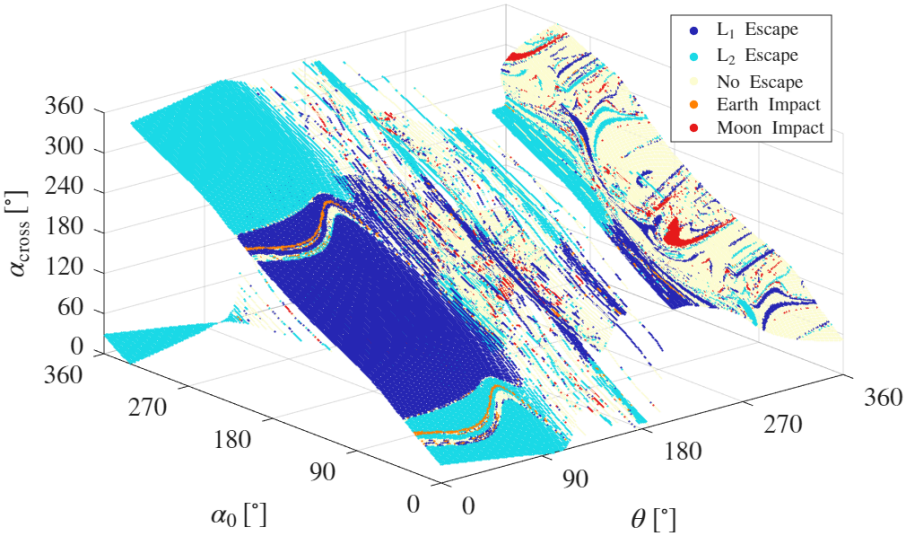

(a) Positive manifold perturbation.

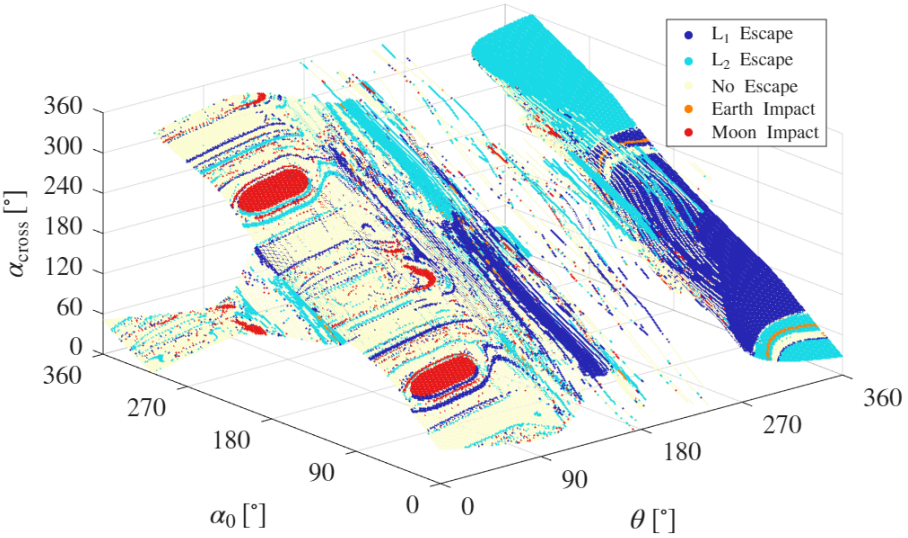

(b) Negative manifold perturbation.

Figure B.1: Three-dimensional representation of the angular mapping for the orbit with $JC = 3.0271$ and $SI = 1.6908$.

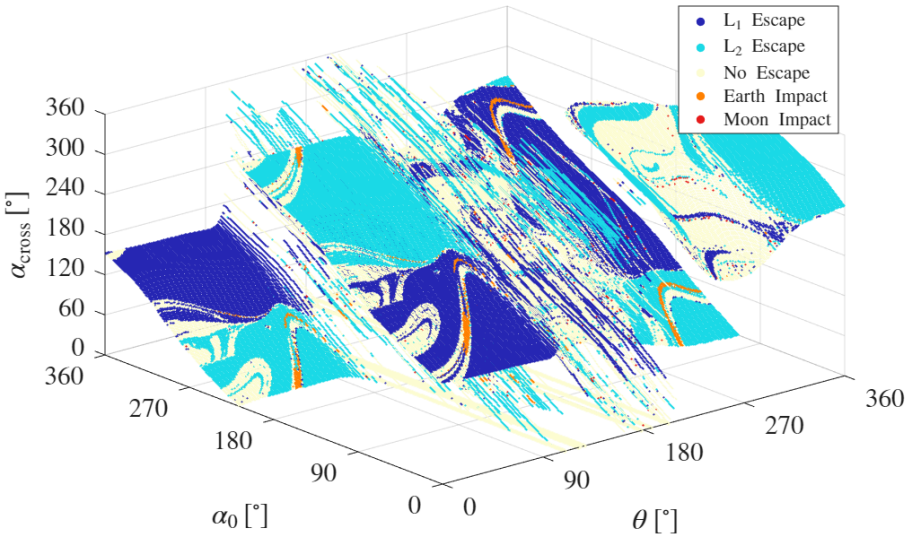

(a) Positive manifold perturbation.

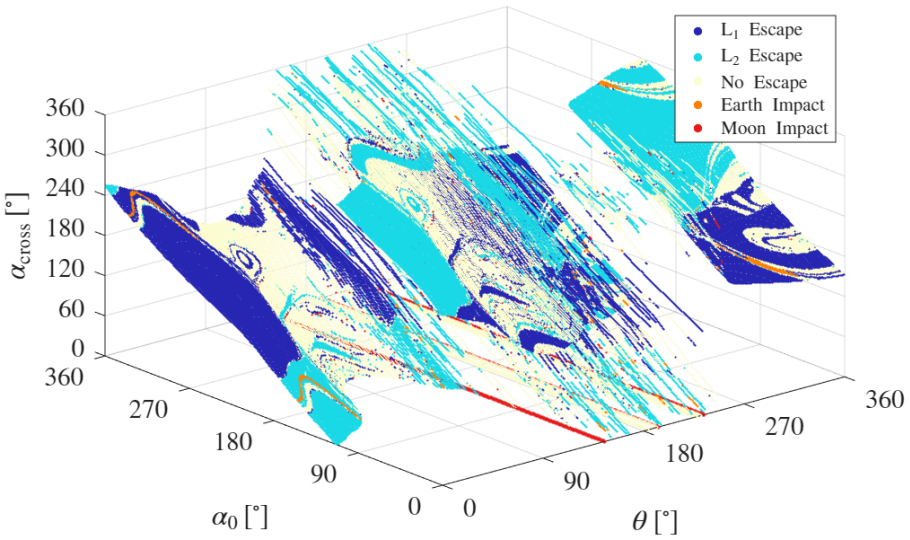

(b) Negative manifold perturbation.

Figure B.2: Three-dimensional representation of the angular mapping for the orbit with $JC = 3.0474$ and $SI = 1.2971$.

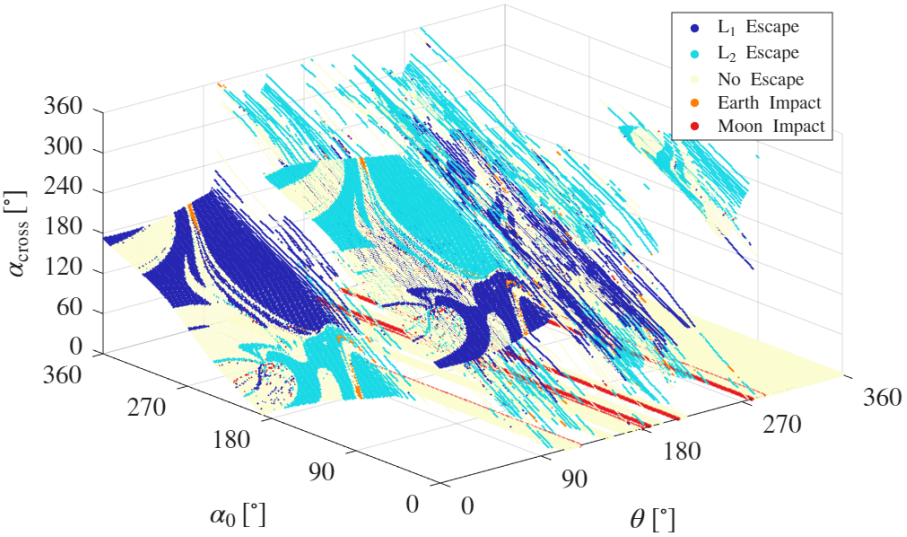

(a) Positive manifold perturbation.

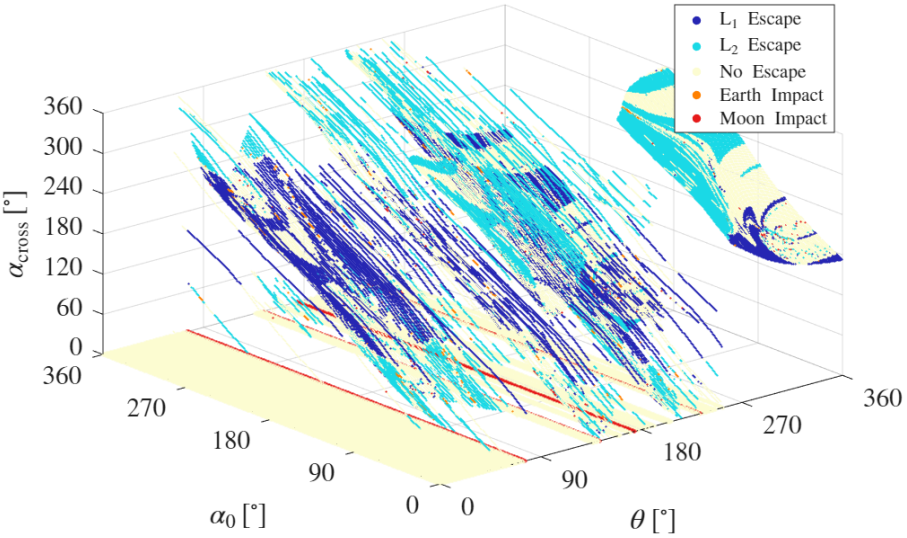

(b) Negative manifold perturbation.

Figure B.3: Three-dimensional representation of the angular mapping for the orbit with $JC = 3.0546$ and $SI = 1.0962$.

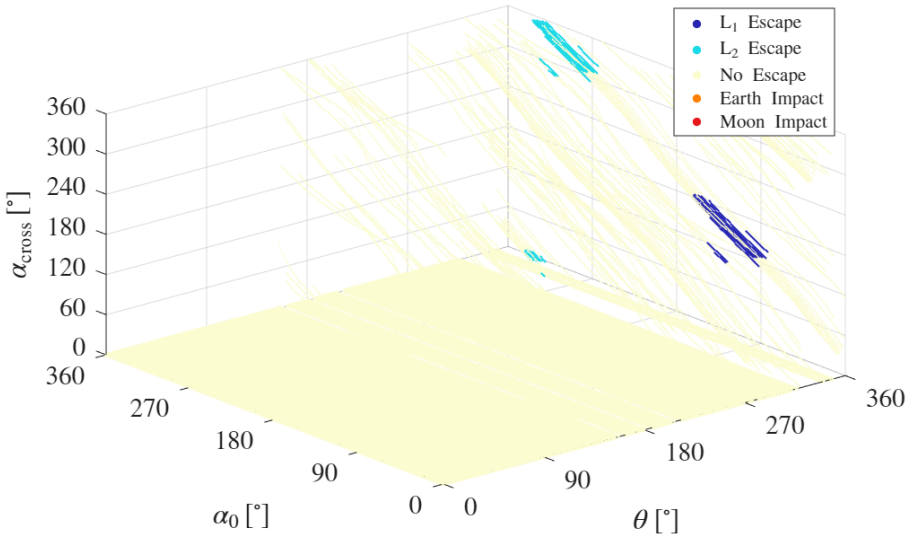

(a) Positive manifold perturbation.

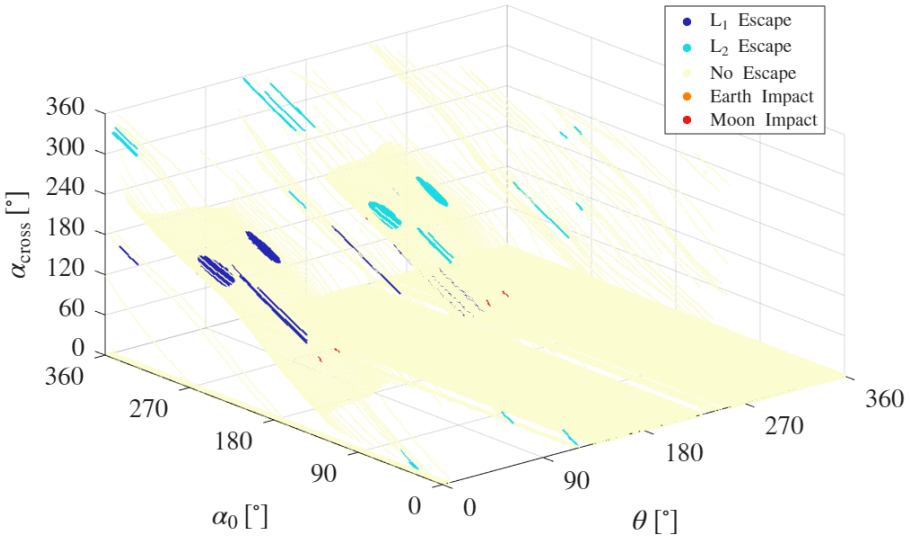

(b) Negative manifold perturbation.

Figure B.4: Three-dimensional representation of the angular mapping for the orbit with $JC = 3.0176$ and $SI = 1.0944$.

List of Figures

List of Tables

List of Symbols

Acronyms

Acronym	Description
BCR4BP	Bicircular Restricted Four-Body Problem
CR3BP	Circular Restricted Three-Body Problem
EoL	End-of-Life
EoM	Equation of Motion
ESA	European Space Agency
FTLE	Finite Time Lyapunov Exponent
JC	Jacobi Constant
LEO	Low Earth Orbit
LPO	Libration Point Orbit
MI	Momentum Integral
ndL	non-dimensional Length
ndT	non-dimensional Time
NRHO	Near-Rectilinear Halo Orbit
RHS	Right Hand Side
SI	Stability Index
STM	State Transition Matrix
WSB	Weak Stability Boundary
ZVC	Zero Velocity Curve
ZVS	Zero Velocity Surface

Scalars

Variable	Description	SI unit
α	phase between Earth-Moon and Sun-Earth system	rad
α_0	α at the beginning of the propagation	rad
α_{cross}	α at the first switch from Earth-Moon to Sun-Earth system	rad
θ	phase angle along the orbit	rad
U	CR3BP potential function	-
L_{m}	Earth-Moon characteristic length	m
L_{s}	Sun-Earth characteristic length	m
ω_{EM}	angular velocity of the rotating Earth-Moon system	1/ndT
ω_{SE}	angular velocity of the rotating Sun-Earth system	1/ndT
X, Y, Z	spatial coordinates in the inertial frame	m
$\dot{X}, \dot{Y}, \dot{Z}$	velocity coordinates in the inertial frame	m/s
x, y, z	spatial coordinates in the rotating frame	ndL
$\dot{x}, \dot{y}, \dot{z}$	velocity coordinates in the rotating frame	ndL/ndT
t	time	s
t_{EM}	non-dimensional time in the Earth-Moon system	ndT
t_{SE}	non-dimensional time in the Sun-Earth system	ndT
T	orbital period	s
T_{ref}	reference time for computing FTLE	ndT
$\sigma_{T_{\text{ref}}}$	FTLE symbol	-
r_1	distance of the third body from the larger primary	ndL
r_2	distance of the third body from the smaller primary	ndL
m_1	mass of the larger primary	Kg
m_2	mass of the smaller primary	Kg
μ	non-dimensional gravitational constant	-
λ	eigenvalue	-
ν_{max}	SI symbol	-
ε	perturbation along the unstable direction	ndL(/ndT)

Vectors and matrices

Variable	Description
$\mathbf{r}$	position vector in the rotating frame
$\mathbf{r_1}$	relative position vector w.r.t. the larger primary in the rotating frame
$\mathbf{r_2}$	relative position vector w.r.t. the smaller primary in the rotating frame
$\mathbf{\Lambda}^u$	unstable manifold direction
$\mathbf{\Phi}$	State Transition Matrix
$\mathbf{I}$	Identity matrix

Ringraziamenti

Vorrei ringraziare la Professoressa Camilla Colombo per avermi dato l'opportunità di svolgere questa tesi e per il supporto ricevuto durante questi mesi.
Un grazie speciale a Mathilda, per avermi seguito con attenzione dall'inizio di questo percorso, per la disponibilità e per tutti i consigli ricevuti.